BIOPHYSICAL CHARACTERIZATION OF HONEY BEE VIRUS UNTRANSLATED REGIONS

JENNA MARIA LETAIN
Bachelor of Science, University of Lethbridge, 2022

A thesis submitted
in partial fulfilment of the requirements for the degree of

MASTER OF SCIENCE

in

BIOCHEMISTRY

Department of Chemistry and Biochemistry
University of Lethbridge
LETHBRIDGE, ALBERTA, CANADA

BIOPHYSICAL CHARACTERIZATION OF HONEY BEE VIRUS UNTRANSLATED REGIONS

JENNA LETAIN

Date of Defence: November 28, 2024

Dr. Trushar Patel	Associate Professor	Ph.D.
Thesis Supervisor		
Dr. Shelley Hoover	Associate Professor	Ph.D.
Thesis Examination Committee Member		
Dr. Theresa Burg	Professor	Ph.D.
Thesis Examination Committee Member		
Dr. Michael Gerken	Professor	Ph.D.
Chair, Thesis Examination Committee		

Abstract

Over the past two decades, honey bee colony losses have become a serious and widespread issue. Many factors contribute to these losses, but one major driver is viruses. Sacbrood virus and deformed wing virus are found globally and can cause detrimental effects to honey bee colonies. These viruses have a long, single-stranded genome of ribonucleic acid (RNA) flanked by structured untranslated regions. Although noncoding, these regions play important roles in the viral life cycle. While untranslated regions have been studied extensively in other viruses, there is a research gap for honey bee viruses. This thesis focuses on the biophysical characterization of the untranslated regions of these two common honey bee viruses. Small-angle X-ray scattering and computational modelling elucidated low and high-resolution three-dimensional structures for the viral untranslated regions. Functional assays revealed that the sacbrood virus 5′ untranslated region acts as an internal ribosome entry site capable of initiating translation. Furthermore, immunoprecipitation pull-down assays identified potential RNA-binding proteins that interact with the sacbrood virus untranslated regions. Altogether, this thesis provides foundational insights into the characteristics of the untranslated regions of sacbrood virus and deformed wing virus, guiding future research in this field.

Contribution of Authors

Chapter 2 is a collaborative manuscript prepared for journal submission. The work for this chapter was completed in collaboration Dr. Eric Jan's laboratory at the University of British Columbia. Contributors to the work completed include Subash Chapagain, Dr. Higor Pereira, SarahAnn Walker, Dr. Luc Roberts, Dr. Shelley Hoover, Dr. Eric Jan, and Dr. Trushar Patel. I performed wet laboratory experiments with support from SarahAnn Walker. The *in vitro* and *in vivo* bicistronic reporter assays were carried out by Subash Chapagain (Jan Group). Dr. Pereira aided with SAXS analysis and computational modelling. I wrote the initial manuscript, with feedback and edits from Dr. Jan, Dr. Hoover, Dr. Roberts, Dr. Pereira, Subash, and Dr. Patel.

Chapter 3 details unpublished work completed with assistance from SarahAnn Walker, Dr. Higor Pereira, and Dr. Trushar Patel. I conducted wet laboratory experiments, with support from SarahAnn Walker. Dr. Pereira assisted with SAXS analysis and computational modelling. I wrote the manuscript and incorporated edits from Dr. Patel.

Chapter 4 describes unpublished work conducted with SarahAnn Walker, Dr. Govi Veerareddygari, Danielle Gemmill, Dr. Shelley Hoover, Jack Moore, and Dr. Trushar Patel. I performed all wet laboratory experiments, with assistance from SarahAnn Walker. Dr. Veerareddygari assisted with DIG-NHS ester RNA labelling. Danielle Gemmill provided the initial pull-down assay protocol and helped with early pull-down assays. Dr. Hoover supplied the honey bees used for the pull-down assays. Jack Moore from the Alberta Proteomics and Mass Spectrometry Facility (University of Alberta) conducted mass spectrometry. I analyzed the mass spectrometry data, while SarahAnn helped with protein literature searches. I wrote the manuscript, with editing support from Dr. Patel.

Acknowledgements

I would like to thank my supervisor, Dr. Trushar Patel, for allowing me to study a topic I'm truly passionate about. Thank you for always believing in me and mentoring me over these past few years. Thank you to all Patel lab members who have always been there for support. I'm very thankful for the friendships I have created over the past two years with you and the Demeler lab members. I greatly cherish our scheduled coffee breaks and the memories I've made. Also, a huge thank you to my independent study student, SarahAnn Walker. I appreciate all your help and dedication.

Thank you to Dr. Shelley Hoover and Dr. Theresa Burg for participating in my committee. Shelley, thank you for contributing the honey bees for the pull-down assays.

Thank you to everyone and anyone who has mentored me these past few years. Dr. Luc Roberts, thank you for inspiring me to pursue graduate school back in the Allos days and for answering many of my questions. Dr. Higor Pereira, thank you for your help with SAXS and our many discussions on the SBV IRES manuscript. Dr. Gunjan Vasudeva, thank you for helping establish BeeSafe, and I'm looking forward to continuing down that path with you.

A huge thank you to my husband, Rhéal. You've been my biggest rock and support throughout this entire time, and I am so grateful for you. I wouldn't be where I am today without your ongoing support. Thank you to my parents and family, who have always been my biggest cheerleaders. To all my friends, thank you for supporting me and helping with my work-life balance. Finally, I can't forget about my two cats, Isaac and Newton. Thank you, boys, for being the best little fuzzy emotional support animals a girl could ask for (most of the time).

Table of Contents **Page**

Abstract iii

Contribution of Authors iv

Acknowledgements v

Table of Contents vi

List of Tables ix

List of Figures x

List of Abbreviations xii

Chapter 1. Introduction

1.1 Western honey bee (*Apis mellifera* L.) 1

1.2 Iflaviruses 3

1.2.1 Deformed wing virus 3

1.2.2 Sacbrood virus 6

1.2.3 Genome organization 7

1.2.4 Untranslated regions 8

1.3 Internal ribosome entry sites 10

1.3.1 Iflavirus IRESs 11

1.4 Thesis objectives 13

1.5 References 14

Chapter 2. Structural and Functional Insights into Sacbrood Virus Untranslated Regions (UTRs) Reveal an Internal Ribosome Entry Site in the 5′ UTR

2.1 Foreword 22

2.2 Abstract 23

2.3 Introduction 24

2.4 Materials and Methods 26

2.4.1 Plasmid design and constructs 26

2.4.2 RNA purification 27

2.4.3 Multi-angle light scattering (MALS) 27

2.4.4 Small-angle X-ray scattering (SAXS) 28

2.4.5 Tertiary structure model fitting 28

2.4.6 Bicistronic luciferase assays 29
2.4.8 Cell culturing and transfection 29
2.5 Results and Discussion 31
2.5.1 Purification and absolute molecular weight determination of SBV UTRs 31
2.5.2 SAXS analysis reveals a distinct SBV 5′ UTR and an elongated SBV 3′ UTR 32
2.5.3 Full-length SBV 5′ UTR and a critical 39 nt region have IRES activity *in vitro* 41
2.5.4 SBV 5′ UTR has IRES activity in S2 cells 44
2.5.5 SBV IRES structural elements 45
2.6 Conclusion 48
2.7 Data Availability 48
2.8 Supplementary Data 49
2.9 References 50
Chapter 3. Biophysical Characterization of the Deformed Wing Virus 3′ Untranslated Region
3.1 Foreword 55
3.2 Introduction 56
3.3 Materials and Methods 59
3.3.1 Plasmid preparation 59
3.3.2 Synthesis and purification of RNA 59
3.3.3 SEC coupled with multi-angle light scattering (MALS) 60
3.3.4 Small-angle X-ray scattering (SAXS) 60
3.3.5 Tertiary structure prediction and model fitting 61
3.4 Results 62
3.4.1 DWV 3′ UTR purification and absolute molecular weight determination 62
3.4.2 Low-resolution structure determination of the DWV 3′ UTR in solution 63
3.4.3 High-resolution atomistic model structure prediction of the DWV 3′ UTR 67
3.5 Discussion 71
3.6 Conclusion and Future Directions 76
3.7 References 77

Chapter 4. Towards Understanding the Interactions of Sacbrood Virus Untranslated Regions with *Apis mellifera* Proteins

4.1 Foreword....81

4.2 Introduction....82

4.3 Materials and Methods....85

4.3.1 Plasmid preparation....85

4.3.2 RNA purification....86

4.3.3 Digoxigenin (DIG) labelling of RNA....86

4.3.4 Crosslinking the A/G magnetic beads....87

4.3.5 Pull-down assays and mass spectrometry analysis....88

4.3.6 Bioinformatic analysis of mass spectrometry data....89

4.4 Results....90

4.4.1 Purification of *in vitro* transcribed SBV 5′ and 3′ UTRs....90

4.4.2 DIG-labelling efficiency....91

4.4.3 Potential RNA-binding proteins revealed through the SBV 5′ and 3′ UTR pull-down assays....92

4.4.4 BlastKOALA analysis of total protein hits from the SBV 5′ and 3′ UTR pull-down assays....95

4.5 Discussion....98

4.6 Conclusion and Future Directions....104

4.7 References....106

Chapter 5. Conclusions

5.1 Overview....111

5.2 Future Directions....113

5.3 References....115

List of Tables

Table 2.1: Biophysical properties of the SBV 5′ and SBV 3′ UTRs determined from small-angle X-ray scattering (SAXS) analysis 35

Table 3.1: Biophysical parameters of the DWV 3′ UTR determined from small-angle X-ray scattering (SAXS) analysis 66

Table 4.1: Mass spectrometry (MS) high-hit proteins (HHPs) 93

List of Figures

Figure 1.1: The global distribution of DWV and SBV in 2020 5

Figure 1.2: Linear representation of the Iflavirus genome 8

Figure 2.1: Purification and absolute molecular weight (M_W) determination of the SBV 5′ and 3′ UTRs 32

Figure 2.2: Small-angle X-ray scattering (SAXS) characterization of the SBV 5′ (green) and SBV 3′ (blue) UTRs 34

Figure 2.3: Small-angle X-ray scattering (SAXS) *ab initio* envelope models of the SBV 5′ (green) and 3′ (blue) UTRs 36

Figure 2.4: Visualization of the SBV UTR secondary structures and resulting computationally derived tertiary models 38

Figure 2.5: Model fitting of the SBV 5′ UTR SAXS envelope with their atomistic tertiary models 40

Figure 2.6: Model fitting of the SBV 3′ UTR SAXS envelope with their atomistic tertiary models 40

Figure 2.7: Determination of IRES activity of the SBV 5′ UTR 42

Figure 2.8: Visualizing the minimal region required for IRES activity 44

Figure S2.1: Urea-PAGE analysis of purified *in vitro* transcribed SBV UTRs 49

Figure S2.2: Raw luciferase values from the SBV 5′ UTR deletion mutant analysis 49

Figure 3.1: Size exclusion chromatography (SEC) purification of *in vitro* transcribed DWV 3′ UTR 62

Figure 3.2: SEC-coupled multi-angle light scattering (MALS) trace for determining the absolute molecular weight (M_W) of the DWV 3′ UTR 63

Figure 3.3: Small-angle X-ray scattering (SAXS) data analysis of the DWV 3′ UTR 65

Figure 3.4: Low-resolution SAXS envelope of the DWV 3′ UTR 67

Figure 3.5: 2-D representation of the DWV 3′ UTR secondary structure 68

Figure 3.6: SAXS envelope overlayed with atomistic computational models of the DWV 3′ UTR 70

Figure 4.1: Size exclusion chromatography (SEC) purification of the SBV wildtype and Scrambled UTRs 90

Figure 4.2: Electrophoretic mobility shift assay (EMSA) verifying successful DIG-labelling of the SBV UTRs 92

Figure 4.3: STRING network of potential protein-protein interactions of immunoprecipitated proteins associated with the SBV 5′ UTR..... 94

Figure 4.4: STRING network of potential protein-protein interactions of immunoprecipitated proteins associated with the SBV 3′ UTR..... 95

Figure 4.5: BlastKOALA analysis of total protein hits (TPHs) from the SBV UTR pull-down assays 97

List of Abbreviations

(+)ssRNA	Positive-sense single-stranded ribonucleic acid
2-D	Two-dimensional
3-D	Three-dimensional
Ab	Antibody
BlastKOALA	Basic Local Alignment Search Tool for the KEGG Orthology and Links Annotation
C	Cluster
CrPV	Cricket paralysis virus
DIG	Digoxigenin
DIG-NHS	Digoxigenin-3-O-methylcarbonyl-ε-aminocaproic acid-N-hydroxysuccinimide
D_{max}	Maximum dimension
dn/dc	Refractive index increment
DWV	Deformed wing virus
EDC	1-ethyl-3-[3-dimethylaminopropyl]carbodiimide hydrochloride
eIF	Eukaryotic initiation factor
EMCV	Encephalomyocarditis virus
EMSA	Electrophoretic mobility shift assay
EoPV	*Ectropis obliqua* picorna-like virus
FLuc	Firefly luciferase
FMDV	Foot-and-mouth disease virus
HHP	High-hit protein
HPLC	High-performance liquid chromatography
IFV	Infectious flacherie virus
IGR	Intergenic region
IRES	Internal ribosome entry site
ITAF	IRES trans-acting factor

IVT	*in vitro* transcription
kDa	Kilodalton
KEGG	Kyoto Encyclopedia of Genes and Genomes
LS	Light scattering
m^7G	7-methylguanosine
MALS	Multi-angle light scattering
MHC	Myosin heavy chain
mPKI	Cricket paralysis virus mutant
MS	Mass spectrometry
M_W	Molecular weight
NMR	Nucleic magnetic resonance
NSD	Normalised spatial discrepancy
nt	Nucleotides
OGDH	2-oxoglutarate dehydrogenase
ORF	Open reading frame
P(r)	Distance pair distribution
PAGE	Polyacrylamide gel electrophoresis
PBS	Phosphate-buffered saline
PCBP2	Poly(C) binding protein-2
PnV	*Perina nuda* virus
Poly-A	Poly-adenylated
PRM	Paramyosin
PTB	Polypyrimidine tract-binding protein
RBP	RNA-binding protein
RdRp	RNA-dependent RNA polymerase
R_g	Radius of gyration
RI	Refractive index
RLuc	*Renilla* luciferase

RNA	Ribonucleic acid
Rp	Ribosomal protein
S2	Schneider 2
S200	Superdex 200 Increase 10/300 GL
SAXS	Small-angle X-ray scattering
SBV	Sacbrood virus
SDS	Sodium dodecyl sulphate
SEC	Size exclusion chromatography
Sf21	*Spodoptera frugiperda* 21
SHAPE	Selective 2’ Hydroxyl Acylation analyzed by Primer Extension
SL	Stem-loop
STRING	Search Tool for the Retrieval of Interacting Genes/Proteins
TBE	Tris-borate-ethylenediaminetetraacetic acid
TCA	Tricarboxylic acid
TPHs	Total protein hits
UTR	Untranslated region
VDV-1	*Varroa destructor* virus-1
Vg	Vitellogenin
VPg	Genome-linked viral protein
WT	Wildtype
X^2	Goodness-of-fit parameter

Chapter 1: Introduction

1.1 Western honey bee (*Apis mellifera* L.)

The western honey bee (*Apis mellifera* L.) is used by farmers worldwide to aid in crop pollination and to produce honey and other hive products (1). Pollination is an essential reproductive process for seed and fruit development in most crops (2). Honey bees and other pollinators facilitate this process by transferring pollen between flowers. This can lead to better quality and yields of numerous crops, allowing honey bees to aid directly in the increased economic value of agricultural production (3). Many crops, such as apples, almonds, cherries, squash, oranges, and vegetable seeds, require pollination or benefit significantly from it (4). In addition to managed honey bees, wild non-*Apis* bee populations are crucial for maintaining plant diversity and can contribute to agricultural crop pollination (5-7). Without the contribution of honey bees, the quality and quantity of crops would be reduced, highlighting their vital role in modern agriculture (3).

There are over 790,000 managed honey bee colonies spread throughout Canada (8). In 2021, the estimated annual economic contribution of honey bee pollination in Canada through direct additional harvest value, including hybrid canola seed (*Brassica napus* L.) production, was about $7 billion (8). The production of hybrid canola seed in southern Alberta mainly depends on managed honey and alfalfa leafcutting bees (*Megachile rotundata* F.) (9). Beyond crop pollination, honey production is another major contributor to the Canadian economy. In 2023, Canada produced 91.8 million pounds of honey, valuing over $277 million (8). Alberta is a large honey producer, accounting for ~40% of this total honey production (8,10). Of the honey produced, a significant portion is exported to other countries, with the United States and Japan

receiving 48.3% and 46.3% of exports, respectively (8). Together, these services emphasize the substantial economic value honey bees bring to the agricultural sector.

However, honey bees face significant health challenges that threaten the sustainability of the beekeeping industry and the agricultural sectors dependent on their pollination (11,12). Over the past couple of decades, high levels of over-winter colony mortality have been an issue for beekeepers. From 2007 to 2023, national winter losses in Canada ranged from 15.3% to 45.5%, averaging 27% (13). Over the winter of 2022-2023, Canadian beekeepers reported losing 32.2% of colonies (13). In the United States, beekeepers lost an estimated 48% of their colonies over the same winter (14). Beekeepers facing these losses bear the expenses of replacing deceased colonies and dealing with the loss of income from honey and pollination services (15).

Many factors can contribute to these colony losses, including pesticide use, climate change, weather, poor nutrition, poor quality queens, parasites, and pathogens, including fungi, bacteria, and viruses (13,16-23). A combination of these factors is typically responsible for colony decline (24). The continuous loss of honey bee colonies emphasizes the urgency of finding solutions to combat these losses better. Integrated Pest Management strategies, which combine control tactics such as monitoring and treatment plans, are commonly used to help maintain healthy bees (25). However, Integrated Pest Management has limited effectiveness against other factors, such as viral pathogens, which currently have limited direct treatments (26). Irradiation has proven effective against waxborne viruses; however, this treatment is not universally available or economically viable for many beekeepers (27).

1.2 Iflaviruses

Viruses infecting honey bees have negatively affected colony health in recent years. Over twenty reported viruses infect honey bees, most belonging to the order *Picornavirales* (28,29). Nine families are recognized within this order, infecting various hosts, including vertebrates, plants, protists, and invertebrates (30,31). Among these, the insect-infecting *Iflaviridae* family has one genus (*Iflavirus*) with sixteen recognized species (30). The first categorized Iflavirus was the infectious flacherie virus (IFV) that infects silkworms (*Bombyx mori* L.). Also included within this family are the most common bee-infecting viruses, such as sacbrood virus (SBV, *Morator aetatulas*), deformed wing virus (DWV), slow bee paralysis virus, and other less common viruses (32-35).

1.2.1 Deformed wing virus

DWV is one of the most widespread honey bee viruses found globally except in a few select regions (**Figure 1.1**) (36). While initially discovered in *A. mellifera*, it has also been documented in other *Apis* and *Bombus* species, including bumble bees (*Bombus terrestris* L. and *Bombus pascuorum* Scopoli) (37,38). The spread of DWV has been closely linked to the ectoparasitic mite known as varroa (*Varroa destructor* Anderson and Trueman) (39). Originally described as a parasite of the eastern honey bee (*Apis cerana* F.), varroa shifted hosts to *A. mellifera* in the first half of the 20th century (40). The mite is also an efficient vector for several other honey bee viruses (41). When feeding on honey bee adults, larvae, and pupae, varroa facilitates the introduction of viral particles directly into bees' hemolymph (42,43). Varroa has been shown to induce immunosuppression in pupae, allowing viruses to infect efficiently (44).

The level of viral transmission is strongly positively correlated with the density of varroa within the hive, where high mite loads significantly increase viral titres (45).

As the name suggests, DWV is well known for causing wing deformities in adult honey bees and other abnormalities, including decreased body size, discolouration, and bloated abdomens (37,46). These deformities significantly shorten the lifespan of newly emerged bees, often dying within 67 hours of emergence (44,46). Chronic infections in colonies can lead to learning and cognitive deficits, affecting honey bee behaviour (47). The mechanism by which DWV causes these deficits is still being explored, but it may involve changes in gene expression in the brain (48). If a colony cannot compensate for significant losses, usually when mite levels are high and brood rearing slows, it will ultimately collapse. Large amounts of dead and dying bees will typically be seen around the hive entrance, along with a patchy brood pattern and pupae failing to emerge from their cells (46). While symptoms are present during overt infection, DWV can also be detected in all stages of development, from egg to adult workers, queens, and drones, without any apparent symptoms (49).

DWV is transmitted horizontally between bees and vertically from queen to offspring (50). Viral particles have been detected in brood food, indicating that horizontal transmission can occur via feeding (51). Vertical transmission, on the other hand, allows viral spread to occur through a transovarial route from infected queens to their offspring (52). Venereal transmission can also occur, where infected drones can spread DWV to a queen during mating (53). The combination of multiple transmission routes allows for the rapid spread of DWV.

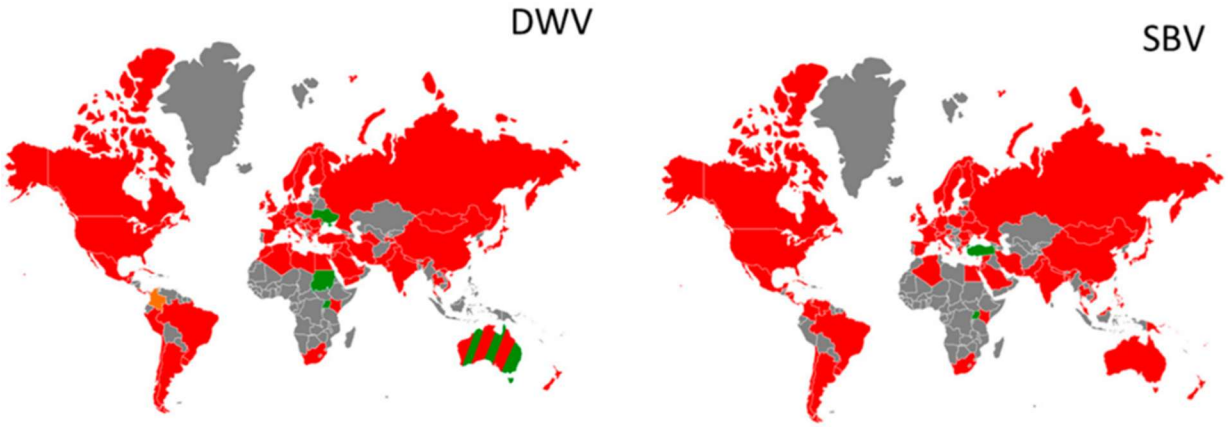

Figure 1.1. The global distribution of DWV and SBV in 2020. Red indicates that at least one study in the respective country has reported the presence of the virus. Green indicates that no study has detected the virus during screening in the respective country. Orange indicates that the virus has been detected, but only in bumblebees. Grey indicates an absence of data. Reproduced with permission from Alexis Beaurepaire (36).

The rapid spread of DWV through varroa and global honey bee exports has led to the emergence of three common variants: DWV-A (33), DWV-B (54), and DWV-C (55). These variants vary in their relative virulence (the capacity of a pathogen to cause disease) and epidemiology (56,57). Historically, DWV-A has been the most commonly seen variant and is associated with colony mortality (58,59). Kakugo virus, a subtype of DWV-A, was found in the brains of aggressive worker honey bees in Japan (60). Kakugo virus shares 98% genome similarity with DWV-A; however, it causes unusual aggressive behaviour not seen with DWV-A infections (61). Recently, many regions have shifted from DWV-A to DWV-B dominance (57,62,63). DWV-B, also known as *Varroa destructor* virus-1 (VDV-1), was first isolated from varroa and has high virulence and transmission rates (54,57). The less common variant, DWV-C, is not widely studied, and its overall impact is relatively unknown (55). Alongside these three common variants, a fourth, seldomly discussed variant known as DWV-D

is suspected to be extinct or rarely seen in modern bee populations (64). The extent of the DWV variants is yet to be fully understood.

1.2.2 Sacbrood virus

Sacbrood disease was first recorded in the United States in 1913 (65), and the causative agent, *Morator aetatulas*, was characterized in 1964 (66). Like DWV, SBV is now found worldwide in *A. mellifera* colonies (**Figure 1.1**) (36). Multiple strains of SBV target different hosts, including highly deadly strains that target *A. cerana*, such as the Chinese sacbrood virus (67). These variants have high mortality rates and are quite widespread in Asian colonies (67,68). In contrast, SBV infections in *A. mellifera* rarely lead to colony collapse, but they can still negatively impact colony productivity (16).

SBV significantly affects honey bee larvae, with larvae around two days old being the most susceptible to infection (69). The virus replicates rapidly, causing viral particles to accumulate in the ecdysial fluid beneath the larval skin (66). This causes the larvae to swell into the characteristic sac-like appearance, with a colour change from white to pale yellow and then to tan (70). Eventually, this leads to larval death, and the fluid-filled pouch will dry into a dark, leathery cuticle. SBV also infects adult bees without causing any visible symptoms and can lead to a shortened lifespan (71). Colonies affected by SBV will exhibit partially or completely uncapped brood cells, a common symptom of viral infection (70). The overall pathogenicity of SBV is dependent on other colony stressors, including temperature fluctuations and the presence of varroa (70). While there is no evidence that SBV is actively vectored by varroa, high mite infestations significantly weaken honey bee immune systems, making colonies more vulnerable to SBV (44,72).

Like DWV, the spread of SBV occurs through multiple transmission routes. SBV particles are left viable on honey, pollen, and dead larvae for up to four weeks (73). This environmental persistence allows for horizontal transmission, where bees become infected through contact with infectious material (50). Additionally, infected nurse bees can spread viral particles accumulated in their hypopharyngeal glands to larvae through glandular secretions (50). SBV can also spread vertically, where queens infected with SBV can transmit the virus to their offspring (72).

1.2.3 Genome organization

All Iflaviruses are comprised of a ribonucleic acid (RNA) genome that is single-stranded and of positive polarity (35). The understanding of the viral infection cycle of honey bee viruses is limited due to the absence of an optimized honey bee cell line (74). It is assumed that the infection cycles of honey bee viruses are like those of the well-studied *Picornaviridae* family. Iflaviruses likely enter the cell by receptor-mediated endocytosis, and their genome is released in the cytoplasm (75). Following genome translation, likely facilitated by an internal ribosome entry site (IRES) element, intracellular membranes are reorganized to form virus replication factories (35). The RNA is replicated through a negative strand intermediate, and newly packaged virions are released after cell disruption due to the cytopathic effect.

The Iflaviral genome is approximately 9-11,000 nucleotides long and contains a single open reading frame (ORF) flanked by 5′ and 3′ untranslated regions (UTRs) (**Figure 1.2**) (76). The ORF translates into a single polyprotein, which gets cleaved into functional viral proteins (35,77). The viral proteins include three major structural proteins (N-terminal region) and three non-structural proteins (C-terminal region) (76). The structural proteins include VP1, VP2, VP3, and, in some species, a smaller capsid protein (VP4) (76). Together, these proteins form the

protective capsid that encases the viral RNA. Some Iflaviruses have a leader protein of unknown function that precedes the structural proteins (35).

Like all members of the order *Picornavirales*, the non-structural proteins of viruses in the genus Iflavirus include RNA helicase, protease, and RNA-dependent RNA polymerase (RdRp) (31,35). The helicase domain belongs to the helicase superfamily III and aids in viral replication by unwinding duplex RNA structures (78,79). The protease, which resembles the picornavirus 3C protease, is essential for the proteolytic processing of the viral polyprotein (80). The RdRp resembles the picornavirus 3D RdRp and is a crucial component of the viral life cycle for synthesizing viral RNA (81,82). Alongside these, a putative genome-linked viral protein (VPg) is covalently attached to the 5′ terminus of the genome and acts as a primer for RNA synthesis (83,84).

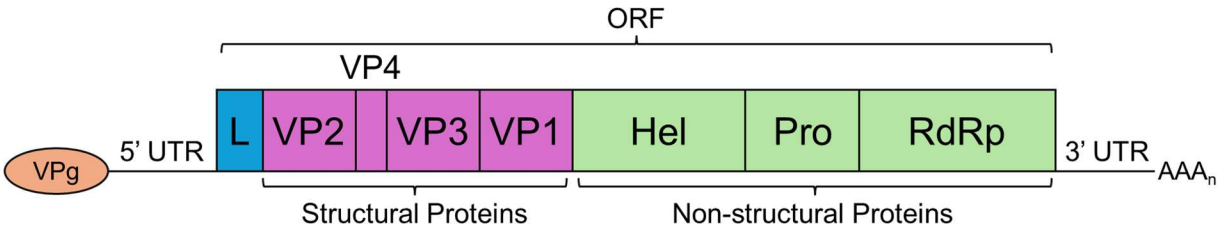

Figure 1.2. Linear representation of the Iflavirus genome. The genome is comprised of a single open reading frame (ORF) flanked by 5′ and 3′ untranslated regions (UTRs). Structural proteins in the N-terminal region are VP1-VP4, flanked by a leader protein (L) found in some species. Non-structural proteins in the C-terminal region are helicase (Hel), protease (Pro), and RNA-dependent RNA polymerase (RdRp). The 5′ end has a genome-linked viral protein (VPg), and the 3′ has a poly-A tail (AAA_n) (76).

1.2.4 Untranslated regions

UTRs are flanking regions at the viral genome's 5′ and 3′ ends (**Figure 1.2**). Unlike the ORF, these regions do not encode proteins but play essential roles in the viral life cycle. In Iflaviruses, the length of UTRs varies significantly between species. For example, the 5′ UTR

varies significantly in size, from the shorter 188 nt region of SBV to the larger 1165 nt region of DWV. The 3′ UTRs are usually shorter than the 5′ UTRs and are terminated by a 3′ poly-adenylated (poly-A) tail (54). Viral UTRs are important RNA segments involved in processes such as translation regulation, viral replication, RNA stability, and genome packaging (85-87). Most of the functional ability of the viral UTRs is fulfilled through their capability of hijacking host cellular factors (88,89). Additionally, the complex secondary and tertiary structures of these regions, including stem-loops, bulges, and pseudoknots, are crucial for their biological function (86). These structures facilitate the three-dimensional folding necessary for their roles in the viral life cycle.

The structures of UTRs are commonly studied using techniques such as small-angle X-ray scattering (SAXS), X-ray crystallography, nuclear magnetic resonance (NMR), and selective 2'-hydroxyl acylation analyzed by primer extension (SHAPE) (90-93). Picornaviruses have been shown to have an array of complex structures that interact with various host proteins to perform different functions (88,94). For example, the 3′ UTR of the foot-and-mouth disease virus (FMDV) is important for both viral replication and virulence (95). The UTR elicited an immune response in transfected porcine cells that relied on the secondary structure. Similarly, the 5′ UTRs of picornaviruses are widely known for mediating translation initiation through a specialized RNA element known as an internal ribosome entry site (IRES).

1.3 Internal ribosome entry sites

Many viruses have evolved to utilize IRESs to their advantage (96). Viral IRESs are structured RNA elements found in the UTRs of some viral genomes. Unlike typical eukaryotic cellular messenger RNAs that rely on a 7-methylguanosine (m^7G) cap at the 5′ end to recruit the ribosome and associated eukaryotic initiation factors (eIFs) for translation, IRES elements bypass this cap-dependent process (96,97). Instead, IRESs directly recruit the ribosome and host proteins to initiate translation in a cap-independent process. This mechanism is advantageous for viruses for several reasons. IRESs enable translation under conditions where cap-dependent initiation is inhibited (i.e., during viral infection or cellular stress), allowing efficient production of viral proteins (98). Some viruses that utilize IRESs encode proteases that cleave specific cellular eIFs, globally inhibiting cap-dependent translation while allowing the virus to continue translation through its IRES (99). It also enables translation initiation using a subset of canonical eIFs and noncanonical host proteins known as IRES trans-acting factors (ITAFs) (94).

Six main types of viral IRESs are classified based on their structure, mechanism, and factor requirements (94). The initially characterized class of Type I IRESs are found in enteroviruses and include the well-characterized poliovirus IRES (100). They interact with all the eIFs except the cap-binding protein eIF4E and various ITAFs, such as poly(C) binding protein-2 (PCBP2) (101,102). Type II IRESs are present in the aphtho-/cardioviruses, including encephalomyocarditis virus (EMCV) and FMDV (103). Like Type I IRESs, Type II requires eIFs and ITAFs, except the eIF4E. Important positively regulating ITAFs for the FMDV IRES include polypyrimidine tract-binding protein (PTB) (104) and $ITAF_{45}$ (105). Type III IRESs are found in the hepatitis A virus (106). Translation initiation for the six domains of the hepatitis A virus is very inefficient; therefore, all initiation factors are required, including eIF4E (107). This

type of IRES is also regulated by various ITAFs, including PCBP2 (108) and PTB (109). Type IV IRESs include flaviviruses such as hepatitis C virus and other picornaviruses such as sapelovirus A (110). Unlike the other IRES types, the hepatitis C virus IRES can directly recruit an eIF-free 40S ribosomal subunit (111). Type V IRESs are found in kobu-/sali-/osciviruses, including the Aichi virus A (112). PTB also enhances this type and is uniquely shown to depend on DExH-box helicase 29 (112). The newly designated Type VI IRES includes dicistrovirus intergenic region (IGR) IRESs, including cricket paralysis virus (113). These IRESs are compact and utilize a streamlined mechanism for initiation, where initiation factors are not required (114).

1.3.1. Iflavirus IRESs

In Iflaviruses, IRES-mediated translation is believed to play a crucial role in the viral life cycle (35). Initially, it was thought that Iflaviruses do not have IRES elements because of their small 5′ UTR compared to most picornaviruses (115). Despite this, a handful of Iflaviruses have been identified to have an IRES, including VDV-1, *Ectropis obliqua* picorna-like virus (EoPV), *Perina nuda* virus (PnV), and *Bombyx mori* infectious flacherie virus (IFV) (116-119). These studies showed that the 5′ UTRs could initiate translation through *in vitro* and/or *in vivo* systems.

Bicistronic reporter systems are commonly used to determine the IRES activity of a sequence (120). For example, Lu et al. (121) used a system where the EoPV 5′ UTR was inserted between two luciferase cistrons: *Renilla* luciferase (RLuc) and firefly luciferase (FLuc). The translation of RLuc relies on cap-dependent initiation mechanisms and acts as a control, whereas the translation of the downstream FLuc depends on cap-independent mechanisms, such as an IRES (120). Lu et al. (121) determined that the EoPV 5′ UTR produced a high amount of FLuc compared to negative controls, both *in vitro* and in insect cells (121). The Iflavirus IRES

structures resemble the six types of known IRESs to some capacity; however, they have not been officially classified. Notable structural features include a three-branched or cloverleaf-like domain from VDV-1 and IFV resembling Type I IRESs (116,119). Additionally, IFV, EoPV, and PnV have a Y-shaped domain resembling Type II IRESs (118,119,121). However, the interactions between Iflavirus IRESs and host eIFs remain unexplored, an important step in helping classify these IRESs (35).

1.4 Thesis objectives

Currently, no direct treatments are available to treat honey bee viral infections. Research into understanding honey bee viruses and their life cycle is essential to developing antiviral therapeutics. An apparent knowledge gap exists in the role and influence of Iflaviral UTRs in the viral life cycle. By exploiting the structural features of UTRs and their interaction with host proteins, we can uncover novel therapeutic targets to disrupt specific viral replication mechanisms. Therefore, the overarching objectives of this thesis are to characterize the UTRs of two major honey bee viruses: SBV and DWV.

The first sub-objective is to biophysically characterize and analyze the structures of the SBV and DWV UTRs. Chapter 2 investigates the SBV 5′ and 3′ UTRs using small-angle X-ray scattering combined with computationally generated RNA models to elucidate their structures. Additionally, the function of the SBV 5′ UTR as an IRES is explored. Chapter 3 extends the biophysical analysis to the DWV 3′ UTR, offering insights into the UTR structure of a different Iflavirus. Gaining more insight into these regions' structures is crucial to understanding the life cycle of these viruses and helping further link viral RNA structure to function.

The second sub-objective is to investigate potential *A. mellifera* RNA-binding proteins that interact with the SBV 5′ and 3′ UTRs, as detailed in Chapter 4. This is accomplished through immunoprecipitation pull-down assays followed by mass spectrometry analysis. These experiments will determine proteins that bind to the SBV UTRs, providing further insight into the potential functional role of these regions. This thesis aims to provide a foundational understanding of the dynamic structures, functions, and RNA-host interactions of the SBV and DWV UTRs.

1.5 References

1. Osterman, J., Aizen, M.A., Biesmeijer, J.C., Bosch, J., Howlett, B.G., Inouye, D.W., Jung, C., Martins, D.J., Medel, R., Pauw, A. *et al.* (2021) Global trends in the number and diversity of managed pollinator species. *Agriculture, Ecosystems & Environment*, **322**.
2. Kevan, P.G., Clark, E.A. and Thomas, V.G. (1990) Insect pollinators and sustainable agriculture. *American Journal of Alternative Agriculture*, **5**, 13-22.
3. Khalifa, S.A.M., Elshafiey, E.H., Shetaia, A.A., El-Wahed, A.A.A., Algethami, A.F., Musharraf, S.G., AlAjmi, M.F., Zhao, C., Masry, S.H.D., Abdel-Daim, M.M. *et al.* (2021) Overview of bee pollination and its economic value for crop production. *Insects*, **12**.
4. Calderone, N.W. (2012) Insect pollinated crops, insect pollinators and US agriculture: trend analysis of aggregate data for the period 1992-2009. *PLoS One*, **7**, e37235.
5. Bohart, G.E. (1972) Management of wild bees for the pollination of crops. *Annual Review of Entomology*, **17**, 287-312.
6. Garibaldi, L.A., Steffan-Dewenter, I., Winfree, R., Aizen, M.A., Bommarco, R., Cunningham, S.A., Kremen, C., Carvalheiro, L.G., Harder, L.D., Afik, O. *et al.* (2013) Wild pollinators enhance fruit set of crops regardless of honey bee abundance. *Science*, **339**, 1608-1611.
7. Fontaine, C., Dajoz, I., Meriguet, J. and Loreau, M. (2006) Functional diversity of plant-pollinator interaction webs enhances the persistence of plant communities. *PLoS Biol*, **4**, e1.
8. Agriculture and Agri-Food Canada. (2024) Statistical overview of the Canadian honey and bee industry, 2023. Horticulture Section: Crops and Horticulture Division, April 2024; https://agriculture.canada.ca/en/sector/horticulture/reports/statistical-overview-canadian-honey-and-bee-industry-2023
9. Hoover, S.E. and Ovinge, L.P. (2018) Pollen collection, honey production, and pollination services: managing honey bees in an agricultural setting. *J Econ Entomol*, **111**, 1509-1516.
10. Government of Alberta. (2023) Economics of beekeeping in Alberta 2022. Agriculture and Irrigation, November 6, 2023; https://open.alberta.ca/dataset/751a8539-2c17-47af-aab3-a7e1d5dcee04/resource/14325fa1-05ef-4fde-83ae-cd9122752bf6/download/agi-economics-of-beekeeping-in-alberta-2022.pdf
11. Willcox, B.K., Potts, S.G., Brown, M.J.F., Alix, A., Al Naggar, Y., Chauzat, M.P., Costa, C., Gekiere, A., Hartfield, C., Hatjina, F. *et al.* (2023) Emerging threats and opportunities to managed bee species in European agricultural systems: a horizon scan. *Sci Rep*, **13**, 18099.
12. El-Seedi, H.R., Ahmed, H.R., El-Wahed, A.A.A., Saeed, A., Algethami, A.F., Attia, N.F., Guo, Z., Musharraf, S.G., Khatib, A., Alsharif, S.M. *et al.* (2022) Bee stressors from an immunological perspective and strategies to improve bee health. *Veterinary Sciences*, **9**.
13. Claing, G., Ellsworth, S., Ferland, J., Janser, M., Kempers, M., Kozak, P., Maund, C., Menzies, C., Micholson, D., Morfin, N. *et al.* (2023) Canadian Association of Professional Apiculturists (CAPA) statement on honey bee wintering losses in Canada

for 2023; https://capabees.com/shared/CAPA-Statement-on-Colony-Losses-2022-2023_final.pdf
14. Bee Informed Partnership. (2023) United States honey bee colony losses 2022-23: preliminary results from the Bee Informed Partnership. Retrieved from; https://beeinformed.org/2023/06/22/united-states-honey-bee-colony-losses-2022-23-preliminary-results-from-the-bee-informed-partnership/
15. Chaudhary, G.N. and Nasr, M. (2007) Estimation of potential economic losses for the Alberta beekeeping industry due to winter losses in 2007. Government of Alberta Industry Development Sector, October 5, 2007
16. Borba, R.S., Hoover, S.E., Currie, R.W., Giovenazzo, P., Guarna, M.M., Foster, L.J., Zayed, A. and Pernal, S.F. (2022) Phenomic analysis of the honey bee pathogen-web and its dynamics on colony productivity, health and social immunity behaviors. *PLoS One*, **17**, e0263273.
17. Williams, G.R., Troxler, A., Retschnig, G., Roth, K., Yanez, O., Shutler, D., Neumann, P. and Gauthier, L. (2015) Neonicotinoid pesticides severely affect honey bee queens. *Sci Rep*, **5**, 14621.
18. Le Conte, Y. and Navajas, M. (2008) Climate change: impact on honey bee populations and diseases. *Rev. Sci. Tech.*, **27**, 499-510.
19. Pernal, S. and Currie, R. (2001) The influence of pollen quality on foraging behavior in honeybees (*Apis mellifera* L.). *Behavioral Ecology and Sociobiology*, **51**, 53-68.
20. Mattila, H.R. and Otis, G.W. (2007) Dwindling pollen resources trigger the transition to broodless populations of long-lived honeybees each autumn. *Ecological Entomology*, **32**, 496-505.
21. Guzmán-Novoa, E., Eccles, L., Calvete, Y., McGowan, J., Kelly, P.G. and Correa-Benítez, A. (2010) *Varroa destructor* is the main culprit for the death and reduced populations of overwintered honey bee (*Apis mellifera*) colonies in Ontario, Canada. *Apidologie*, **41**, 443-450.
22. Genersch, E. (2010) Honey bee pathology: current threats to honey bees and beekeeping. *Appl Microbiol Biotechnol*, **87**, 87-97.
23. Staveley, J.P., Law, S.A., Fairbrother, A. and Menzie, C.A. (2014) A causal analysis of observed declines in managed honey bees (*Apis mellifera*). *Hum Ecol Risk Assess*, **20**, 566-591.
24. Hristov, P., Shumkova, R., Palova, N. and Neov, B. (2020) Factors associated with honey bee colony losses: a mini-review. *Vet Sci*, **7**.
25. Jack, C.J. and Ellis, J.D. (2021) Integrated pest management control of *Varroa destructor* (Acari: Varroidae), the most damaging pest of (*Apis mellifera* L. (Hymenoptera: Apidae)) colonies. *Journal of Insect Science*, **21**.
26. Grozinger, C.M., Underwood, R. and López-Uribe, M. (2023) Viruses in honey bees. PennState Extension; https://extension.psu.edu/viruses-in-honey-bees
27. Colwell, M.J., Pernal, S.F. and Currie, R.W. (2024) Treatment of waxborne honey bee (Hymenoptera: Apidae) viruses using time, temperature, and electron-beam irradiation. *J Econ Entomol*, **117**, 34-42.
28. Tantillo, G., Bottaro, M., Di Pinto, A., Martella, V., Di Pinto, P. and Terio, V. (2015) Virus infections of honeybees *Apis mellifera*. *Ital J Food Saf*, **4**, 5364.

29. Baker, A.C. and Schroeder, D.C. (2008) The use of RNA-dependent RNA polymerase for the taxonomic assignment of Picorna-like viruses (order *Picornavirales*) infecting *Apis mellifera* L. populations. *Virol J*, **5**, 10.
30. International Committee on Taxonomy of Viruses (ICTV). (2024) Virus Taxonomy: 2023 Release. Retrieved from; https://ictv.global/taxonomy
31. Le Gall, O., Christian, P., Fauquet, C.M., King, A.M., Knowles, N.J., Nakashima, N., Stanway, G. and Gorbalenya, A.E. (2008) *Picornavirales*, a proposed order of positive-sense single-stranded RNA viruses with a pseudo-T = 3 virion architecture. *Arch Virol*, **153**, 715-727.
32. Ghosh, R.C., Ball, B.V., Willcocks, M.M. and Carter, M.J. (1999) The nucleotide sequence of sacbrood virus of the honey bee: an insect picorna-like virus. *J Gen Virol*, **80 (Pt 6)**, 1541-1549.
33. Lanzi, G., de Miranda, J.R., Boniotti, M.B., Cameron, C.E., Lavazza, A., Capucci, L., Camazine, S.M. and Rossi, C. (2006) Molecular and biological characterization of deformed wing virus of honeybees (*Apis mellifera* L.). *J Virol*, **80**, 4998-5009.
34. de Miranda, J.R., Dainat, B., Locke, B., Cordoni, G., Berthoud, H., Gauthier, L., Neumann, P., Budge, G.E., Ball, B.V. and Stoltz, D.B. (2010) Genetic characterization of slow bee paralysis virus of the honeybee (*Apis mellifera* L.). *J Gen Virol*, **91**, 2524-2530.
35. van Oers, M.M. (2010) In Asgari, S. and Johnson, K. N. (eds.), *Insect Virology*. Caister Academic Press, Norfolk, U.K., pp. 231-250.
36. Beaurepaire, A., Piot, N., Doublet, V., Antunez, K., Campbell, E., Chantawannakul, P., Chejanovsky, N., Gajda, A., Heerman, M., Panziera, D. *et al.* (2020) Diversity and global distribution of viruses of the western honey bee, *Apis mellifera*. *Insects*, **11**.
37. Bailey, L. and Ball, B.V. (1991), *Honey Bee Pathology*, pp. 10-34.
38. Genersch, E., Yue, C., Fries, I. and de Miranda, J.R. (2006) Detection of deformed wing virus, a honey bee viral pathogen, in bumble bees (*Bombus terrestris* and *Bombus pascuorum*) with wing deformities. *J Invertebr Pathol*, **91**, 61-63.
39. Anderson, D.L. and Trueman, J.W.H. (2000) *Varroa jacobsoni* (Acari: Varroidae) is more than one species. *Experimental and Applied Acarology*, **24**, 165-189.
40. Rosenkranz, P., Aumeier, P. and Ziegelmann, B. (2010) Biology and control of *Varroa destructor*. *J Invertebr Pathol*, **103 Suppl 1**, S96-119.
41. Boecking, O. and Genersch, E. (2008) Varroosis – the ongoing crisis in bee keeping. *J Verbr Lebensm*, **3**, 221-228.
42. Bowen-Walker, P.L., Martin, S.J. and Gunn, A. (1999) The transmission of deformed wing virus between honeybees (*Apis mellifera* L.) by the ectoparasitic mite *Varroa jacobsoni* Oud. *Journal of Invertebrate Pathology*, **73**, 101-106.
43. Ramsey, S.D., Ochoa, R., Bauchan, G., Gulbronson, C., Mowery, J.D., Cohen, A., Lim, D., Joklik, J., Cicero, J.M., Ellis, J.D. *et al.* (2019) *Varroa destructor* feeds primarily on honey bee fat body tissue and not hemolymph. *Proc Natl Acad Sci U S A*, **116**, 1792-1801.
44. Yang, X. and Cox-Foster, D. (2007) Effects of parasitization by *Varroa destructor* on survivorship and physiological traits of *Apis mellifera* in correlation with viral incidence and microbial challenge. *Parasitology*, **134**, 405-412.
45. Dainat, B., Evans, J.D., Chen, Y.P., Gauthier, L. and Neumann, P. (2012) Dead or alive: deformed wing virus and *Varroa destructor* reduce the life span of winter honeybees. *Appl Environ Microbiol*, **78**, 981-987.

46. de Miranda, J.R. and Genersch, E. (2010) Deformed wing virus. *J Invertebr Pathol*, **103 Suppl 1**, S48-61.
47. Iqbal, J. and Mueller, U. (2007) Virus infection causes specific learning deficits in honeybee foragers. *Proc Biol Sci*, **274**, 1517-1521.
48. Traniello, I.M., Bukhari, S.A., Kevill, J., Ahmed, A.C., Hamilton, A.R., Naeger, N.L., Schroeder, D.C. and Robinson, G.E. (2020) Meta-analysis of honey bee neurogenomic response links deformed wing virus type A to precocious behavioral maturation. *Sci Rep*, **10**, 3101.
49. Chen, Y.P., Higgins, J.A. and Feldlaufer, M.F. (2005) Quantitative real-time reverse transcription-PCR analysis of deformed wing virus infection in the honeybee (*Apis mellifera* L.). *Appl Environ Microbiol*, **71**, 436-441.
50. Chen, Y., Evans, J. and Feldlaufer, M. (2006) Horizontal and vertical transmission of viruses in the honey bee, *Apis mellifera*. *J Invertebr Pathol*, **92**, 152-159.
51. Yue, C. and Genersch, E. (2005) RT-PCR analysis of deformed wing virus in honeybees (*Apis mellifera*) and mites (*Varroa destructor*). *J Gen Virol*, **86**, 3419-3424.
52. Yue, C., Schroder, M., Gisder, S. and Genersch, E. (2007) Vertical-transmission routes for deformed wing virus of honeybees (*Apis mellifera*). *J Gen Virol*, **88**, 2329-2336.
53. Amiri, E., Meixner, M.D. and Kryger, P. (2016) Deformed wing virus can be transmitted during natural mating in honey bees and infect the queens. *Sci Rep*, **6**, 33065.
54. Ongus, J.R., Peters, D., Bonmatin, J.M., Bengsch, E., Vlak, J.M. and van Oers, M.M. (2004) Complete sequence of a picorna-like virus of the genus *Iflavirus* replicating in the mite *Varroa destructor*. *J Gen Virol*, **85**, 3747-3755.
55. Mordecai, G.J., Wilfert, L., Martin, S.J., Jones, I.M. and Schroeder, D.C. (2016) Diversity in a honey bee pathogen: first report of a third master variant of the deformed wing virus quasispecies. *ISME J*, **10**, 1264-1273.
56. McMahon, D.P., Natsopoulou, M.E., Doublet, V., Furst, M., Weging, S., Brown, M.J., Gogol-Doring, A. and Paxton, R.J. (2016) Elevated virulence of an emerging viral genotype as a driver of honeybee loss. *Proc Biol Sci*, **283**.
57. Paxton, R.J., Schafer, M.O., Nazzi, F., Zanni, V., Annoscia, D., Marroni, F., Bigot, D., Laws-Quinn, E.R., Panziera, D., Jenkins, C. *et al.* (2022) Epidemiology of a major honey bee pathogen, deformed wing virus: potential worldwide replacement of genotype A by genotype B. *Int J Parasitol Parasites Wildl*, **18**, 157-171.
58. Kevill, J.L., de Souza, F.S., Sharples, C., Oliver, R., Schroeder, D.C. and Martin, S.J. (2019) DWV-A lethal to honey bees (*Apis mellifera*): a colony level survey of DWV variants (A, B, and C) in England, Wales, and 32 states across the US. *Viruses*, **11**.
59. Francis, R.M., Nielsen, S.L. and Kryger, P. (2013) Varroa-virus interaction in collapsing honey bee colonies. *PLoS One*, **8**, e57540.
60. Fujiyuki, T., Takeuchi, H., Ono, M., Ohka, S., Sasaki, T., Nomoto, A. and Kubo, T. (2004) Novel insect picorna-like virus identified in the brains of aggressive worker honeybees. *J Virol*, **78**, 1093-1100.
61. Huang, W.F. (2023) Editorial: obstacles, advantages, and recent progress in honey bee virus research. *Front Insect Sci*, **3**, 878344.
62. Grindrod, I., Kevill, J.L., Villalobos, E.M., Schroeder, D.C. and Martin, S.J. (2021) Ten years of deformed wing virus (DWV) in Hawaiian honey bees (*Apis mellifera*), the dominant DWV-A variant Is potentially being replaced by variants with a DWV-B coding sequence. *Viruses*, **13**.

63. Morfin, N., Foster, L.J., Guzman-Novoa, E., Van Westendorp, P., Currie, R.W. and Higo, H. (2024) *Varroa destructor* economic injury levels and pathogens associated with colony losses in Western Canada. *Frontiers in Bee Science*, **2**.
64. de Miranda, J.R., Brettell, L.E., Chejanovsky, N., Childers, A.K., Dalmon, A., Deboutte, W., de Graaf, D.C., Doublet, V., Gebremedhn, H., Genersch, E. *et al.* (2022) Cold case: The disappearance of Egypt bee virus, a fourth distinct master strain of deformed wing virus linked to honeybee mortality in 1970's Egypt. *Virol J*, **19**, 12.
65. White, G.F. (1913) *Sacbrood, a disease of bees*. US Department of Agriculture, Bureau of Entomology, Washington, DC, USA.
66. Bailey, L., Gibbs, A.J. and Woods, R.D. (1964) Sacbrood virus of the larval honey bee (*Apis mellifera* Linnaeus). *Virology*, **23**, 425-429.
67. Wei, R., Cao, L., Feng, Y., Chen, Y., Chen, G. and Zheng, H. (2022) Sacbrood virus: a growing threat to honeybees and wild pollinators. *Viruses*, **14**, 1871.
68. Grabensteiner, E., Ritter, W., Carter, M.J., Davison, S., Pechhacker, H., Kolodziejek, J., Boecking, O., Derakhshifar, I., Moosbeckhofer, R., Licek, E. *et al.* (2001) Sacbrood virus of the honeybee (*Apis mellifera*): rapid identification and phylogenetic analysis using reverse transcription-PCR. *Clin Diagn Lab Immunol*, **8**, 93-104.
69. Ball, B.V. and Bailey, L. (1997) In Morse, R. A. and Flottum, K. (eds.), *Honey Bee Pests, Predators, & Disease*. The A. I. Root Company, Medina, OH, USA, pp. 11-31.
70. Chen, Y.P. and Siede, R. (2007) Honey bee viruses. *Adv Virus Res*, **70**, 33-80.
71. Bailey, L. and Fernando, E.F.W. (1972) Effects of sacbrood virus on adult honey-bees. *Annals of Applied Biology*, **72**, 27-35.
72. Shen, M., Cui, L., Ostiguy, N. and Cox-Foster, D. (2005) Intricate transmission routes and interactions between picorna-like viruses (Kashmir bee virus and sacbrood virus) with the honeybee host and the parasitic varroa mite. *J Gen Virol*, **86**, 2281-2289.
73. Li, J., Wang, T., Evans, J.D., Rose, R., Zhao, Y., Li, Z., Li, J., Huang, S., Heerman, M., Rodriguez-Garcia, C. *et al.* (2019) The phylogeny and pathogenesis of Sacbrood virus (SBV) infection in European honey bees, *Apis mellifera*. *Viruses*, **11**.
74. Guo, Y., Goodman, C.L., Stanley, D.W. and Bonning, B.C. (2020) Cell lines for honey bee virus research. *Viruses*, **12**, 236.
75. Prochazkova, M., Skubnik, K., Fuzik, T., Mukhamedova, L., Pridal, A. and Plevka, P. (2020) Virion structures and genome delivery of honeybee viruses. *Curr Opin Virol*, **45**, 17-24.
76. Valles, S.M., Chen, Y., Firth, A.E., Guerin, D.M.A., Hashimoto, Y., Herrero, S., de Miranda, J.R., Ryabov, E. and ICTV Report Consortium. (2017) ICTV virus taxonomy profile: *Iflaviridae*. *J Gen Virol*, **98**, 527-528.
77. Hashimoto, Y., Watanabe, A. and Kawase, S. (1984) *In vitro* translation of infectious flacherie virus RNA in a wheat germ and a rabbit reticulocyte system. *Biochimica et Biophysica Acta*, **781**, 76-80.
78. Kadaré, K. and Haenni, A. (1997) Virus-encoded RNA helicases. *Journal of Virology*, **71**, 2583-2590.
79. Cheng, Z., Yang, J., Xia, H., Qiu, Y., Wang, Z., Han, Y., Xia, X., Qin, C.F., Hu, Y. and Zhou, X. (2013) The nonstructural protein 2C of a picorna-like virus displays nucleic acid helix destabilizing activity that can be functionally separated from its ATPase activity. *J Virol*, **87**, 5205-5218.

80. Ye, S., Xia, H., Dong, C., Cheng, Z., Xia, X., Zhang, J., Zhou, X. and Hu, Y. (2012) Identification and characterization of Iflavirus 3C-like protease processing activities. *Virology*, **428**, 136-145.
81. Lin, M., Ye, S., Xiong, Y., Cai, D., Zhang, J. and Hu, Y. (2010) Expression and characterization of RNA-dependent RNA polymerase of *Ectropis obliqua* virus. *BMB Rep.*, **43**, 284-290.
82. Kok, C.C. and McMinn, P.C. (2009) Picornavirus RNA-dependent RNA polymerase. *Int J Biochem Cell Biol*, **41**, 498-502.
83. Hashimoto, Y., Watanabe, A. and Kawase, S. (1986) Evidence for the presence of a genome-linked protein in infectious flacherie virus. *Arch Virol*, **90**, 301-312.
84. Lee, Y.F., Nomoto, A., Detjen, B.M. and Wimmer, E. (1977) A protein covalently linked to poliovirus genome RNA. *Proc Natl Acad Sci U S A*, **74**, 59-63.
85. Kloc, A., Rai, D.K. and Rieder, E. (2018) The roles of picornavirus untranslated regions in infection and innate immunity. *Front Microbiol*, **9**, 485.
86. Liu, Y., Zhang, Y., Wang, M., Cheng, A., Yang, Q., Wu, Y., Jia, R., Liu, M., Zhu, D., Chen, S. *et al.* (2020) Structures and functions of the 3′ untranslated regions of positive-sense single-stranded RNA viruses infecting humans and animals. *Front Cell Infect Microbiol*, **10**, 453.
87. Ng, W.C., Soto-Acosta, R., Bradrick, S.S., Garcia-Blanco, M.A. and Ooi, E.E. (2017) The 5′ and 3′ untranslated regions of the flaviviral genome. *Viruses*, **9**.
88. Lin, J.Y., Chen, T.C., Weng, K.F., Chang, S.C., Chen, L.L. and Shih, S.R. (2009) Viral and host proteins involved in picornavirus life cycle. *J Biomed Sci*, **16**, 103.
89. Vidalain, P.O. and Tangy, F. (2010) Virus-host protein interactions in RNA viruses. *Microbes Infect*, **12**, 1134-1143.
90. Jackson, R.W., Smathers, C.M. and Robart, A.R. (2023) General strategies for RNA X-ray crystallography. *Molecules*, **28**.
91. Chen, J.L., Bellaousov, S. and Turner, D.H. (2016), *RNA Structure Determination*, pp. 177-186.
92. Chen, Y. and Pollack, L. (2016) SAXS studies of RNA: structures, dynamics, and interactions with partners. *Wiley Interdiscip Rev RNA*, **7**, 512-526.
93. Deigan, K.E., Li, T.W., Mathews, D.H. and Weeks, K.M. (2009) Accurate SHAPE-directed RNA structure determination. *PNAS*, **106**, 97-102.
94. Abdullah, S.W., Wu, J., Wang, X., Guo, H. and Sun, S. (2023) Advances and breakthroughs in IRES-directed translation and replication of picornaviruses. *mBio*, **14**.
95. Rodríguez-Pulido, M., Borrego, B., Sobrino, F. and Saiz, M. (2011) RNA structural domains in noncoding regions of the foot-and-mouth disease virus genome trigger innate immunity in porcine cells and mice. *J Virol*, **85**, 6492-6501.
96. Jan, E. (2006) Divergent IRES elements in invertebrates. *Virus Res*, **119**, 16-28.
97. Merrick, W.C. and Pavitt, G.D. (2018) Protein synthesis initiation in eukaryotic cells. *Cold Spring Harb Perspect Biol*, **10**.
98. Komar, A.A. and Hatzoglou, M. (2005) Internal ribosome entry sites in cellular mRNAs: mystery of their existence. *J Biol Chem*, **280**, 23425-23428.
99. Jaafar, Z.A. and Kieft, J.S. (2019) Viral RNA structure-based strategies to manipulate translation. *Nature Reviews Microbiology*, **17**, 110-123.
100. Pelletier, J. and Sonenberg, N. (1988) Internal initiation of translation of eukaryotic mRNA directed by a sequence derived from poliovirus RNA. *Nature*, **334**, 320-325.

101. Mailliot, J. and Martin, F. (2018) Viral internal ribosomal entry sites: four classes for one goal. *Wiley Interdiscip Rev RNA*, **9**.
102. Blyn, L.B., Swiderek, K.M., Richards, O., Stahl, D.C., Semler, B.L. and Ehrenfeld, E. (1996) Poly(rC) binding protein 2 binds to stem-loop IV of the poliovirus RNA 5′ noncoding region: Identification by automated liquid chromatography-tandem mass spectrometry. *Proc Natl Acad Sci U S A*, **93**, 11115-11120.
103. Martinez-Salas, E., Francisco-Velilla, R., Fernandez-Chamorro, J., Lozano, G. and Diaz-Toledano, R. (2015) Picornavirus IRES elements: RNA structure and host protein interactions. *Virus Res*, **206**, 62-73.
104. Niepmann, M., Peterson, A., Meyer, K. and Beck, E. (1997) Functional involvement of polypyrimidine tract-binding protein in translation initiation complexes with the internal ribosome entry site of foot-and-mouth disease virus. *Journal of Virology*, **71**, 8330-8339.
105. Pilipenko, E.V., Pestova, T.V., Kolupaeva, V.G., Khitrina, E.V., Poperechnaya, A.N., Agol, V.I. and Hellen, C.U.T. (2000) A cell cycle-dependent protein serves as a template-specific translation initiation factor. *Genes & Development*, **14**, 2028-2045.
106. Brown, E.A., Zajac, A.J. and Lemon, S.M. (1994) *In vitro* characterization of an internal ribosome site (IRES) present within the 5′ nontranslated region of hepatitis A virus RNA: comparison with the IRES of encephalomyocarditis virus. *Journal of Virology*, **68**, 1066-1074.
107. Ali, I.K., McKendrick, L., Morley, S.J. and Jackson, R.J. (2001) Activity of the hepatitis A virus IRES requires association between the cap-binding translation initiation factor (eIF4E) and eIF4G. *J Virol*, **75**, 7854-7863.
108. Graff, J., Cha, J., Blyn, L.B. and Ehrenfeld, E. (1998) Interaction of poly(rC) binding protein 2 with the 5′ noncoding region of hepatitis A virus RNA and its effects on translation. *Journal of Virology*, **72**, 9668-9675.
109. Gosert, R., Chang, K.H., Rijnbrand, R., Yi, M., Sangar, D.V. and Lemon, S.M. (2000) Transient expression of cellular polypyrimidine-tract binding protein stimulates cap-independent translation directed by both picornaviral and flaviviral internal ribosome entry sites *in vivo*. *Molecular and Cellular Biology*, **20**, 1583-1595.
110. Arhab, Y., Bulakhov, A.G., Pestova, T.V. and Hellen, C.U.T. (2020) Dissemination of internal ribosomal entry sites (IRES) between viruses by horizontal gene transfer. *Viruses*, **12**, 612.
111. Pestova, T.V., Shatsky, I.N., Fletcher, S.P., Jackson, R.J. and Hellen, C.U.T. (1998) A prokaryotic-like mode of cytoplasmic eukaryotic ribosome binding to the initiation codon during internal translation initiation of hepatitis C and classical swine fever virus RNAs. *Genes & Development*, **12**, 67-83.
112. Yu, Y., Sweeney, T.R., Kafasla, P., Jackson, R.J., Pestova, T.V. and Hellen, C.U. (2011) The mechanism of translation initiation on Aichivirus RNA mediated by a novel type of picornavirus IRES. *EMBO J*, **30**, 4423-4436.
113. Abaeva, I.S., Young, C., Warsaba, R., Khan, N., Tran, L.V., Jan, E., Pestova, T.V. and Hellen, C.U.T. (2023) The structure and mechanism of action of a distinct class of dicistrovirus intergenic region IRESs. *Nucleic Acids Res*, **51**, 9294-9313.
114. Deniz, N., Lenarcic, E.M., Landry, D.M. and Thompson, S.R. (2009) Translation initiation factors are not required for Dicistroviridae IRES function *in vivo*. *RNA*, **15**, 932-946.

115. Christian, P.D., Carstens, E.B., Domier, L., Johnson, J., Johnson, K.N., Nakashima, N., Scotti, P.D. and van der Wilk, F. (2005) In Fauquet, C. M., Mayo, M. A., Maniloff, J., Desselberger, U. and Ball, L. A. (eds.), *Virus Taxonomy: Classification and nomenclature of viruses: Eighth report of the International Committee on the Taxonomy of Viruses*. Academic Press, San Diego, USA.
116. Ongus, J.R., Roode, E.C., Pleij, C.W.A., Vlak, J.M. and van Oers, M.M. (2006) The 5′ non-translated region of *Varroa destructor* virus 1 (genus *Iflavirus*): structure prediction and IRES activity in *Lymantria dispar* cells. *J Gen Virol*, **87**, 3397-3407.
117. Lu, J., Hu, Y., Hu, L., Zong, S., Cai, D., Wang, J., Yu, H. and Zhang, J. (2007) *Ectropis obliqua* picorna-like virus IRES-driven internal initiation of translation in cell systems derived from different origins. *J Gen Virol*, **88**, 2834-2838.
118. Wu, T.Y., Wu, C.Y., Chen, Y.J., Chen, C.Y. and Wang, C.H. (2007) The 5′ untranslated region of *Perina nuda* virus (PnV) possesses a strong internal translation activity in baculovirus-infected insect cells. *FEBS Lett*, **581**, 3120-3126.
119. Li, M., Man, N., Qiu, H., Cai, S., He, X., He, X. and Lu, X. (2012) Detection of an internal translation activity in the 5′ region of *Bombyx mori* infectious flacherie virus. *Appl Microbiol Biotechnol*, **95**, 697-705.
120. Thompson, S.R. (2012) So you want to know if your message has an IRES? *Wiley Interdiscip Rev RNA*, **3**, 697-705.
121. Lu, J., Zhang, J., Wang, X., Jiang, H., Liu, C. and Hu, Y. (2006) *In vitro* and *in vivo* identification of structural and sequence elements in the 5′ untranslated region of Ectropis obliqua picorna-like virus required for internal initiation. *J Gen Virol*, **87**, 3667-3677.

Chapter 2: Structural and Functional Insights into Sacbrood Virus Untranslated Regions (UTRs) Reveal an Internal Ribosome Entry Site in the 5′ UTR

2.1 Foreword

This chapter consists of a manuscript that has been submitted to *Communications Biology*. Any formatting differences are to fulfill the submission requirements of the journal. Worked conducted for this chapter was performed jointly with Subash Chapagain, Dr. Higor Pereira, SarahAnn Walker, Dr. Luc Roberts, Dr. Shelley Hoover, Dr. Eric Jan, and Dr. Trushar Patel. This study was in collaboration with Dr. Jan's laboratory at the University of British Columbia. I conducted wet laboratory experiments with assistance from SarahAnn Walker. Subash Chapagain (Jan Group) performed the *in vitro* and *in vivo* bicistronic reporter assays. Dr. Pereira assisted with SAXS analysis and computational modelling. I wrote the manuscript with input and edits from Dr. Jan, Dr. Hoover, Dr. Roberts, Dr. Pereira, Subash, and Dr. Patel.

2.2 Abstract

The untranslated regions (UTRs) of RNA viruses are critical for viral replication. Many viruses have evolved to exploit an internal ribosome entry site (IRES) within their 5′ UTRs to enable cap-independent translation initiation in host cells. Sacbrood virus (SBV), a honey bee virus from the picorna-like *Iflaviridae* family, shares this feature with other Iflaviruses that have demonstrated IRES activity, though the presence of an IRES in SBV has not been confirmed experimentally prior to our work. Additionally, the structural features of SBV UTRs, remain unexplored. In this study, we present a biophysical characterization and structural determination of SBV UTRs. We identified a distinct multi-branched stem-loop structure in the SBV 5′ UTR, alongside an elongated 3′ UTR. Importantly, we discovered an IRES region within the SBV 5′ UTR and confirmed its ability to mediate IRES-dependent translation *in vitro* through a bicistronic reporter assay. Deletion mutant analysis further localized the essential IRES activity to a 39-nucleotide segment. Additionally, we demonstrated that the full-length SBV 5′ UTR exhibits IRES activity *in vivo*, and deletion of the minimal region abrogates this function. These findings provide the first experimental evidence that the SBV 5′ UTR adopts a unique structure capable of acting as an IRES.

2.3 Introduction

The western honey bee (*Apis mellifera* L.) is widely used in agriculture for pollination. It is estimated that pollination by the honey bee adds over $235-577 billion (US) to global crop output annually (1). Recently, honey bee colony mortality has increased, becoming a serious issue resulting in the significant over-winter decrease of managed honey bee populations (2). The cause of this mortality is multifaceted, with one major threat being pathogenic viruses primarily spread through varroa mites (3). Sacbrood virus (SBV), or *Morator aetatulas* virus, is one of the most common honey bee viruses found worldwide (4,5). SBV primarily affects young (~2 days old) larvae, causing failure to pupate and eventually death (6,7). Replicated viral particles accumulate in the ecdysial fluid underneath the larval skin, forming the characteristic sac-like appearance, and subsequent colour change from white to pale yellow and ultimately tan. SBV infection of adult honey bees, in contrast, is usually asymptomatic (8). SBV rarely leads to colony mortality in *A. mellifera*, however, it can significantly decrease the overall health and productivity of a colony (9). Currently, there are no treatments to specifically treat SBV or other honey bee viruses. The only preventative measures include removing contaminated combs, quarantining, and sterilizing equipment to reduce colony and yard transmission (8).

SBV belongs to the *Iflaviridae* family and has a positive-sense, single-stranded, 8861 nucleotides (nt) long RNA ((+) ssRNA) genome (10). The SBV genome contains a single open reading frame (ORF) that is translated into a polyprotein and then proteolytically processed to yield structural proteins (N-terminal) and non-structural proteins (C-terminal) (11,12). A 188 nt 5′ UTR and a 93 nt 3′ UTR flank the SBV ORF, and the viral RNA genome is polyadenylated (13).

The 5′ UTRs of some RNA viruses in the *Iflavirus* genus, including *Varroa destructor* virus 1 (VDV-1), *Ectropis obliqua* picorna-like virus (EoPV), *Perina nuda* virus (PnV), and *Bombyx mori* infectious flacherie virus (IFV) function as an internal ribosome entry site (IRES) (14-17). Viral IRES elements are structured RNAs that typically recruit a subset of translation factors to direct 5′-end- and cap-independent translation initiation (18). To date, viral IRESs are classified into six types based on sequence, RNA structure conservation, and factor requirements (19,20). The mechanism underlying Iflavirus IRES translation has not been investigated (12).

The 5′ UTR of SBV has been suspected to act as an IRES because of its classification in *Iflaviridae* (11). In this study, using small-angle X-ray scattering (SAXS) and computational modelling, we combined experimental low-resolution data with high-resolution models to generate 3-dimensional (3-D) structures of the SBV 5′ and 3′ UTRs. Furthermore, through a bicistronic reporter assay, we demonstrated that the full-length SBV 5′ UTR possesses IRES activity *in vitro*. Deletion mutant analyses mapped the functional IRES to a minimal 39 nt element and showed that the minimal IRES directed translation in *Drosophila melanogaster* Schneider 2 (S2) cells. This study suggests a novel IRES class utilized by the SBV 5′ UTR.

2.4 Materials and Methods

2.4.1 Plasmid design and constructs

Plasmid constructs were created to generate the 5′ and 3′ UTRs of SBV based on the GenBank accession code MG545286 (Azenta Life Sciences, USA). The cDNA sequences were prepared using a T7 RNA polymerase promoter with two additional G nucleotides on the 5′ end, followed by a HindIII restriction enzyme cut site (A^AGCTT) on the 3′ end. The RNA constructs used for *in vitro* transcription (IVT) are as follows:

1. SBV 5′ UTR (191 nt)
   5′GGGAAAUAAGAAUACGAAUCGUGAUUCGAUUCAUUGUUUCGCCUGAGUA
   AAUCGAGAUUUACCUUGACGGGGUUUGCUUGACGUUGCGUCAGACCCGUU
   UUCCUUGUGAUUUUUAGGUUGUGAAGAUUUAUUCGAGGAAGUUAAUUAAA
   CAGAAAGUUUAUUAUAUAGACAGAGACAUAAUAAGUUUAUUA 3′

2. SBV 3′ UTR (96 nt)
   5′GGUGUUUUUUAAGGUCUCAUAUAUGCUAUAAAGGUUAUGGGUACUAAUA
   UAGUGGAUUAAUAUCAAUAUAUGGCAUUUUAAAAAAAAAAAAAAAAAA 3′

The plasmids were transformed into *Escherichia coli* DH5α competent cells and were purified using GeneJET Plasmid Maxiprep Kits (Thermo Fisher Scientific, USA) as per the manufacturer's instructions.

Full-length SBV 5′ UTR was cloned into bicistronic luciferase reporter plasmid using Gibson assembly (21). The UTR sequence is upstream of the firefly luciferase (FLuc) ORF and downstream of the *Renilla* luciferase (RLuc) ORF. Plasmids were created containing five truncated versions of the SBV 5′ UTR sequence (Azenta Life Sciences, USA). The deletions are as follows: Δ1-50, Δ1-92, Δ1-131, Δ155-195, and Δ121-195. Each sequence was flanked with a 5′ EcoRI site and a 3′ NarI site for use in cloning into the bicistronic reporter plasmid. Assembled plasmids were verified by Sanger sequencing (Azenta Life Sciences, USA).

2.4.2 RNA purification

Purified plasmid constructs were linearized by HindIII restriction endonuclease (New England Biolabs, Canada). IVT reactions were performed using in-house T7 RNA polymerase, followed by the purification of synthesized RNA by size exclusion chromatography (SEC), following previous protocols (22). RNA fractions were eluted using RNA buffer (10 mM Bis-tris pH 6.0, 100 mM NaCl, 15 mM KCl, 5 mM $MgCl_2$, and 5% glycerol) and were pooled before ethanol precipitation overnight. RNA pellets were resuspended in RNA buffer to a concentration around 1.0-2.0 mg/mL for use downstream. The integrity of the RNA was analyzed using 2% nondenaturing agarose gel electrophoresis and 8% denaturing urea polyacrylamide gel electrophoresis (PAGE).

2.4.3 Multi-angle light scattering (MALS)

SEC-coupled multi-angle light scattering (MALS) was performed on a DAWN Multi-angle Light Scatterer with Optilab Refractive Index System (Wyatt Technology Corporation, Santa Barbara, CA, USA). RNA samples were purified through a Shodex KW403-4F (Showa Denko America Inc., New York, NY, USA) SEC column that was in succession with the light scattering system. Samples were run at a flow rate of 0.160 mL/min and were measured using 18 multi-angle detectors. All experiments were performed at room temperature (21°C). The concentration of 5′ and 3′ UTRs used was 1.7 and 1.0 mg/mL, respectively. The SBV 3′ UTR was heated at 95°C for 5 minutes and snap-cooled on ice before loading. Before data analyses, the refractive index increment (dn/dc) was adjusted to 0.196 mL/g for both UTRs. The ASTRA v8.0.0.25 software package was used to analyze data and determine the absolute molecular weight (M_W), as described before (22,23).

2.4.4 Small-angle X-ray scattering (SAXS)

The B21 beamline at Diamond Light Source (Didcot, Oxfordshire, UK) was used to collect small-angle X-ray scattering (SAXS) data. An Agilent 1200 high-performance liquid chromatography (HPLC) system equipped with a specialized flow cell was used, as previously described (24). A Shodex KW403-4F SEC column was used at a flow rate of 0.160 mL/min using RNA buffer. The concentrations of each RNA were as mentioned previously (Section 2.4.3). The SBV 3′ UTR was heated and cooled as mentioned previously. Samples were exposed to X-rays for 3 seconds of exposure time for a total of 600 frames.

Data analyses were performed using the ATSAS suite (25). CHROMIXS (26) was initially used on each raw data set to subtract for buffer contribution. To determine the radius of gyration (R_g) and the homogeneity of the samples, Guinier analysis was performed (q^2 vs. ln(I(q))) (27). The folding state of the RNA was determined using dimensionless Kratky analysis (qR_g vs. qR_g^2*I(q)/I(0)) (28). To obtain real space R_g and the maximum dimension (D_{max}) of the RNAs, paired distance distribution (P(r)) plots were made (29). By inputting the P(r) data into DAMMIN (30), we generated fifty models for SBV 5′ and twenty models for SBV 3′. Using these models, an average and filtered model for each RNA was generated using DAMAVER and DAMFILT (31).

2.4.5 Tertiary structure model fitting

RNAfold WebServer from the Vienna RNA Websuite (32,33) was used to generate secondary structure predictions for SBV 5′ and 3′ UTRs. The lowest free energy structures were selected and inputted as secondary structure constraints into SimRNA v3.20 (34) to obtain 3-D tertiary models of each RNA. A total of 1000 clusters for SBV 3′ and 20000 for SBV 5′ were

generated. DAMSUP (31) was used to align the tertiary models of each RNA to the SAXS models and calculate normalized spatial discrepancy (NSD). Finally, CRYSOL (35) was used to determine the fit of the atomistic structures to the experimental data by calculating the goodness of fit parameter (X^2). The best representative models were filtered using X^2, R_g, and NSD values. The models were visually represented using UCSF ChimeraX-1.8 (36).

2.4.6 Bicistronic luciferase assays

Bicistronic plasmids were linearized by BamHI restriction enzyme (New England Biolabs, Canada). RNA was transcribed using T7 RNA polymerase and subsequently purified with an RNA cleanup kit (New England Biolabs, Canada). 5′ capping was performed post-transcriptionally (CellScript). RNA integrity and purity were confirmed by denaturing agarose gel electrophoresis, and concentration was measured with a spectrophotometer (Nanodrop). *In vitro* transcribed RNAs were incubated in insect *Spodoptera frugiperda* (Sf) 21 cell lysates (Promega) for 1.5 hours at 30 °C (37). Reactions were either in the presence or absence of salt (0.5 $MgCl_2$, 40 mM KOAc). The reactions were analyzed for enzymatic luciferase activity using a dual luciferase kit (Promega) in a Tecan Spark-10M Multimode plate reader.

2.4.7 Cell culturing and transfection

D. melanogaster S2 cells were maintained in Shields and Sang M3 insect medium (Sigma-Aldrich, St. Louis, MI, USA) supplemented with 10% fetal bovine serum at 25°C (38). S2 cells (2.5×10^6) were transfected with capped bicistronic RNA (2 μg) using Lipofectamine 2000 reagent (Invitrogen). For monitoring reporter RNA translation, cells were harvested 6 hours post-transfection and lysed in 1X passive lysis buffer (Promega). Lysates were cleared, and protein concentration was measured by Bradford assay (Bio-Rad, Hercules, CA, USA). To

measure luciferase enzymatic activity, 5 μg of total protein was used with the dual luciferase reporter assay kit (Promega) according to the manufacturer's protocol.

2.5 Results and Discussion

2.5.1 Purification and absolute molecular weight determination of SBV UTRs

We investigated the absolute M_Ws of the purified SBV UTRs. *In vitro* transcribed RNAs were purified using SEC, leading to elution profiles for SBV 5′ and 3′ UTR (**Figure 2.1A**), with peaks at 12.2 mL and 14.2 mL, respectively. The SBV 3′ UTR had a single uniform peak, representing a single RNA species that was used for subsequent experiments. For the SBV 5′ UTR, the oligomeric species eluting from ~8-11 mL was removed, and peak fractions from ~11.5 to ~13 mL were selected to ensure only monodisperse and pure RNA was used for subsequent experiments. Nondenaturing and denaturing agarose gel electrophoresis were used to confirm the size and integrity of the RNAs (**Figure 2.1B** and **S2.1**). The gels confirmed the mass of the RNAs (191 nt and 96 nt for SBV 5′ and 3′ UTRs, respectively), yielding monodisperse and pure samples. Furthermore, SEC-MALS was used to determine the absolute M_W of the RNAs, as MALS employs scattered light from RNA molecules measured at various angles to calculate the M_W. SEC-MALS resulted in uniform peaks with relatively uniform absolute M_Ws for both RNAs (**Figures 2.1C** and **D**), indicating that the samples are homogenous. The SBV 5′ UTR was calculated to have an absolute M_W of 61.26 ± 0.27 kDa (**Figure 2.1C**), which is within ~0.3% of the theoretical M_W of 61.44 kDa. The SBV 3′ UTR was calculated to be 31.16 ± 0.54 kDa (**Figure 2.1D**), also closely matching the theoretical M_W of 30.95 kDa, with a difference of ~0.7%. The MALS results confirmed the homogeneity and monodispersity of the RNAs, verifying the appropriateness to proceed with SAXS to determine their 3-D structures in solution.

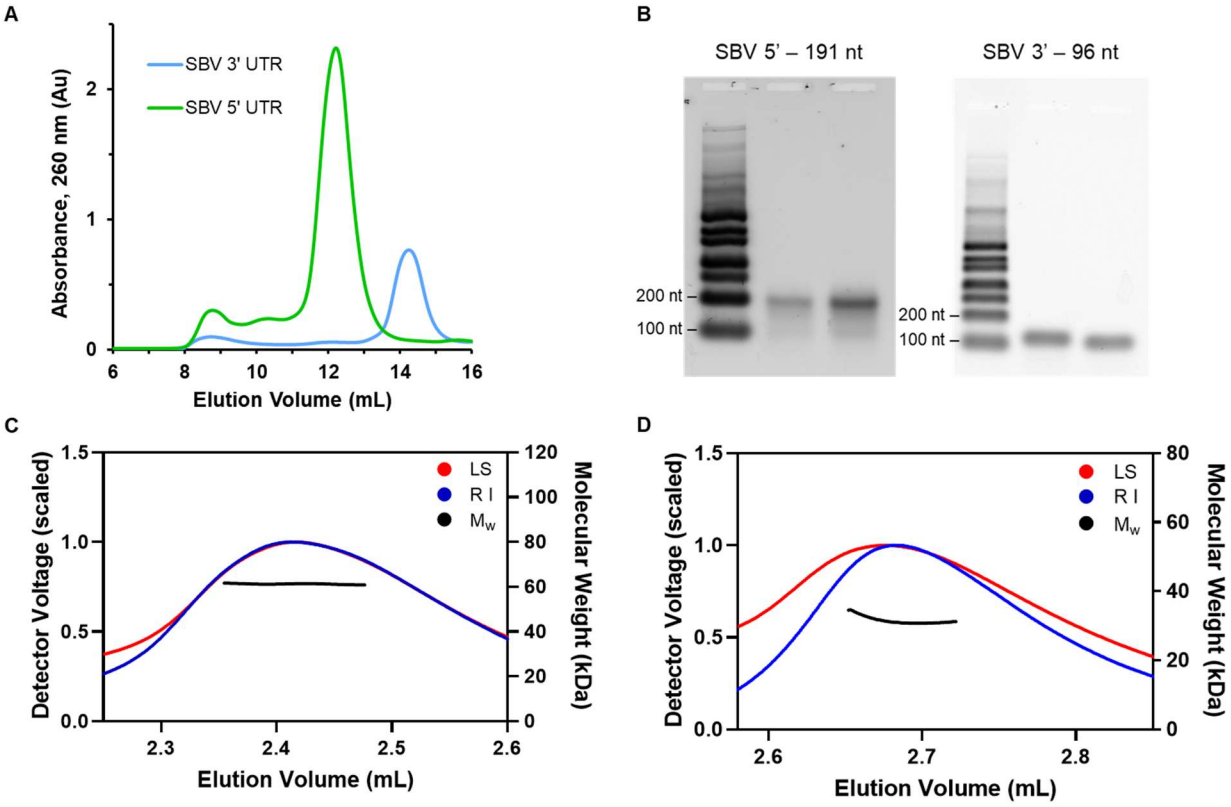

Figure 2.1. Purification and absolute molecular weight (Mw) determination of the SBV 5′ and 3′ UTRs. (**A**) Size exclusion chromatography elution profile of the SBV 5′ and 3′ UTRs purified using the Superdex 200 Increase 10/300 GL column (Cytiva Life Sciences, USA). The SBV 5′ UTR peak (green) elution fractions were collected from 11.5 to 13 mL, whereas the SBV 3′ UTR peak (blue) elution fractions were collected from ~13.5 to 15 mL. (**B**) Non-denaturing agarose gel (2%) showing concentrated SBV 5′ UTR (191 nucleotides (nt)) and 3′ UTR (96 nt) fractions. (**C**) SBV 5′ UTR absolute M_W determination of 61.26 ± 0.27 kDa (black line). (**D**) SBV 3′ UTR absolute M_W determination of 31.16 ± 0.54 kDa. Each multi-angle light scattering trace portrays light scattering (LS, red line) and the refractive index (RI, blue line).

2.5.2 SAXS analysis reveals a distinct SBV 5′ UTR and an elongated SBV 3′ UTR

To determine the 3-D structure of the SBV UTRs in solution, we utilized SAXS, a powerful technique that can provide low-resolution structure information based on the intensity of scattered high-energy photons (39). The raw scattering data for each RNA was merged (**Figure 2.2A**). Guinier analysis was performed on each data set, and the radius of gyration (R_g) was determined (**Figure 2.2B**). The Guinier R_g for SBV 5′ and 3′ UTRs were 49.28 ± 0.12 Å and

35.54 ± 0.30 Å, respectively (**Table 2.1**). A linear Guinier plot indicated that the samples were monodispersed and free of aggregation (27). The data were transformed into a dimensionless Kratky plot to assess the overall folding state of our RNAs (**Figure 2.2C**) (40). As the Kratky plot plateaus, this indicated that both RNAs are folded molecules and suggested an elongated profile, as seen in other RNAs of previous works (22,41). Lastly, the data were evaluated using real space electron density in a distance pair distribution plot (P(r)) (**Figure 2.2D**). This analysis determined the overall shape and the maximum dimension (D_{max}) of the RNA (42). We also determined values of real space R_g for SBV 5′ and 3′ UTRs to be 49.38 ± 0.58 Å and 35.56 ± 0.92 Å, respectively (**Table 2.1**). The similarity between Guinier R_g and P(r) R_g values gave confidence in the validity of the data sets. The D_{max} values of SBV 5′ and 3′ UTRs were calculated to be 151 Å and 108 Å, respectively (**Table 2.1**). These D_{max} values were expected in RNAs of differing lengths, with the SBV 5′ UTR being larger than the SBV 3′ UTR. We also determined the overall shape of the RNA molecules by examining the P(r) analysis. A solid sphere adopted a bell-shaped P(r) function, whereas an elongated molecule had a non-Gaussian distribution (42), similar to what is seen in **Figure 2.2D**. The P(r) distribution for the SBV 3′ UTR had an initial increase to its maxima and then a gradual decrease until the D_{max} was reached. The SBV 5′ UTR P(r) distribution revealed an elongated molecule; however, it had two slight peaks and then a gradual decrease. This result indicated that a different shape is formed, as further indicated by the SAXS envelope (**Figure 2.3**).

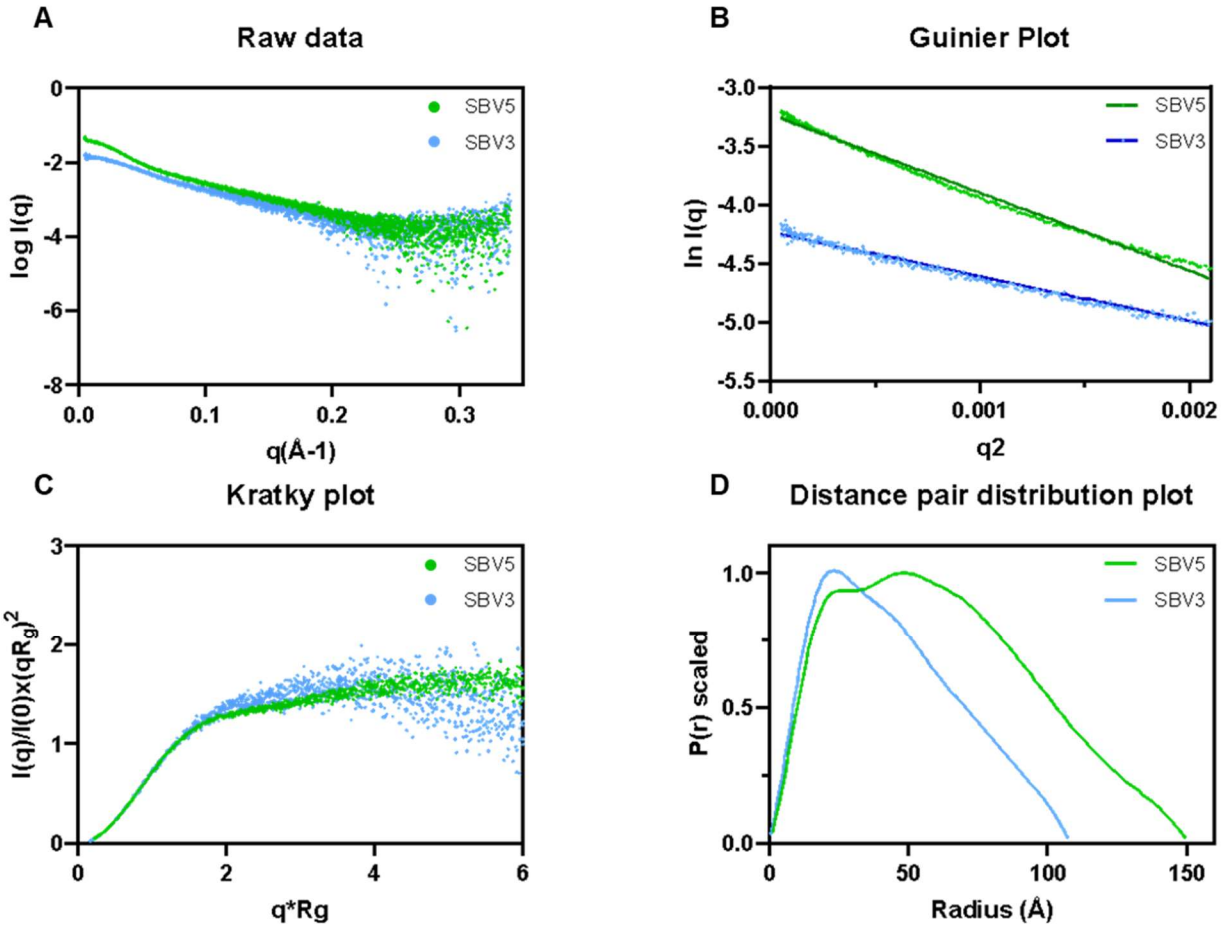

Figure 2.2. Small-angle X-ray scattering (SAXS) characterization of the SBV 5′ (green) and SBV 3′ (blue) UTRs. (**A**) Scattering data for SBV RNA depicting the scattering intensity (log I(q)) versus scattering angle ($q = 4\pi\sin\theta/\lambda$). (**B**) Guinier plots ($\ln(I(q))$ versus q^2), where a linear plot shows homogeneity of samples. (**C**) Dimensionless Kratky plots $(I(q)/I(0)*(q*R_g)^2$ versus $q*R_g$) demonstrating the elongated structure of the RNAs. (**D**) Distance pair distribution plots (P(r)) allow for the calculation of D_{max} and real-space R_g determination.

Table 2.1. Biophysical properties of the SBV 5′ and SBV 3′ UTRs determined from small-angle X-ray scattering (SAXS) analysis.

Parameters	SBV 5′ UTR	SBV 3′ UTR
SAXS Molecular Weight (kDa)	79.20	41.03
Guinier I(0)	0.0410	0.0146
Guinier R_g (Å)	49.28 ± 0.12	35.54 ± 0.30
P(r) I(0)	$0.0412 \pm 0.51 \times 10^{-4}$	$0.0146 \pm 0.35 \times 10^{-4}$
P(r) R_g (Å)	49.38 ± 0.58	35.56 ± 0.92
D_{max} (Å)	150.8	108.3
X^2 *	~ 1.03	~ 1.03
NSD *	0.98 ± 0.03	0.79 ± 0.02

Data points * were derived from DAMMIN and DAMAVER analysis. Terms: Scattering intensity at zero angle (I(0)); radius of gyration (R_g); maximum dimension (Dmax); goodness-of-fit parameter (X^2); and normalised spatial discrepancy (NSD)

DAMMIN (30) was used for *ab initio* modelling to generate low-resolution envelope structures for the SBV 5′ and 3′ UTRs. Fifty models were generated for the SBV 5′ UTR and twenty for the 3′ UTR, yielding favourable X^2 values of ~1.03, indicating that the experimental scattering data fits well with the computationally derived envelopes. These models were averaged and filtered to obtain a single representative model for each RNA using DAMAVER and DAMFILT (31), as shown in **Figure 2.3**. Both RNAs had low NSD values below 1 (**Table 2.1**), which suggested that the average model is very similar to all generated models (43). The envelope models (**Figure 2.3**) indicated that these RNA had elongated structures in solution, as the P(r) predicted. The SBV 3′ UTR (blue) adopted a typical extended RNA structure, as seen with other UTRs of similar size (44). The longer SBV 5′ UTR (green), while elongated, had a more distinctive structure. The envelope was asymmetrical, where the right side adopted a Y-shaped form while the left extended outward. The Y-shape appeared relatively wide, with a flattened structure when rotated along the X-axis, suggesting a more extended conformation.

While we successfully generated the envelope models for the UTRs, further investigation was required to obtain information on the directionality of the RNAs.

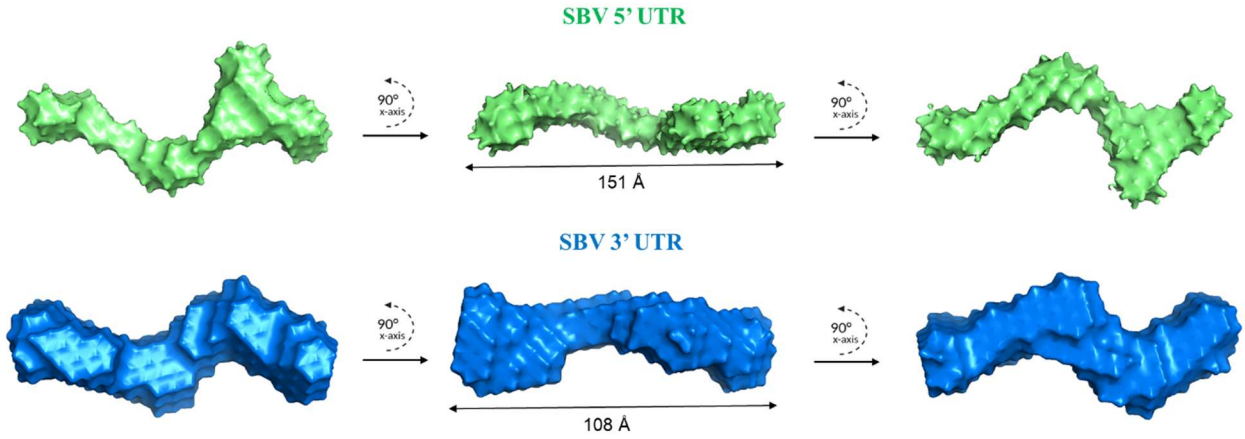

Figure 2.3. Small-angle X-ray scattering (SAXS) *ab initio* envelope models of the SBV 5′ (green) and 3′ (blue) UTRs. Depicted is the averaged and filtered low-resolution model for each RNA. SBV 5′ UTR takes on an elongated and asymmetrical structure with a Y-shaped form on the right, with a maximum dimension (D_{max}) of 151 Å. SBV 3′ UTR is also elongated, with a D_{max} of 108 Å. Each model is rotated along the X-axis at 90°. Dimensions represent D_{max} from P(r) plots.

To obtain structural insights into SBV UTRs, we combined in-solution experimental data with computationally derived atomistic structures. The RNAfold WebServer (32,33) was used to generate minimum free energy secondary structures for the SBV 5′ and 3′ UTRs (**Figure 2.4**). The SBV 5′ UTR had a single stem-loop (SL) followed by a large multibranched SL domain with five SLs (**Figure 2.4A**). The SBV 3′ UTR had a simple structure with a three-way junction, where three SL segments converge from a central branching point (**Figure 2.4B**). The secondary constraints were then inputted into SimRNA (34) for tertiary structure prediction. The predicted tertiary structures were superimposed with our experimental scattering data using DAMSUP (31). Selected alignments of our low-resolution SAXS envelopes to their predicted structures are shown in **Figures 2.5** and **2.6**. Alignments were chosen based on visual fit, low NSD values, and

R_g values similar to SAXS R_gs. The SBV 5′ UTR resulted in two top models with NSD values ranging from 1.20-1.22, meaning that the models had conformational heterogeneity, as shown in molecules from other studies (45,46). The SBV 3′ UTR yielded three top models with low NSD values from 0.94-0.97, indicating that all the computational models were very similar. Furthermore, the calculated R_g from the model fittings were correlated with the experimentally derived R_g (**Table 2.1**), where the SBV 5′ UTR models averaged 50.54 Å and the SBV 3′ UTR models at 35.49 Å. Overall, these structural overlays indicated that the SAXS data agree with the high-resolution computationally derived models.

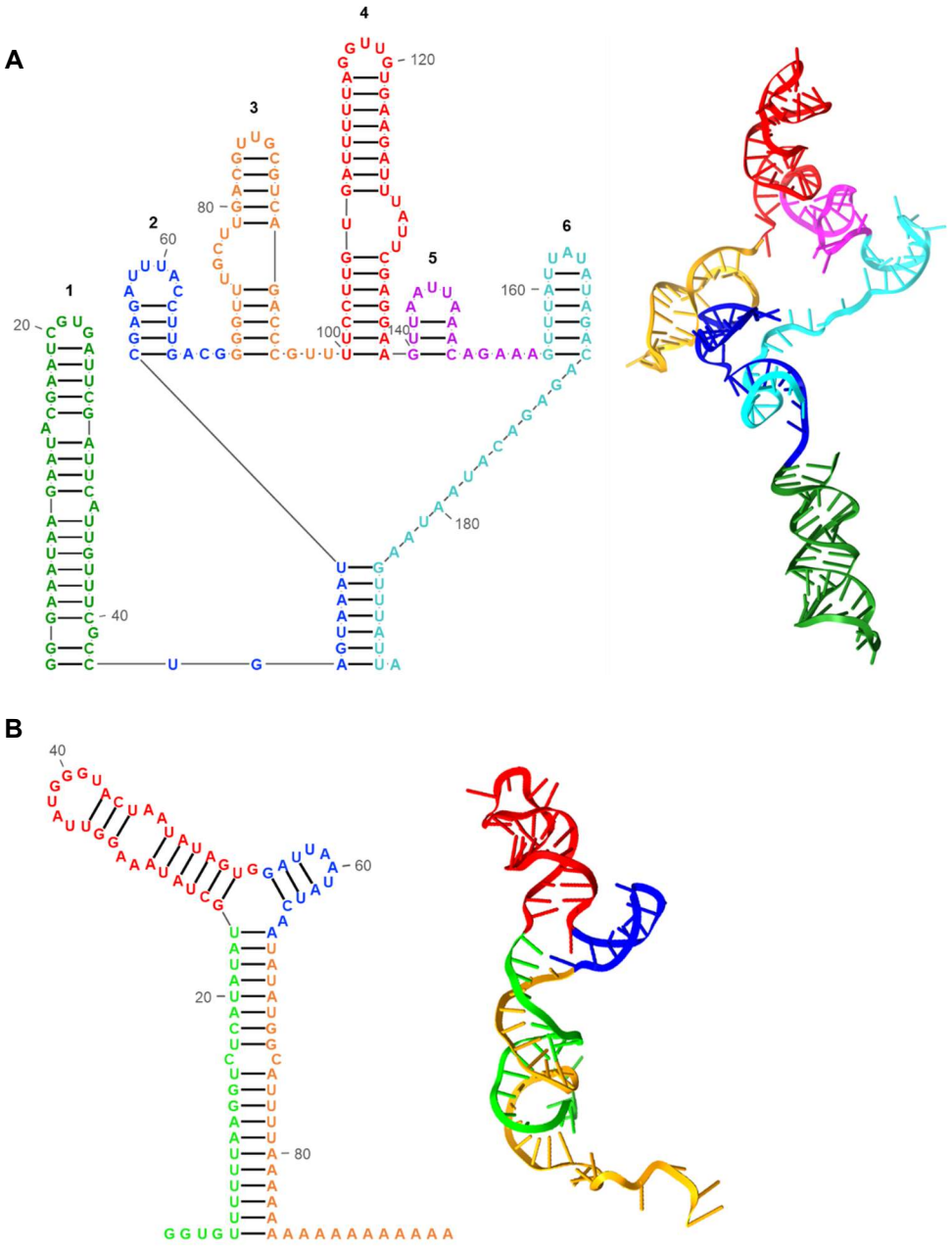

Figure 2.4. Visualization of the SBV UTR secondary structures and resulting computationally derived tertiary models. (**A**) SBV 5′ UTR 2-D secondary structure, with stem-loops numbered 1-6 and corresponding 3-D tertiary structure (AA_0411). (**B**) SBV 3′ UTR 2-D secondary structure and corresponding 3-D tertiary structure (AA_02_000086). Secondary structures were generated from the RNAfold WebServer (32,33). Tertiary structures were predicted using SimRNA (34). Structures are colour-coordinated with SLs. Visualized using RNAcanvas (47) and ChimeraX-1.8 (36).

The tertiary SBV 5′ UTR models showed a dynamic and flexible structure; however, some structural elements were maintained throughout each model (**Figure 2.5**). A consistently extended SL1 (**Figure 2.4**) was observed on the 5′ end of the RNA that mostly agrees with the SAXS envelope. The most distal end of the SL was slightly extending out of the envelope. On the 3′ end, a multi-branched SL structure that follows the Y-shaped envelope was observed. However, SL3 (**Figure 2.4**), near the middle, partially protruded from the envelope. Alongside this, SL4 also bulged out of the envelope. While we have not reported pseudoknots in our structure, these SL sections may fold more tightly in solution than the computational models visualize. The SBV 3′ UTR SAXS model agreed well with the predicted models, with only slight variations between each structure (**Figure 2.6**). The poly-adenylated tail was observed throughout each model, extending outward of the SAXS envelope. Also, a SL was present near the 3′ end of the molecule that slightly protrudes out of the envelope. In summary, we successfully visualized the 3-D structures of the SBV UTRs in solution and provided high-resolution models that helped to understand the SBV structural features.

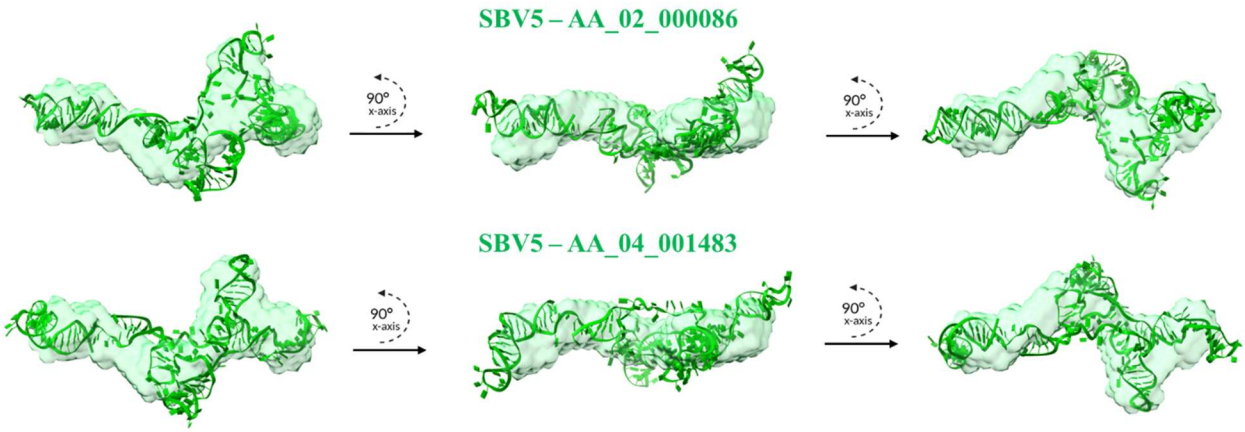

Figure 2.5. Model fitting of the SBV 5′ UTR SAXS envelope with their atomistic tertiary models. High-resolution models were generated using SimRNA (34) and overlayed using DAMSUP (31). Models AA_02_000086 and AA_04_001483 were chosen based on visual fit, X^2 values, and NSD values. Each model has an agreeable fit, showing the overlap of the atomistic model with the envelope. However, the stem-loop (SL) on the 5′ end protrudes out, and part of the multibranched SL structure extends out. Models are rotated along the X-axis at 90°. Visualized using ChimeraX-1.8 (36).

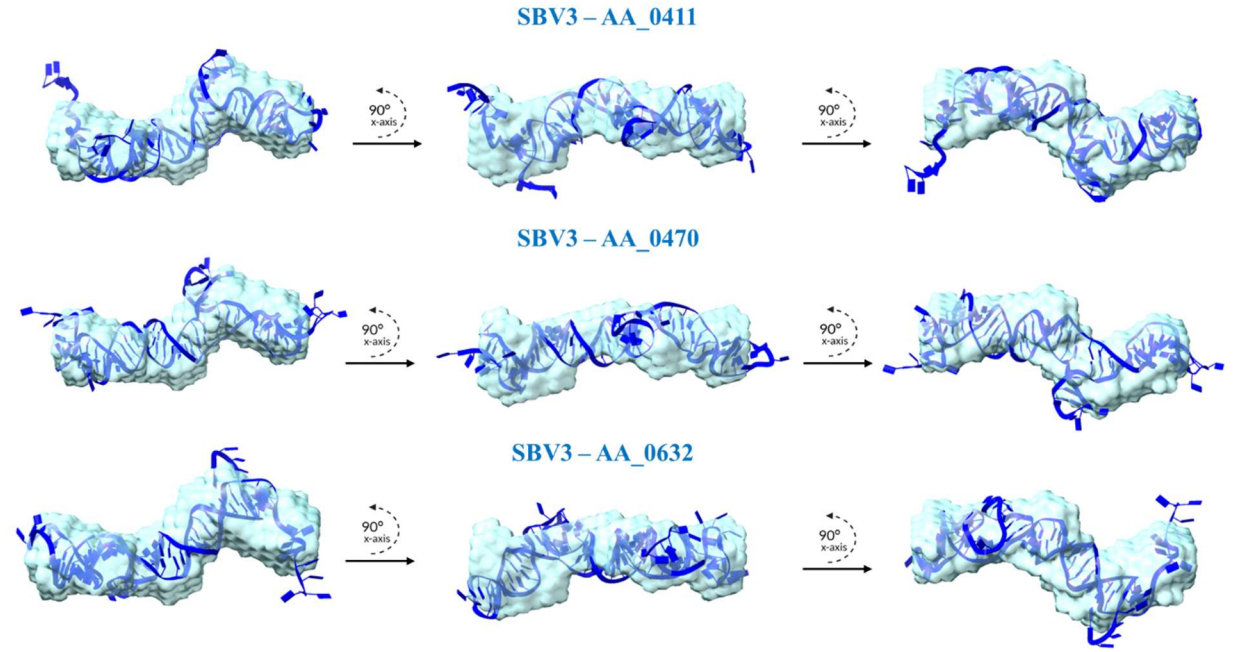

Figure 2.6. Model fitting of the SBV 3′ UTR SAXS envelope with their atomistic tertiary models. High-resolution models were generated using SimRNA (34) and overlayed using DAMSUP (31). Models AA_0411, AA_0470, and AA_0632 were chosen based on visual fit, X^2 values, and NSD values. Each atomistic model fits well with the SAXS envelope. However, there is a stem-loop that protrudes from the envelope near the 3′ end, and the poly-adenylated tail that extends outward. Models are rotated along the X-axis at 90°. Visualized using ChimeraX-1.8 (36).

2.5.3 Full-length SBV 5′ UTR and a critical 39 nt region have IRES activity *in vitro*

Previous studies have speculated that the SBV 5′ UTR possesses an IRES based on its classification as an Iflavirus (11,14). However, this hypothesis has not been tested. To determine whether the SBV 5′ UTR has internal translation activity, a bicistronic reporter RNA was generated and tested in insect Sf21 lysates. The SBV 5′ UTR was inserted between *Renilla* (RLuc) and firefly (FLuc) luciferase cistrons. Translation of RLuc relies on scanning-dependent mechanisms, whereas translation of the downstream FLuc cistron relies on cap-independent mechanisms such as an IRES (48). Therefore, the translational activity of the SBV 5′ UTR can be measured through FLuc activity, while RLuc acts as a control. The raw data (**Figure S2.2**) is normalized to a ratio of FLuc/RLuc, as indicated in **Figure 2.7A**. The wildtype (WT) SBV 5′ UTR displayed similar relative luciferase activity as compared to WT CrPV IRES (**Figure 2.7A**). The CrPV IGR IRES is well studied and used as a benchmark for studying IRES activity (21). The reactions contained exogenous Mg^{+2} and K^{+}, as the addition of these salts assisted in CrPV IRES structure and function (49). In the presence of exogenous salt, translation by the SBV 5′ UTR was approximately 97% of WT CrPV, whereas, in the absence of salt, translation was ~83%. As expected, mutant CrPV IRES (mPKI), which contains mutations that disrupt pseudoknot base pairing (21), did not support internal initiation. These results demonstrated that the SBV 5′ UTR initiates translation via an IRES *in vitro*.

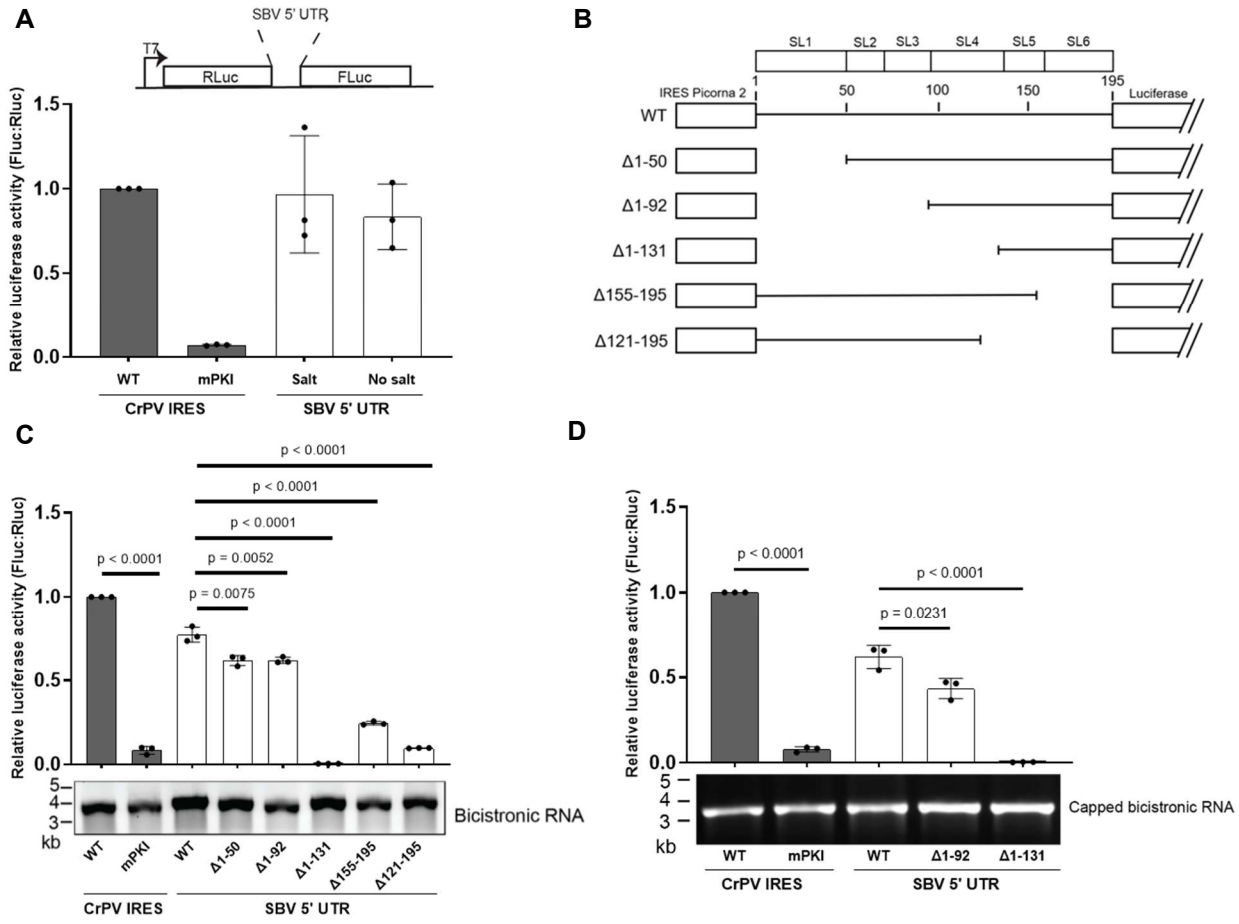

Figure 2.7. Determination of IRES activity of the SBV 5′ UTR. (**A**) Bicistronic reporter assay performed *in vitro* with Sf21 lysates to determine relative luciferase activity of full length SBV 5′ UTR with or without salt. Above the graph is a depiction of the bicistronic reporter construct where SBV 5′ UTR is inserted between RLuc and FLuc. (**B**) Deletion mutants generated from the 5′ and 3′ end of the SBV 5′ UTR. Shown above are the stem-loops (SLs) that become deleted based on each mutant; Δ = deletion. (**C**) Bicistronic reporter assay repeated with the deletion mutants. (**D**) Relative luciferase activity determined of bicistronic RNAs transfected into S2 cells. All samples were measured for RLuc and FLuc activity and normalized to wildtype (WT) CrPV IRES. An unpaired t-test was used to determine p values; $p < 0.05$ is significant. Values shown are the averages (± standard deviation) from n=3.

The SBV IRES activity is within the 195 nt 5′ UTR. To delineate further the minimal SBV IRES element, deletion mutants of the SBV 5′ UTR were created (**Figure 2.7B**). The regions selected for deletion were chosen based on the predicted secondary structure, resulting in the systematic deletion of the predicted SL structures from either the 5′ end or the 3′ end of the

SBV 5′ UTR (**Figure 2.4**). Briefly, for the 5′ end deletions: Δ1-50, Δ1-92, and Δ1-131 deleted SL1, SL1-3 and SL1-4, respectively. The 3′ end deletions included Δ155-195 and Δ121-195, which resulted in the deletion of SL6 and SL4-6, respectively. Bicistronic reporter RNAs were incubated in Sf21 extracts, and luciferase activities were measured. Deleting SL1-4 (Δ1-131) abolished all relative luciferase activity as compared to the full-length WT SBV 5′ UTR, indicating that IRES activity was impaired (**Figure 2.7C**). However, deleting SL1 or SL1-3 (Δ1-50, Δ1-92) retained IRES activity (~80% of WT SBV 5′UTR). By contrast, 3′ deletions of SL6 (Δ155-195) and SL4-6 (Δ121-195), diminished IRES translation, showing ~32% and ~13%, respectively, of WT SBV 5′ UTR activity. These results indicated that the region between 92-131 nt, which contains SL1-4, is critical for IRES activity (**Figure 2.8**). While the deletion of SL1-4 resulted in the total loss of activity, the deletion of SL4-6 (Δ121-195) also resulted in lower IRES activity. It is likely that this region, containing SL5 and SL6, contributed towards efficient IRES activity. These results indicate that a region within SL4 is crucial for IRES activity. In summary, deletion mutants have delineated a 39 nt section between 92 -131 nt of the SBV 5′ UTR (herein dubbed the minimal SBV IRES) critical for IRES activity *in vitro*.

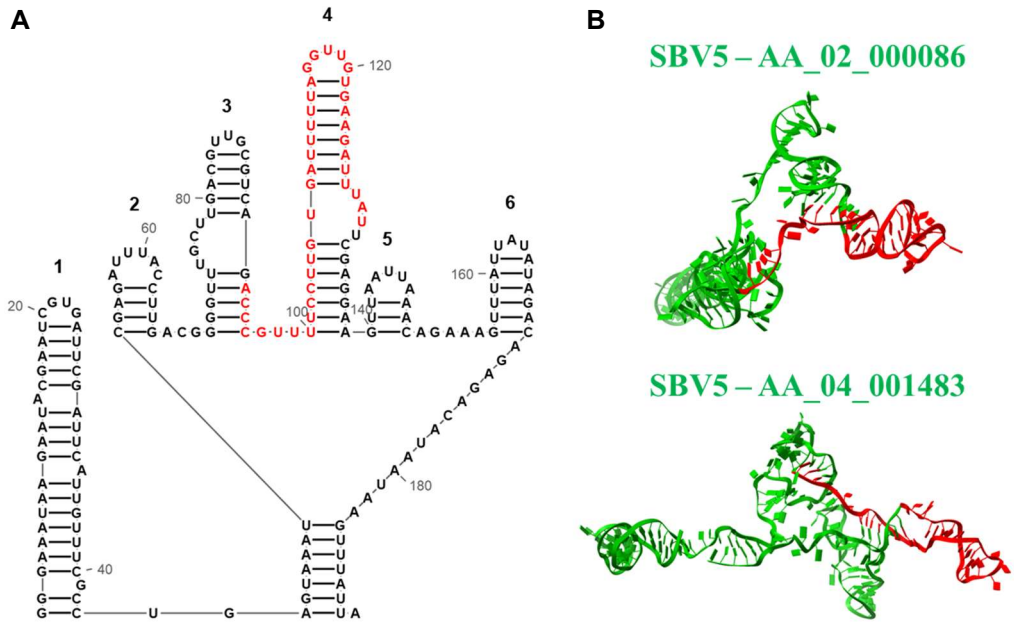

Figure 2.8. Visualizing the minimal region required for IRES activity. (**A**) SBV 5′ UTR 2-D secondary structure schematic. Red indicates the region where the segment needed for any IRES activity is between 92-131 nt (based on the deletion mutant Δ1-131). Stem-loops (SLs) are numbered from 1-6. Visualized using RNAcanvas (47). (**B**) Tertiary structure of SBV 5′ UTR illustrating 92-131 nt (SL4) in red. Visualized using ChimeraX-1.8 (36).

2.5.4 SBV 5′ UTR has IRES activity in S2 cells

We also investigated whether WT SBV 5′ UTR and the minimal SBV IRES can support translation in *D. melanogaster* S2 cells. S2 cells were transfected with *in vitro* transcribed bicistronic RNAs containing the WT SBV 5′ UTR or mutants that delete SL1-3 or SL1-4 (Δ1-92 or Δ1-131). The results were consistent with *in vitro* data, where Δ1-92 RNAs showed ~70% of WT SBV 5′ UTR relative luciferase activity and deleting SL1-4 (Δ1-131) abolished activity (**Figure 2.7D**). When comparing WT SBV 5′ UTR and WT CrPV IRES translation in transfected S2 cells, SBV 5′ UTR-mediated translation was lower, ~62% of WT CrPV IRES. These results further confirmed that the full-length SBV 5′ UTR contains an IRES and that the 92-131 nt element is critical for IRES translation both *in vitro* and in transfected Drosophila S2 cells.

Given that the SBV 5′UTR can direct IRES-mediated translation in Sf21 extract and *Drosophila* cells, these results suggest that the mechanism underlying SBV 5′ UTR IRES translation may be conserved across species, including in honey bees. It will be important to test SBV 5′ UTR IRES translation in a honey bee cell line, once a consistent honey bee cell line has been established. Maintaining an *A. mellifera* cell line is difficult, and it is hard to find honey bee cells without viruses (50). In replacement of the honey bee cell line, insect cell lines, such as those from other hymenopteran species, can be used. Furthermore, to elucidate the exact mechanism of IRES-mediated translation initiation, studies will need to be performed to determine if IRES trans-acting factors (ITAFs) and/or eukaryotic initiation factors (eIFs) are required for function (19). Overall, these findings show that the SBV 5′ UTR contains a functional IRES capable of cap-independent translation *in vivo*. These results imply that SBV can maintain viral protein synthesis even during host stress conditions where cap-dependent translation is inhibited, an important step towards understanding the SBV life cycle.

2.5.5 SBV IRES structural elements

A handful of studies show the structure of IRES elements in solution (38,51-56). Most of the three-dimensional structure information on IRESs comes from cryogenic electron microscopy and X-ray crystallography studies in which an IRES is bound with a ribosome (53,57). We are able to present, for the first time, models for the 3-D solution structure of an IRES element from the *Iflaviridae* family. The SBV 5′ UTR has a distinct shape, creating a multi-branched SL element at the 3′ end of the RNA, while the 5′ end extends outward as a single SL (**Figures 2.4** and **2.5**). The model fitting shows that this unique shape is flexible, a common trait of the closely related picornavirus IRESs (58). Viral IRESs are diverse in their structural elements, and no universal structural motif exists for all IRESs (18).

When comparing our secondary structure to known Iflavirus IRESs, we can see no strong resemblance to these structures (14-16). The Iflavirus IRESs studied are longer than the SBV 5′ UTR and have 52-61% sequence similarity in the 5′ UTR region. The VDV-1 5′ UTR is 1117 nt long and contains five hairpins and two branched cloverleaf-like structures (14), which do not resemble the SBV 5′ UTR multibranched structural element. Similarly, the 5′ region of IFV contains multiple SLs, a cloverleaf structure, and a three-way junction (17) that do not resemble the SBV 5′ UTR. The 5′ UTRs of PnV and EoPV have similar structures with multiple SLs (14,16), however, they are not similar to the SBV 5′ UTR structure. These differences are not unusual, as shown in *Picornaviridae*, IRES structure can vary greatly within the family (19).

Picornavirus IRESs, which are closely related to the picorna-like Iflaviruses, have been studied extensively. There are six distinct types of picornavirus and picorna-like IRESs, which are classified based on structure and requirements of cellular factors: the enterovirus group (Type I) (18), the aphtho-/cardiovirus group (Type II) (59), the hepatitis A virus group (Type III) (60), the hepatitis C virus-like group (Type IV) (61), the aichivirus-like group (Type V) (62), and the newly classified dicistrovirus group (Type VI) (20). There is no significant resemblance when comparing the SBV 5′ UTR to these IRES types. The SBV 5′ UTR is small compared to most picornavirus IRESs, and the multibranched SL region appears unique. Like the other Iflavirus IRESs, cloverleaf structures are common in the picornavirus IRESs, a domain the SBV 5′ UTR does not have. Type II IRESs are described as having a Y-shaped domain (63). Even though our secondary structure does not resemble the Type II IRESs, the folding pattern of certain domains appears similar. The Y-shape of our multibranched domain slightly resembles the J-K domain of the Type II IRES from encephalomyocarditis virus (EMCV) (56). While they have a similar shape, the structure of our domain has more SLs than the J-K region. Type IV IRESs are smaller

than other picornavirus IRESs, and some viruses within this type are similar in size to the SBV 5′ UTR (64). The structural features of Type IV IRESs include a single SL (domain II) followed by domain III composed of several subdomains and an essential pseudoknot (65). The SBV 5′ UTR SL1 is similar to the Type IV IRES domain II; however, the multibranched domain differs from domain III (61). There is also a resemblance of the SBV IRES to the CrPV IGR IRES in 3-D shape (66), however, we have reported no known pseudoknots in our structure. Further investigation is required to determine the presence or absence of pseudoknots. Overall, more evidence is needed to elucidate the type of IRES that the SBV 5′ UTR resembles.

There are common motifs seen in picornavirus IRESs that can contribute to activity and efficiency. Two purine-rich motifs, the RAAA and GNRA motifs, are commonly found at the end of SLs and have been shown to contribute to IRES activity (67). Two GAAA sequences are present in the SBV 5′ UTR; one is found in SL1 and in a single-stranded region between SL5 and SL6 (**Figure 2.4**). Considering these sequences are not situated at the distal ends of SLs, their contribution to IRES activity is unlikely. There are GNRA sequences found throughout, however, these sequences do not form tetraloops in our predicted secondary structure. Another possible motif is the 8 nt long polypyrimidine tract region (5′-UUUUCCUU-3′) from 98-105 nt in SL4. The mutation of the UUUCCUU motif in the foot-and-mouth disease virus (FMDV) IRES abolishes IRES activity (68). This motif acts as a binding site for polypyrimidine tract-binding protein (PTB), which helps facilitate translation initiation at the FMDV IRES (69). This, taken together with SL4's pyrimidine-rich background and bulge region, may be evidence for this region's contribution to IRES activity. Further mutational analyses will need to be performed to determine the contribution of these regions to SBV IRES activity.

2.6 Conclusion

In conclusion, we have biophysically characterized the UTRs of SBV and demonstrated that the SBV 5′ UTR possesses IRES activity both *in vitro* and *in vivo*, bringing us one step closer to understanding the SBV life cycle. The combination of bicistronic assays and the solution structure of the SBV 5′ UTR provides strong evidence supporting its role as an IRES. Through deletion mutants, we mapped the region necessary for IRES activity to a structured segment between 92- 131 nt, with the 3′ end (121-195 nt) further contributing to efficient IRES function. Future mutation analyses are required to determine whether the 39 nt section is critical due to its structure or sequence. Additionally, Selective 2' Hydroxyl Acylation analyzed by Primer Extension (SHAPE) analysis should be conducted to accurately determine the RNA secondary structure of the SBV UTRs, including the potential presence of pseudoknots. Investigating whether host factors, such as translation initiation factors, are required for the SBV 5′ UTR to initiate translation is also a crucial next step. By experimentally confirming the secondary structure and identifying any necessary host factors, we can better classify the type of IRES. This study advances our understanding of *Iflaviridae* noncoding RNA structure and its role in the viral life cycle, providing valuable insights that could inform the future development of antiviral therapeutics.

2.7 Data Availability

SAXS data have been deposited to SASDBD server and can be accessed using the following accession numbers: SASDVX7 and SASDVW7 for the SBV 5′ UTR and SBV 3′ UTR, respectively.

2.8 Supplementary Data

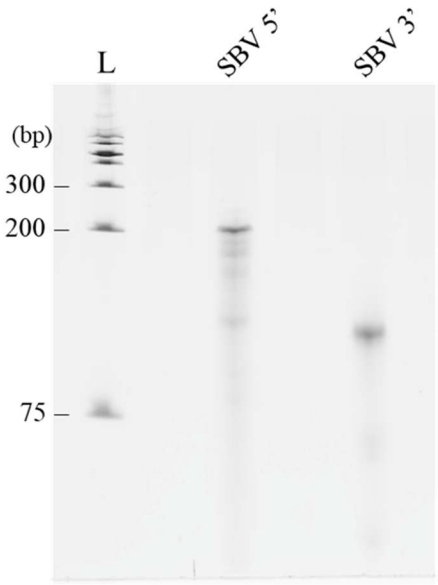

Figure S2.1. Urea-PAGE analysis of purified *in vitro* transcribed SBV UTRs. 8% urea-PAGE illustrating RNA purity after SEC purification, where the SBV 5′ UTR migrates around 191 nucleotides (nt) and the SBV 3′ UTR around 96 nt. Gel ran at 300V for 17 minutes. Loaded with 1 kb Plus DNA Ladder (Thermo Fisher Scientific, USA).

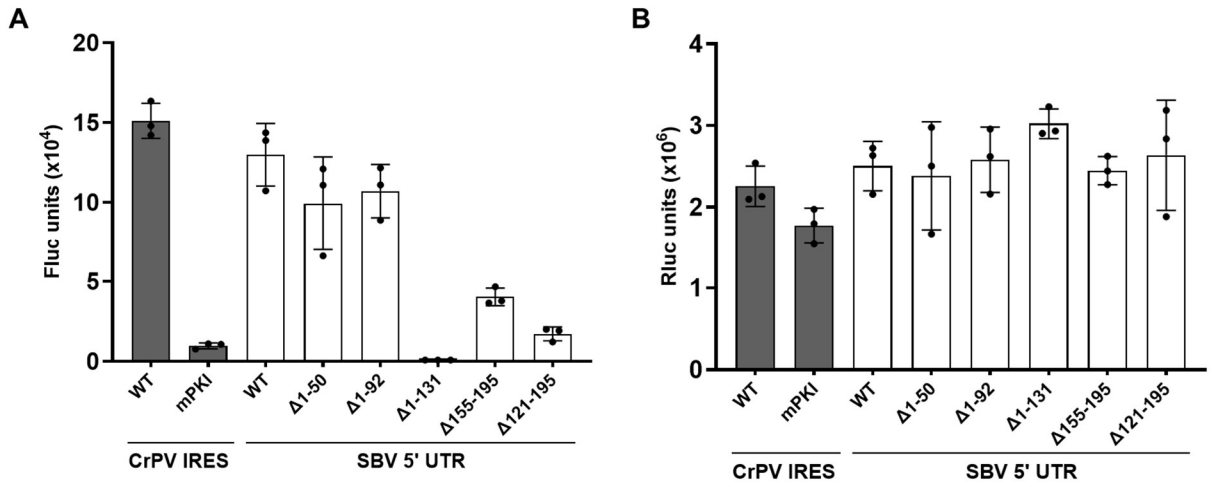

Figure S2.2. Raw luciferase values from the SBV 5′ UTR deletion mutant analysis. Firefly luciferase (FLuc) (**A**) and *Renilla* luciferase (RLuc) (**B**) activity of the CrPV IREs and the wildtype (WT) and deletion mutants of SBV 5′ UTR. Values shown are the averages (± standard deviation) from n=3.

2.9 References

1. Potts, S.G., Imperatriz-Fonseca, V., Ngo, H.T., Aizen, M.A., Biesmeijer, J.C., Breeze, T.D., Dicks, L.V., Garibaldi, L.A., Hill, R., Settele, J. *et al.* (2016) Safeguarding pollinators and their values to human well-being. *Nature*, **540**, 220-229.
2. Claing, G., Ellsworth, S., Ferland, J., Janser, M., Kempers, M., Kozak, P., Maund, C., Menzies, C., Micholson, D., Morfin, N. *et al.* (2023) Canadian Association of Professional Apiculturists (CAPA) statement on honey bee wintering losses in Canada for 2023; https://capabees.com/shared/CAPA-Statement-on-Colony-Losses-2022-2023_final.pdf
3. Cornman, R.S., Tarpy, D.R., Chen, Y., Jeffreys, L., Lopez, D., Pettis, J.S., vanEngelsdorp, D. and Evans, J.D. (2012) Pathogen webs in collapsing honey bee colonies. *PLoS One*, **7**, e43562.
4. Ellis, J.D. and Munn, P.A. (2015) The worldwide health status of honey bees. *Bee World*, **86**, 88-101.
5. National Bee Diagnostic Centre. (2017) Canadian National Honey Bee Health Survey, 2017 Report. 1-33.
6. Bailey, L., Gibbs, A.J. and Woods, R.D. (1964) Sacbrood virus of the larval honey bee (*Apis mellifera* Linnaeus). *Virology*, **23**, 425-429.
7. Ball, B.V. and Bailey, L. (1997) In Morse, R. A. and Flottum, K. (eds.), *Honey Bee Pests, Predators, & Disease*. The A. I. Root Company, Medina, OH, USA, pp. 11-31.
8. Wei, R., Cao, L., Feng, Y., Chen, Y., Chen, G. and Zheng, H. (2022) Sacbrood virus: a growing threat to honeybees and wild pollinators. *Viruses*, **14**, 1871.
9. Borba, R.S., Hoover, S.E., Currie, R.W., Giovenazzo, P., Guarna, M.M., Foster, L.J., Zayed, A. and Pernal, S.F. (2022) Phenomic analysis of the honey bee pathogen-web and its dynamics on colony productivity, health and social immunity behaviors. *PLoS One*, **17**, e0263273.
10. Baker, A.C. and Schroeder, D.C. (2008) The use of RNA-dependent RNA polymerase for the taxonomic assignment of Picorna-like viruses (order *Picornavirales*) infecting *Apis mellifera* L. populations. *Virol J*, **5**, 10.
11. Valles, S.M., Chen, Y., Firth, A.E., Guerin, D.M.A., Hashimoto, Y., Herrero, S., de Miranda, J.R., Ryabov, E. and ICTV Report Consortium. (2017) ICTV virus taxonomy profile: *Iflaviridae*. *J Gen Virol*, **98**, 527-528.
12. van Oers, M.M. (2010) In Asgari, S. and Johnson, K. N. (eds.), *Insect Virology*. Caister Academic Press, Norfolk, U.K., pp. 231-250.
13. Li, J., Wang, T., Evans, J.D., Rose, R., Zhao, Y., Li, Z., Li, J., Huang, S., Heerman, M., Rodriguez-Garcia, C. *et al.* (2019) The phylogeny and pathogenesis of Sacbrood virus (SBV) infection in European honey bees, *Apis mellifera*. *Viruses*, **11**.
14. Ongus, J.R., Roode, E.C., Pleij, C.W.A., Vlak, J.M. and van Oers, M.M. (2006) The 5′ non-translated region of *Varroa destructor* virus 1 (genus *Iflavirus*): structure prediction and IRES activity in *Lymantria dispar* cells. *J Gen Virol*, **87**, 3397-3407.
15. Lu, J., Hu, Y., Hu, L., Zong, S., Cai, D., Wang, J., Yu, H. and Zhang, J. (2007) *Ectropis obliqua* picorna-like virus IRES-driven internal initiation of translation in cell systems derived from different origins. *J Gen Virol*, **88**, 2834-2838.
16. Wu, T.Y., Wu, C.Y., Chen, Y.J., Chen, C.Y. and Wang, C.H. (2007) The 5′ untranslated region of *Perina nuda* virus (PnV) possesses a strong internal translation activity in baculovirus-infected insect cells. *FEBS Lett*, **581**, 3120-3126.

17. Li, M., Man, N., Qiu, H., Cai, S., He, X., He, X. and Lu, X. (2012) Detection of an internal translation activity in the 5′ region of *Bombyx mori* infectious flacherie virus. *Appl Microbiol Biotechnol*, **95**, 697-705.
18. Martinez-Salas, E., Francisco-Velilla, R., Fernandez-Chamorro, J. and Embarek, A.M. (2017) Insights into structural and mechanistic features of viral IRES elements. *Front Microbiol*, **8**, 2629.
19. Abdullah, S.W., Wu, J., Wang, X., Guo, H. and Sun, S. (2023) Advances and breakthroughs in IRES-directed translation and replication of picornaviruses. *mBio*, **14**.
20. Abaeva, I.S., Young, C., Warsaba, R., Khan, N., Tran, L.V., Jan, E., Pestova, T.V. and Hellen, C.U.T. (2023) The structure and mechanism of action of a distinct class of dicistrovirus intergenic region IRESs. *Nucleic Acids Res*, **51**, 9294-9313.
21. Jan, E. and Sarnow, P. (2002) Factorless ribosome assembly on the internal ribosome entry site of cricket paralysis virus. *J Mol Biol*, **324**, 889-902.
22. Mrozowich, T., Park, S.M., Waldl, M., Henrickson, A., Tersteeg, S., Nelson, C.R., De Klerk, A., Demeler, B., Hofacker, I.L., Wolfinger, M.T. *et al.* (2023) Investigating RNA-RNA interactions through computational and biophysical analysis. *Nucleic Acids Res*, **51**, 4588-4601.
23. Wyatt, P.J. (2014) Measurement of special nanoparticle structures by light scattering. *Anal Chem*, **86**, 7171-7183.
24. Cowieson, N.P., Edwards-Gayle, C.J.C., Inoue, K., Khunti, N.S., Doutch, J., Williams, E., Daniels, S., Preece, G., Krumpa, N.A., Sutter, J.P. *et al.* (2020) Beamline B21: high-throughput small-angle X-ray scattering at Diamond Light Source. *J Synchrotron Radiat*, **27**, 1438-1446.
25. Manalastas-Cantos, K., Konarev, P.V., Hajizadeh, N.R., Kikhney, A.G., Petoukhov, M.V., Molodenskiy, D.S., Panjkovich, A., Mertens, H.D.T., Gruzinov, A., Borges, C. *et al.* (2021) ATSAS 3.0: expanded functionality and new tools for small-angle scattering data analysis. *J Appl Crystallogr*, **54**, 343-355.
26. Panjkovich, A. and Svergun, D.I. (2018) CHROMIXS: automatic and interactive analysis of chromatography-coupled small-angle X-ray scattering data. *Bioinformatics*, **34**, 1944-1946.
27. Putnam, C.D. (2016) Guinier peak analysis for visual and automated inspection of small-angle X-ray scattering data. *J Appl Crystallogr*, **49**, 1412-1419.
28. Burke, J.E. and Butcher, S.E. (2012) Nucleic acid structure characterization by small angle X-ray scattering (SAXS). *Curr Protoc Nucleic Acid Chem*, **Chapter 7**, Unit7 18.
29. Svergun, D.I. (1992) Determination of the regularization parameter in indirect-transform methods using perceptual criteria. *J. Appl. Cryst.*, **25**, 495-503.
30. Svergun, D.I. (1999) Restoring low resolution structure of bio macromolecules from solution scattering using simulated annealing. *Biophysical Journal*, **76**, 2879-2886.
31. Volkov, V.V. and Svergun, D.I. (2003) Uniqueness of *ab initio* shape determination in small-angle scattering. *Journal of Applied Crystallography*, **36**, 860-864.
32. Gruber, A.R., Lorenz, R., Bernhart, S.H., Neubock, R. and Hofacker, I.L. (2008) The Vienna RNA websuite. *Nucleic Acids Res*, **36**, W70-74.
33. Lorenz, R., Bernhart, S.H., Höner zu Siederdissen, C., Tafer, H., Flamm, C., Stadler, P.F. and Hofacker, I.L. (2011) ViennaRNA package 2.0. *Algorithms for Molecular Biology*, **6**.

34. Boniecki, M.J., Lach, G., Dawson, W.K., Tomala, K., Lukasz, P., Soltysinski, T., Rother, K.M. and Bujnicki, J.M. (2016) SimRNA: a coarse-grained method for RNA folding simulations and 3D structure prediction. *Nucleic Acids Res*, **44**, e63.
35. Franke, D., Petoukhov, M.V., Konarev, P.V., Panjkovich, A., Tuukkanen, A., Mertens, H.D.T., Kikhney, A.G., Hajizadeh, N.R., Franklin, J.M., Jeffries, C.M. *et al.* (2017) ATSAS 2.8: a comprehensive data analysis suite for small-angle scattering from macromolecular solutions. *J Appl Crystallogr*, **50**, 1212-1225.
36. Meng, E.C., Goddard, T.D., Pettersen, E.F., Couch, G.S., Pearson, Z.J., Morris, J.H. and Ferrin, T.E. (2023) UCSF ChimeraX: tools for structure building and analysis. *Protein Sci*, **32**, e4792.
37. Wang, Q.S., Au, H.H. and Jan, E. (2013) Methods for studying IRES-mediated translation of positive-strand RNA viruses. *Methods*, **59**, 167-179.
38. Chen, Y., Chapagain, S., Chien, J., Pereira, H.S., Patel, T.R., Inoue-Nagata, A.K. and Jan, E. (2024) Factor-dependent internal ribosome entry site and -1 programmed frameshifting signal in the bemisia-associated dicistrovirus 2. *Viruses*, **16**, 695.
39. Grawert, T.W. and Svergun, D.I. (2020) Structural modeling using solution small-angle X-ray scattering (SAXS). *J Mol Biol*, **432**, 3078-3092.
40. Patel, T.R., Chojnowski, G., Astha, Koul, A., McKenna, S.A. and Bujnicki, J.M. (2017) Structural studies of RNA-protein complexes: A hybrid approach involving hydrodynamics, scattering, and computational methods. *Methods*, **118-119**, 146-162.
41. D'Souza, M.H., Mrozowich, T., Badmalia, M.D., Geeraert, M., Frederickson, A., Henrickson, A., Demeler, B., Wolfinger, M.T. and Patel, T.R. (2022) Biophysical characterisation of human LincRNA-p21 sense and antisense Alu inverted repeats. *Nucleic Acids Res*, **50**, 5881-5898.
42. Kikhney, A.G. and Svergun, D.I. (2015) A practical guide to small angle X-ray scattering (SAXS) of flexible and intrinsically disordered proteins. *FEBS Lett*, **589**, 2570-2577.
43. Kozin, M.B. and Svergun, D.I. (2001) Automated matching of high- and low-resolution structural models. *J Appl Cryst*, **34**, 33-41.
44. Mrozowich, T., Henrickson, A., Demeler, B. and Patel, T.R. (2020) Nanoscale structure determination of Murray Valley encephalitis and Powassan virus non-coding RNAs. *Viruses*, **12**, 190.
45. Zhang, Y., Zhang, Y., Liu, Z.Y., Cheng, M.L., Ma, J., Wang, Y., Qin, C.F. and Fang, X. (2019) Long non-coding subgenomic flavivirus RNAs have extended 3D structures and are flexible in solution. *EMBO Rep*, **20**, e47016.
46. Konarev, P.V., Petoukhov, M.V. and Svergun, D.I. (2016) Rapid automated superposition of shapes and macromolecular models using spherical harmonics. *J Appl Crystallogr*, **49**, 953-960.
47. Johnson, P.Z. and Simon, A.E. (2023) RNAcanvas: interactive drawing and exploration of nucleic acid structures. *Nucleic Acids Res*, **51**, W501-W508.
48. Jimenez, J., Jang, G.M., Semler, B.L. and Waterman, M.L. (2005) An internal ribosome entry site mediates translation of lymphoid enhancer factor-1. *RNA*, **11**, 1385-1399.
49. Wilson, J.E., Powell, M.J., Hoover, S.E. and Sarnow, P. (2000) Naturally occurring dicistronic cricket paralysis virus RNA is regulated by two internal ribosome entry sites. *Molecular and Cellular Biology*, **20**, 4990-4999.
50. Guo, Y., Goodman, C.L., Stanley, D.W. and Bonning, B.C. (2020) Cell lines for honey bee virus research. *Viruses*, **12**, 236.

51. Perard, J., Leyrat, C., Baudin, F., Drouet, E. and Jamin, M. (2013) Structure of the full-length HCV IRES in solution. *Nat Commun*, **4**, 1612.
52. Tolbert, M., Morgan, C.E., Pollum, M., Crespo-Hernandez, C.E., Li, M.L., Brewer, G. and Tolbert, B.S. (2017) HnRNP A1 alters the structure of a conserved enterovirus IRES domain to stimulate viral translation. *J Mol Biol*, **429**, 2841-2858.
53. Kieft, J.S., Zhou, K., Jubin, R., Murray, M.G., Lau, J.Y.N. and Doudna, J.A. (1999) The hepatitis C virus internal ribosome entry site adopts an ion-dependent tertiary fold. *J Mol Biol*, **292**, 513-529.
54. Beckham, S.A., Matak, M.Y., Belousoff, M.J., Venugopal, H., Shah, N., Vankadari, N., Elmlund, H., Nguyen, J.H.C., Semler, B.L., Wilce, M.C.J. *et al.* (2020) Structure of the PCBP2/stem-loop IV complex underlying translation initiation mediated by the poliovirus type I IRES. *Nucleic Acids Res*, **48**, 8006-8021.
55. Dorn, G., Gmeiner, C., de Vries, T., Dedic, E., Novakovic, M., Damberger, F.F., Maris, C., Finol, E., Sarnowski, C.P., Kohlbrecher, J. *et al.* (2023) Integrative solution structure of PTBP1-IRES complex reveals strong compaction and ordering with residual conformational flexibility. *Nat Commun*, **14**, 6429.
56. Imai, S., Kumar, P., Hellen, C.U., D'Souza, V.M. and Wagner, G. (2016) An accurately preorganized IRES RNA structure enables eIF4G capture for initiation of viral translation. *Nat Struct Mol Biol*, **23**, 859-864.
57. Spahn, C.M., Jan, E., Mulder, A., Grassucci, R.A., Sarnow, P. and Frank, J. (2004) Cryo-EM visualization of a viral internal ribosome entry site bound to human ribosomes: the IRES functions as an RNA-based translation factor. *Cell*, **118**, 465-475.
58. Filbin, M.E. and Kieft, J.S. (2009) Toward a structural understanding of IRES RNA function. *Curr Opin Struct Biol*, **19**, 267-276.
59. Martinez-Salas, E., Francisco-Velilla, R., Fernandez-Chamorro, J., Lozano, G. and Diaz-Toledano, R. (2015) Picornavirus IRES elements: RNA structure and host protein interactions. *Virus Res*, **206**, 62-73.
60. Brown, E.A., Zajac, A.J. and Lemon, S.M. (1994) *In vitro* characterization of an internal ribosome site (IRES) present within the 5′ nontranslated region of hepatitis A virus RNA: comparison with the IRES of encephalomyocarditis virus. *Journal of Virology*, **68**, 1066-1074.
61. Arhab, Y., Bulakhov, A.G., Pestova, T.V. and Hellen, C.U.T. (2020) Dissemination of internal ribosomal entry sites (IRES) between viruses by horizontal gene transfer. *Viruses*, **12**, 612.
62. Yu, Y., Sweeney, T.R., Kafasla, P., Jackson, R.J., Pestova, T.V. and Hellen, C.U. (2011) The mechanism of translation initiation on Aichivirus RNA mediated by a novel type of picornavirus IRES. *EMBO J*, **30**, 4423-4436.
63. Bassili, G., Tzima, E., Song, Y., Saleh, L., Ochs, K. and Niepmann, M. (2004) Sequence and secondary structure requirements in a highly conserved element for foot-and-mouth disease virus internal ribosome entry site activity and eIF4G binding. *J Gen Virol*, **85**, 2555-2565.
64. Li, Y., Zhang, L., Wang, L., Li, J., Zhao, Y., Liu, F. and Wang, Q. (2024) Structure and function of type IV IRES in picornaviruses: a systematic review. *Front Microbiol*, **15**, 1415698.
65. Asnani, M., Kumar, P. and Hellen, C.U. (2015) Widespread distribution and structural diversity of Type IV IRESs in members of *Picornaviridae*. *Virology*, **478**, 61-74.

66. Schüler, M., Connell, S.R., Lescoute, A., Giesebrecht, J., Dabrowski, M., Schroeer, B., Mielke, T., Penczek, P.A., Westhof, E. and Spahn, C.M. (2006) Structure of the ribosome-bound cricket paralysis virus IRES RNA. *Nat Struct Mol Biol*, **13**, 1092-1096.
67. López de Quinto, S. and Martínez-Salas, E. (1997) Conserved structural motifs located in distal loops of aphthovirus internal ribosome entry site domain 3 are required for internal initiation of translation. *Journal of Virology*, **71**, 4171-4175.
68. Kühn, R., Luz, N. and Beck, E. (1990) Functional analysis of the internal translation initiation site of foot-and-mouth disease virus. *Journal of Virology*, **64**, 4625-4631.
69. Niepmann, M., Peterson, A., Meyer, K. and Beck, E. (1997) Functional involvement of polypyrimidine tract-binding protein in translation initiation complexes with the internal ribosome entry site of foot-and-mouth disease virus. *Journal of Virology*, **71**, 8330-8339.

Chapter 3: Biophysical Characterization of the Deformed Wing Virus 3′ Untranslated Region

3.1 Foreword

This chapter is based on unpublished work conducted with the help of SarahAnn Walker, Dr. Higor Pereira, and Dr. Trushar Patel. I performed all wet laboratory experiments, with assistance from SarahAnn Walker. I analyzed all data, and Dr. Pereira assisted with SAXS analysis and computational modelling. I wrote the manuscript, with edits from Dr. Patel.

3.2 Introduction

Deformed wing virus (DWV) is one of the most widespread western honey bee (*Apis mellifera* L.) pathogens (1,2). It was initially isolated from diseased adult honey bees from Japan in 1982 and found distantly related to the Egypt bee virus (3). The isolate was later named DWV because bees had wing deformities (3). Presently, the global distribution of DWV is followed closely by the ectoparasitic mite *Varroa destructor* (4,5). The varroa mite is an efficient vector of DWV, leading to overt infection levels in adult honey bees (6,7). Overt infection is characterized by wing deformities and other abnormalities in workers and drones, including bloated abdomens, discolouration, and reduced body size (7). It can also negatively impact a colony's viability by shortening the lifespan of newly emerged bees (8). Honey bees can also be asymptomatic; however, viral loads can still be very high (9).

Due to the rapid spread of DWV, novel variants are emerging throughout the globe. There are three master variants of DWV which vary in their virulence: DWV-A (10), DWV-B (11), and DWV-C (12). Studies have linked high titres of DWV-A to colony collapse (13,14), a devastating worldwide phenomenon (15). Traditionally, DWV-A has been the dominant variant globally for many years; however, DWV-B has seen a prevalence shift in recent years (16). DWV-B, also known as *Varroa destructor* virus-1 (VDV-1) due to its initial discovery from Varroa, is of concern because of its higher transmission rates and increased virulence (11,16). The newly discovered variant, DWV-C, is less common and not as widely studied; therefore, its impact is relatively unknown (12).

DWV is a positive-sense single-stranded RNA ((+)ssRNA) virus from the picorna-like *Iflaviridae* family (10,17). The genome is 10,188 nucleotides (nt) long and consists of a single

open reading frame (ORF) flanked by long 5′ and 3′ untranslated regions (UTRs) (7,10). UTRs are noncoding RNA regions that play an essential role in the viral replication cycle (18). Studies have shown that the specific RNA structures of viral UTRs are important for function (19). There are many different roles that the secondary and tertiary structures formed in the UTRs play throughout the viral life cycle, including regulating translation, recruiting host factors, genome cyclization, protecting viral RNA, and providing signals for RNA synthesis and genome replication (19-22). The dengue virus 3′ UTR folds into a highly conserved stem-loop that aids in viral replication (23). The 5′ UTR of tick-borne encephalitis virus has stem-loop structures critical for RNA stability and viral replication (24). Some Iflaviruses contain a structured internal ribosome entry site (IRES) element in their 5′ UTR region (25-28), as further shown in Chapter 2. Aside from these studies, little is known about the structural features of Iflavirus UTRs, especially the 3′ UTRs.

Many techniques have been used to determine the structures of UTRs in other viruses, including Selective 2’ Hydroxyl Acylation analyzed by Primer Extension (SHAPE), X-ray crystallography, nuclear magnetic resonance (NMR), small-angle X-ray scattering (SAXS), and structure prediction software (29-33). Biophysical methods, such as SAXS, are commonly employed to study RNA structure because they allow for investigating RNA in its native, solution-state environment. In this study, we use a combination of biophysical and computational techniques to characterize and determine the structure of the DWV 3′ UTR. We used size exclusion chromatography coupled with multi-angle light scattering (SEC-MALS) to determine the absolute molecular weight (M_W) of *in vitro* transcribed and purified DWV 3′ UTR. Through small-angle X-ray scattering (SAXS), we are able to generate the low-resolution *ab initio* envelope model for the DWV 3′ UTR. Furthermore, we fitted models of the SAXS envelope to

high-resolution computationally predicted structures. We show that the DWV 3′ UTR has an elongated structure where the predicted tertiary models follow the shape of the envelope, with some deviation from the overall fit. Overall, this study provides insights into the structural features of the DWV 3′ UTR, laying the foundation for future studies of the DWV 5′ UTR and other Iflavirus UTRs.

3.3 Material and Methods

3.3.1 Plasmid preparation

The DWV 3′ UTR sequence was obtained from the last 341 nt of GenBank accession code MG831200 (DWV-A) and inserted into pUC-GW-Kan (Azenta Life Sciences, USA). The *in vitro* transcription (IVT) construct was created as previously described (34). Briefly, the UTR sequence was controlled by a T7 RNA polymerase promotor, followed by two additional G nucleotides on the 5′ end and a HindIII restriction enzyme cut site (A^AGCTT) on the 3′ end of the sequence. The resulting construct used is as follows:

DWV 3′ UTR (344 nt)

5′GGUAUUUAAUUUUAAAUACUUAUUAAUUUUAAUUUUAUUUUAGGUUAUUGGAAUUGA
GGGAAGUACCACCCCCCAAGACCUUCGUUUUAAAUCUACUAAGAGGAGUAAACCUAUAUA
UAAGAGUCUAAAGACAGAGUGGAUUAGACCAUCAUCUUUAGCUUAUAUAUGGGGAAGGU
UGAGUUGCCUCUAAAGACUCAGCUCCGUAGUAGAGUAGUUUUAAUUACGAUUAAAGUGG
UACUCUAGGUUAGGUGUUACUCGCGUAUUAUCAACUUGUGGUAAUGCGUCCUAAUUUUA
GUAUAGUUUUAACCAUAAUAGUAAAAAAAAAAAAAAAAAAAAAAAAAAA3′

The plasmid was transformed into *Escherichia coli* DH5α competent cells, and a transformant was grown in 250 mL of LB media supplemented with kanamycin antibiotic (50 μg/mL final concentration). Plasmid was purified using GeneJET Plasmid Maxiprep Kits according to the manufacturer's instructions (Thermo Fisher Scientific, USA). The purified plasmid was ethanol precipitated overnight at -80°C and stored at -20°C for downstream reactions. In preparation for IVT, the plasmid was digested overnight with HindIII restriction endonuclease (New England Biolabs, Canada).

3.3.2 Synthesis and purification of RNA

IVT was performed with in-house purified T7 RNA polymerase (35). The reaction mixture was incubated at 37°C for 1 hour and then treated with DNase to digest the remaining plasmid.

Synthesized RNA was purified using size exclusion chromatography (SEC) with a Superdex 200 Increase 10/300 GL column (GE Healthcare Canada Inc., Mississauga, ON) on the AKTA Pure 25 FPLC (GE Healthcare, USA). SEC ran at 0.4 mL/min with RNA buffer (10 mM Bis-tris pH 6.0, 100 mM NaCl, 5 mM $MgCl_2$, 15 mM KCl, 5% glycerol). Elution fractions were assessed for RNA purity using native and formaldehyde agarose gel electrophoresis. Fractions containing pure RNA were pooled and ethanol precipitated overnight at -80 °C. RNA pellets were resuspended in RNA buffer to a concentration of 1.2-1.6 mg/mL for use in downstream experiments.

3.3.3 SEC coupled with multi-angle light scattering (MALS)

To determine the absolute molecular weight (M_W) of the RNA, SEC-MALS was performed on a DAWN Multi-angle Light Scatterer with Optilab Refractive Index System (Wyatt Technology Corporation, Santa Barbara, CA, USA), as outlined in Chapter 2. Briefly, a Shodex KW403-4F (Showa Denko America Inc., New York, NY, USA) SEC column was used in tandem with the MALS. The experiment ran at a flow rate of 0.150 mL/min and ambient room temperature (21°C). The concentration of RNA used was 1.2 mg/mL. The ASTRA v8.0.0.25 software package analyzed data and determined the M_W (35,36). The refractive index increment (dn/dc) was set to 0.172 mL/g during data analyses.

3.3.4 Small-angle X-ray scattering (SAXS)

The B21 Beamline at Diamond Light Source (Didcot, Oxfordshire, UK) was used to collect SAXS data. The concentration of RNA used was 1.6 mg/mL. Datum analysis was performed using the ATSAS suite (37), as previously described (Chapter 2). In brief, CHROMIXS (38) was used to subtract buffer contribution from the raw data. Guinier analysis

(q^2 vs. ln(I(q))) (39) was performed to determine the radius of gyration (R_g) and homogeneity of the RNA, followed by dimensionless Kratky analysis (qRg vs. qRg2*I(q)/I(0)) to determine RNA folding state (40). Paired distance distribution (P(r)) plots were generated to determine real space R_g and the maximum dimension (D_{max}) of the RNA (41). We then used the P(r) data to generate twenty *ab initio* envelope models using DAMMIN (42). These models were then averaged and filtered using DAMAVER and DAMFILT (43) to obtain a single representative model.

3.3.5 Tertiary structure prediction and model fitting

The RNAfold WebServer from the Vienna RNA Websuite (44,45) was used to generate the secondary structure prediction for the DWV 3′ UTR. RNAcanvas was used to visualize the two-dimensional (2-D) secondary structure (46). The lowest free energy secondary structure constraints were inputted into SimRNA v3.20 (47) to predict tertiary structures, creating a total of 2000 clusters. The SAXS envelope was superimposed with the predicted structures using DAMSUP (43), which also determined the normalized spatial discrepancy (NSD). The representative models were filtered using NSD and visual fit, and the best models were visualized using UCSF ChimeraX-1.8 (48).

3.4 Results

3.4.1 DWV 3′ UTR purification and absolute molecular weight determination

We utilized SEC to purify the *in vitro* transcribed DWV 3′ UTR. **Figure 3.1A** shows the elution profile after SEC, with a large peak from ~10-12 mL and a small shoulder peak from ~9-10 mL. A non-denaturing agarose gel (**Figure 3.1B**) verified that the prominent peak contained monomeric DWV 3′ UTR. The DWV 3′ UTR was seen as a prominent band below the 400 nt marker from ~10-11 mL (pink). These fractions were pooled for downstream use. The shoulder peak, from ~9-9.5 mL (blue), contained some oligomeric species, which were avoided for downstream use. A denaturing formaldehyde agarose gel was used to verify RNA purity with the 10.5 mL elution fraction (**Figure 3.1C**). There was minimal RNA degradation, and the band migrated around the 400 nt marker.

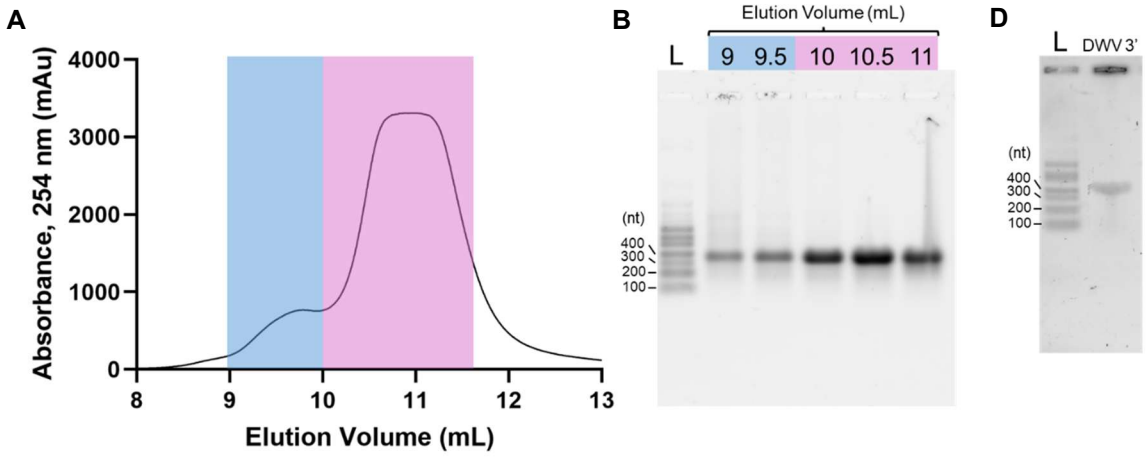

Figure 3.1. Size exclusion chromatography (SEC) purification of *in vitro* transcribed DWV 3′ UTR. (**A**) Chromatogram after RNA purification on the Superdex 200 Increase 10/300 GL column in RNA Buffer. (**B**) Non-denaturing 1.5% agarose gel visualizing the SEC elution fractions. Blue lanes are fractions from 9-9.5 mL, and pink lanes from 10-11 mL. The gel was run at 50V for 60 min. (**C**) Denaturing 1.5% formaldehyde agarose gel of the 10.5 mL fraction, confirming the integrity of the RNA. The gel was run at 50V for 68 min. Both gels used the RiboRuler Low-Range RNA Ladder (Thermo Fisher Scientific, USA) and were stained with SYBR Gold Nucleic Acid Gel Stain (Thermo Fisher Scientific, USA).

The absolute M_W of the DWV 3′ UTR in solution was determined using SEC-MALS. SEC-MALS is an analytical biophysical technique that is used to characterize macromolecules. It combines SEC separation with MALS, where light is scattered from a macromolecule and detected at multiple angles (49). By analyzing the intensity of scattered light at many angles, the concentration, and the $(dn/dc)^2$ of a macromolecule, the absolute M_W of a biomolecule can be determined (50,51). **Figure 3.2** displays the resulting MALS trace after SEC purification, illustrating a peak at ~3.0 mL. A shoulder peak eluting at a smaller volume (not shown) indicated oligomeric species separated during SEC. The M_W across the main peak was relatively constant and was calculated to be 92.46 ± 2.67 kDa, whereas the theoretical M_W is 110 kDa. While the error is relatively low, the calculated M_W was ~18 kDa smaller than the theoretical M_W. Overall, the low error and uniformity of the M_W indicated that the separated DWV 3′ UTR was relatively homogenous.

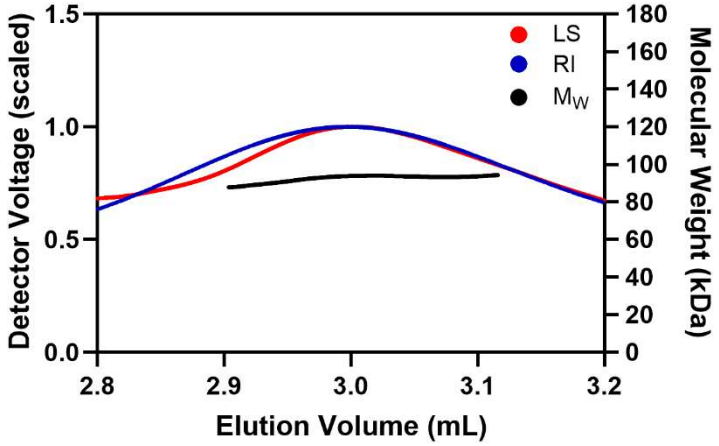

Figure 3.2. SEC-coupled multi-angle light scattering (MALS) trace for determining the absolute molecular weight (Mw) of the DWV 3′ UTR. Light scattering (LS, red), refractive index (RI, blue), and molecular weight (M_W, black) calculation across the peak. The calculated M_W from the prominent peak is 92.46 ± 2.67 kDa.

3.4.2 Low-resolution structure determination of the DWV 3′ UTR in solution

SAXS was utilized to elucidate the structure and biophysical properties of the DWV 3′ UTR in solution. Biophysical properties obtained from SAXS are outlined in **Table 3.1**. As seen

in **Figure 3.3A**, the raw scattering data was adjusted for background scattering and depicts scattering intensity versus scattering angle. Guinier analysis was first completed to determine the monodispersity of the sample (**Figure 3.3B**). The resulting Guinier plot is linear, meaning that the DWV 3′ UTR was homogenous, and it was appropriate to continue with further analysis (39). The Guinier R_g, a measure of a macromolecule's size in solution, was also calculated to be 59.62 ± 0.20 Å (**Table 3.1**).

The data was further transformed into a dimensionless Kratky plot to reveal the folded or unfolded state of the sample (52). **Figure 3.3C** revealed a plateaued plot, suggesting that the DWV 3′ UTR was elongated and folded (53). Furthermore, to determine the overall shape and D_{max} of the RNA, a P(r) plot was generated, as seen in **Figure 3.3D**. The P(r) plot provided information on real-space electron pair distance distribution, helping determine the relative shape of a molecule (54). The plot revealed a sharp increase in the maxima and a gradual decrease in the D_{max}. This specific shape of the curve indicated that the RNA was elongated. Using this plot, we have calculated a D_{max} of 189 Å and a real-space R_g of 60.16 ± 0.19 Å (**Table 3.1**).

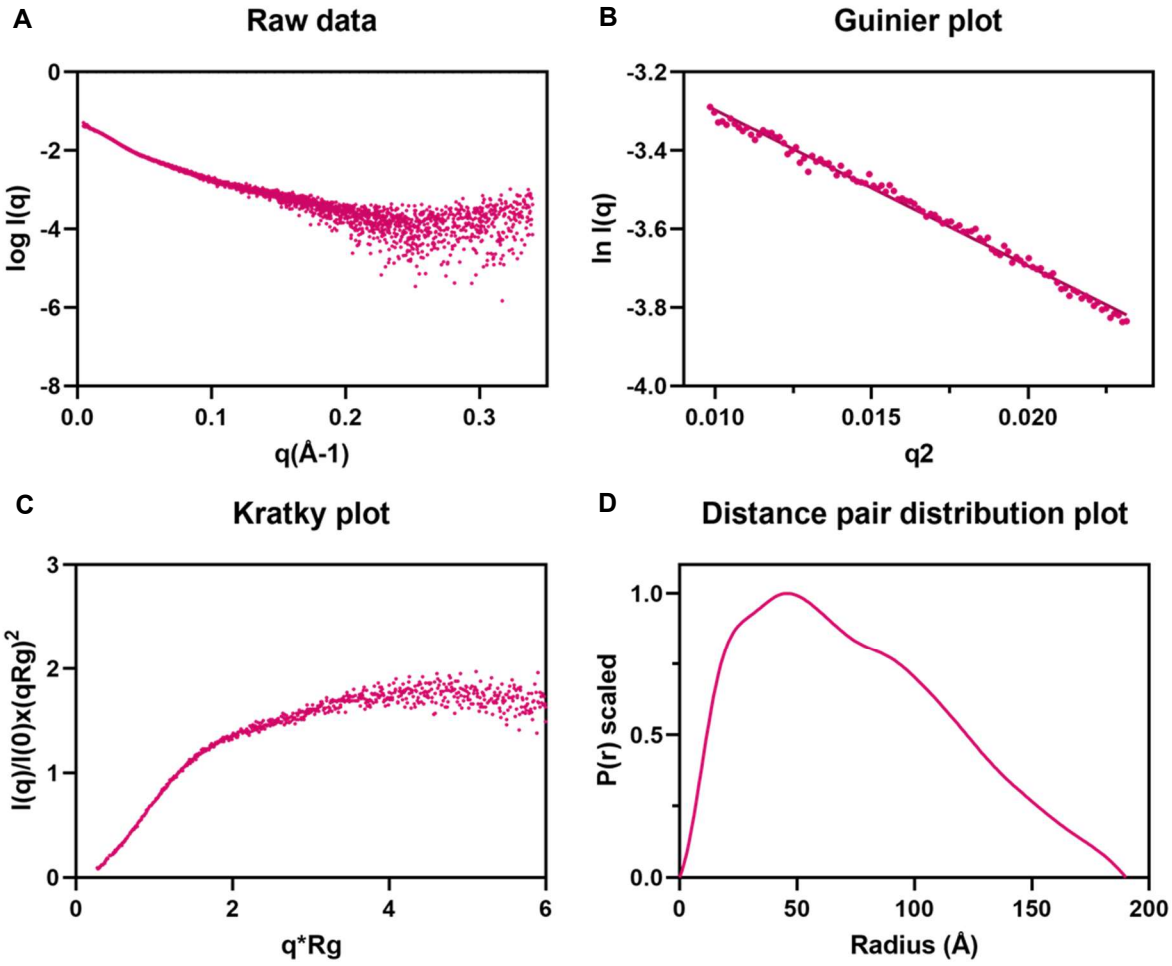

Figure 3.3. Small-angle X-ray scattering (SAXS) data analysis of the DWV 3′ UTR. (**A**) Raw scattering data that represents scattering intensity (log I(q)) vs. scattering angle ($q = 4\pi\sin\Theta/\lambda$). (**B**) Guinier analysis (ln I(q) vs. q^2), where a linear plot indicates sample homogeneity and the determination of R_g. (**C**) Dimensionless Kratky plot ($(I(q)/I(0)*(q*R_g)^2$ vs. $q*R_g$) that depicts the elongated structure of the DWV 3′ UTR. (**D**) Distance pair distribution plot (P(r)) where the radius indicates the maximum dimension (D_{max}) and illustrates that the DWV 3′ UTR has an elongated shape. The D_{max} is shown at 189 Å.

Table 3.1. Biophysical parameters of the DWV 3′ UTR determined from small-angle X-ray scattering (SAXS) analysis.

Parameters	DWV 3′ UTR
SAXS Molecular Weight (kDa)	118.94
Guinier R_g (Å)	59.62 ± 0.20
Guinier I(0)	0.0394
P(r) R_g (Å)	60.16 ± 0.19
P(r) I(0)	$0.0394 \pm 0.13 \times 10^{-4}$
D_{max}(Å)	189
X^{2*}	~1.07
NSD*	0.98 ± 0.03

Data points * were derived from DAMMIN and DAMAVER analysis. Terms: Scattering intensity at zero angle (I(0)); radius of gyration (R_g); maximum dimension (D_{max}); goodness-of-fit parameter (X^2); and normalised spatial discrepancy (NSD)

Using the P(r) data, low-resolution envelope structures were generated for the DWV 3′ UTR. Twenty *ab initio* bead models were generated using DAMMIN (42) with favourable goodness-of-fit parameter (X^2) values of ~1.07, indicating the models fit the SAXS data. DAMAVER and DAMFILT (43) were utilized to average and filter the generated models into a single representative model for the DWV 3′ UTR, as shown in **Figure 3.4**. The envelope had a favourable NSD value of 0.98 ± 0.03. As predicted from the P(r) distribution, the DWV 3′ UTR had an elongated structure in solution. Additionally, the envelope was asymmetrical and had a bulge located near the middle of the RNA.

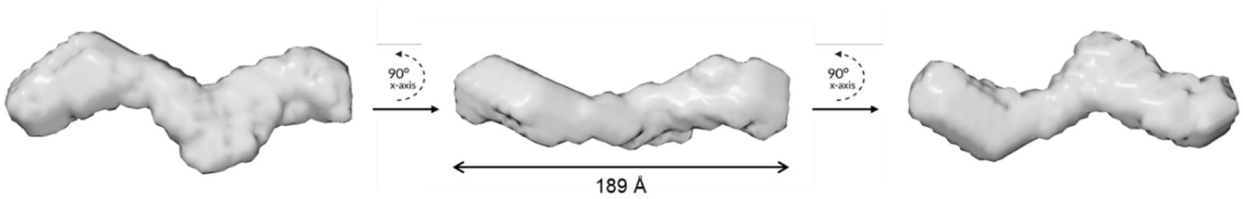

Figure 3.4. Low-resolution SAXS envelope of the DWV 3′ UTR. Portrayed is the averaged and filtered representative model generated using DAMAVER and DAMFILT. A prominent feature is the bulge near the middle of the envelope. The model is rotated along the X-axis by 90°. Dimension represents the D_{max} of 189 Å obtained from the P(r) plot. Visualized using ChimeraX-1.8 (48).

3.4.3 High-resolution atomistic model structure prediction of the DWV 3′ UTR

The RNAfold WebServer (44,45) was used to predict the minimum free energy secondary structure of the DWV 3′ UTR. The resulting 2-D secondary structure, as seen in **Figure 3.5**, contained a long, structured, multibranched loop domain. The domain contained multiple stems and stem-loop (SL) motifs. After an initial small SL (grey), there was a sizeable multi-branch loop that contained a four-way and three-way junction. The four-way junction, stemming from a ~15 nt long stem (red), consisted of two SLs (orange and purple) and a bent stem (yellow) that lead into the three-way junction. The three-way junction consisted of a longer bent SL (green) and a shorter SL (blue). The 3′ end of the RNA illustrated the 28 nt long poly-adenylated (poly-A) tail (red).

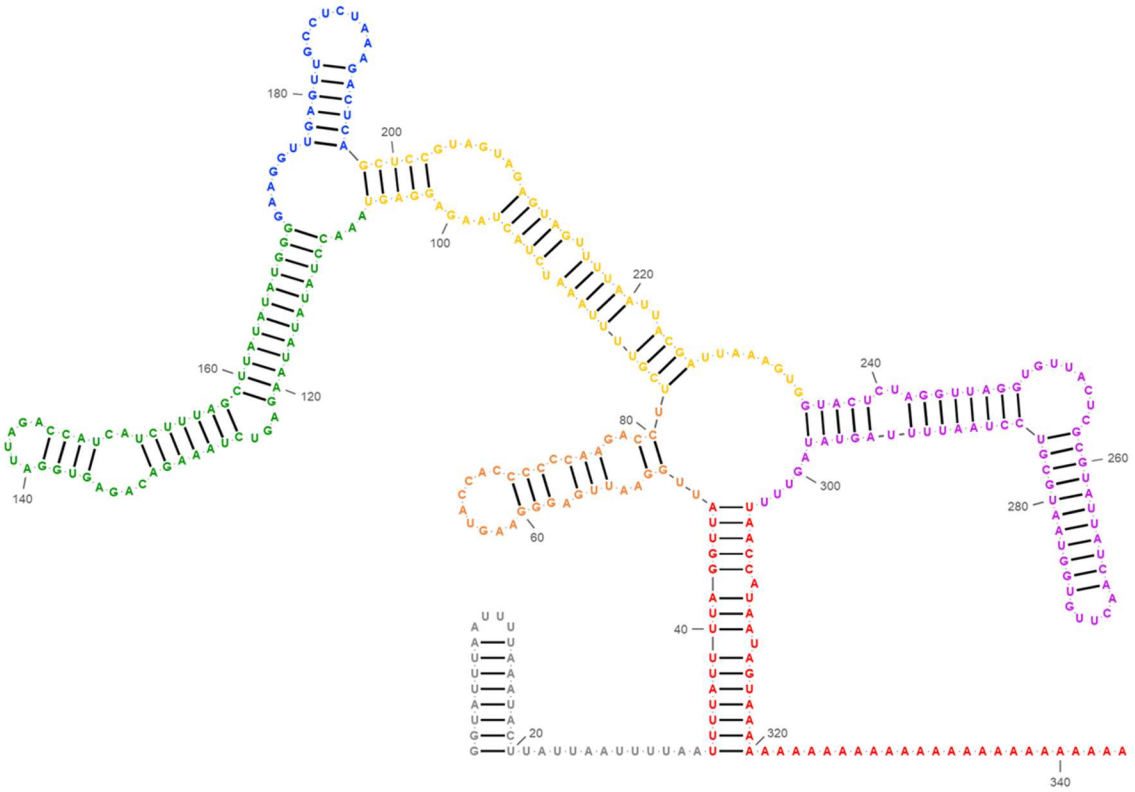

Figure 3.5. 2-D representation of the DWV 3′ UTR secondary structure. Predicted secondary structure generated using the RNAfold Webserver (44,45). Stem and stem-loop (SL) regions are colour-coordinated: an initial short SL (grey), followed by a four-way junction containing red and yellow stems and orange and purple SLs. The three-way junction contains the yellow stem and green and blue SLs. The poly-adenylated tail at the terminal 3′-end of the structure is also shown in red. 2-D structure visualized using RNAcanvas (46).

The predicted secondary structure constraints were inputted into SimRNA v3.20 (47) to obtain high-resolution structures to overlay with the low-resolution SAXS envelope. The predicted DWV 3′ UTR structures were superimposed with the envelope using DAMSUP (43). The three selected alignments shown in **Figure 3.6** were chosen based on low NSD values and visual fitting. Upon visual inspection, all atomistic models follow the relative shape of the SAXS envelope. However, sections from each model appear to be protruding out at some position on the envelope. Model 683 (**Figure 3.6A**) had the best fit, based on an NSD value of 1.29. However, the grey and green SLs stick out of the right and left side of the envelope, respectively.

The longer, bent purple SL near the right side disagrees with the envelope. Model 686 (**Figure 3.6B**) had a similar NSD value of 1.30, but there was some disagreement with the SAXS envelope. Similar to Model 683, the grey and green SLs extend out of the ends of the envelope. The single-stranded poly-A tail (red) protrudes more out of this model, and there was also disagreement with the orange and purple SLs. Model 701 (**Figure 3.6C**) had a higher NSD value of 1.33. This model was similar to model 686, except the poly-A tail extended out even more, and there was more agreeance with the grey SL on the right side of the envelope.

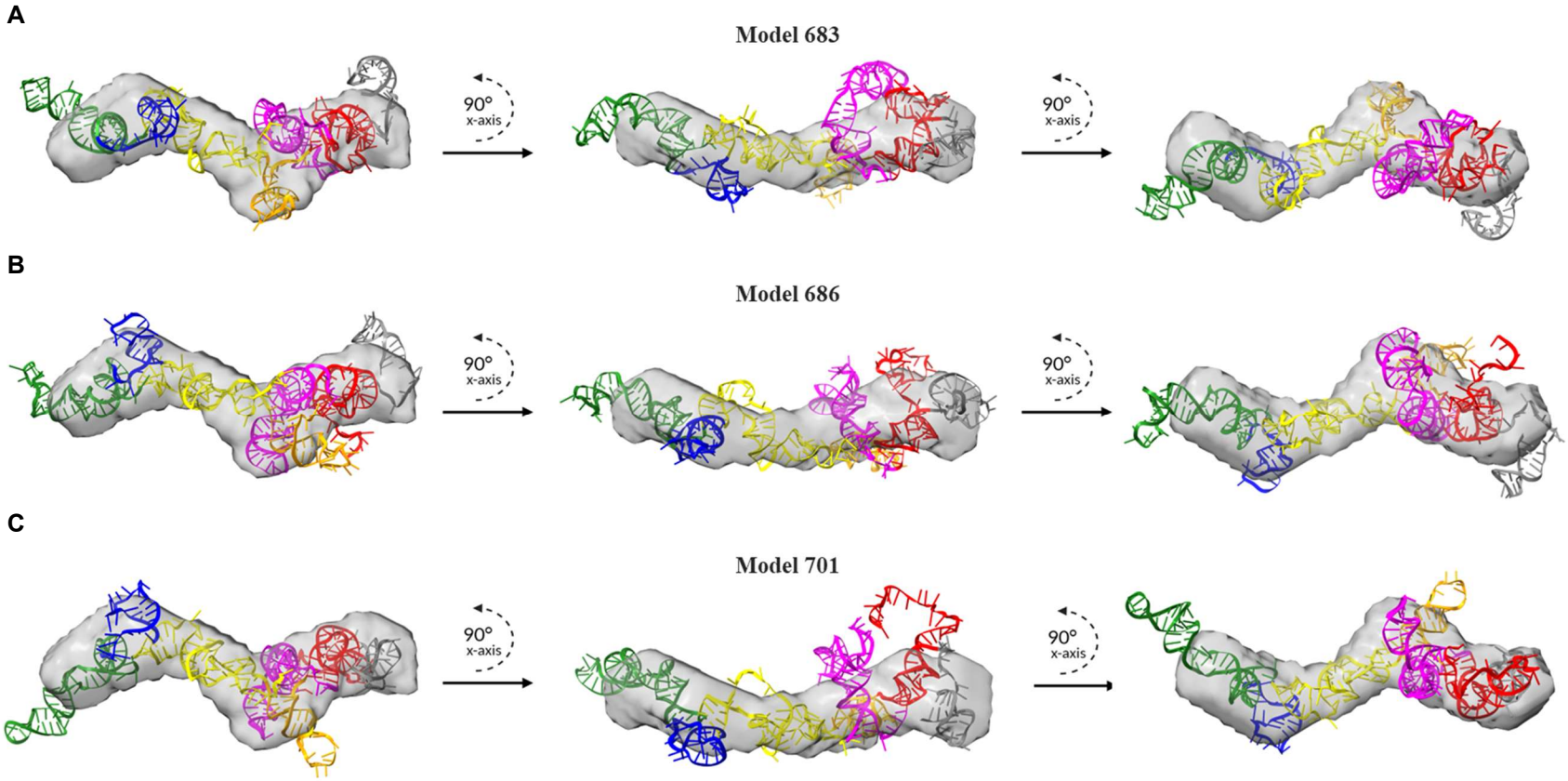

Figure 3.6. SAXS envelope overlayed with atomistic computational models of the DWV 3′ UTR. The top SimRNA models are (**A**) 683, (**B**) 686, and (**C**) 701. Representative models were chosen based on low normalized spatial discrepancy (NSD) values and visual fit. The atomistic models follow the shape of the SAXS envelope; however, there is disagreement with the fit, as seen by regions extending outward of the envelope. Visualized using ChimeraX-1.8 (48).

3.5 Discussion

Structure plays an essential role in the function of a UTR (19,55). Viral UTRs often fold into complex secondary and tertiary structures that mediate interactions with host cellular components (56). Determining these structures is important for identifying key structural features crucial for viral replication and host interactions. Once these elements are better understood, they can be exploited to develop antiviral therapeutics, such as small molecules, to target and disrupt these regions. Despite its importance, the DWV 3′ UTR structure had not been characterized prior to this study, leaving key aspects of its function poorly understood. Therefore, in this study, we investigated the structural features of the DWV 3′ UTR, laying the foundation for understanding its functional role in the viral life cycle.

The DWV 3′ UTR was initially prepared using IVT and purified to homogeneity, as indicated in **Figure 3.1**. Based on non-denaturing and denaturing agarose gels, the RNA appeared pure. Elution fractions were first analyzed using non-denaturing agarose, which illustrated high concentrations of the DWV 3′ UTR from ~10-11 mL that were relatively pure (**Figure 3.1B**). Larger oligomeric species were faintly seen from ~9-9.5 mL, and when pooling fractions, these were avoided to limit RNA heterogeneity for downstream applications. The 10.5 mL fraction was analyzed using denaturing formaldehyde agarose gel electrophoresis to depict the purified RNA's length accurately. The gel showed a pure and homogenous RNA band around 400 nt, slightly higher than the expected 344 nt (**Figure 3.1C**). We then utilized SEC-MALS to determine the absolute M_W of the RNA and check the RNA quality before SAXS.

The MALS trace showed a prominent peak ~3 mL with a relatively uniform M_W calculation (**Figure 3.2**). The absolute M_W was calculated to be 92.46 ± 2.67 kDa, which is

slightly smaller than the theoretical value of 110 kDa. This discrepancy is most likely due to column conditions during SEC-MALS. It is possible that the system used was introducing some degradation through ribonuclease contamination. We do not report RNA degradation at any other step of RNA characterization, from purification of the *in vitro* transcribed product to SAXS. This is evidenced by the reported SAXS M_W of 118.94 kDa (**Table 3.1**), which is closer to our theoretical M_W, indicating that the sample used for SAXS analysis was not degraded. Even though a lower M_W was calculated from SEC-MALS, we determined that the DWV 3′ UTR was monomeric and proceeded with SAXS structure determination.

SAXS is a powerful technique to determine biological molecules' low-resolution three-dimensional (3-D) structures in their solution state (57). SEC, coupled with SAXS, is another measure to purify RNA further and ensure species homogeneity. The initial observation of raw scattering showed appropriately distributed scattering intensities (**Figure 3.3A**). As seen in **Figure 3.3B**, the Guinier analysis revealed a linear plot, illustrating that the DWV 3′ UTR was monodisperse and homogenous (39). The Guinier R_g, a measure of the overall size of a molecule, was determined to be 59.62 ± 0.20 Å (**Table 3.1**), a value consistent with other elongated RNAs (58,59). After verifying homogeneity, the Kratky plot was created to determine the relative foldedness of the DWV 3′ UTR (50). **Figure 3.3C** showed that the RNA was an elongated and folded molecule, like other UTR RNAs (34,35).

To understand more about the shape of the RNA, a P(r) plot was generated. The P(r) distribution utilizes real space data to describe the overall shape of the molecule and the D_{max} (54). Generally, a bell-shaped curve indicates a globular molecule, while extended molecules have an asymmetric curve that gradually tails off (54). Results in **Figure 3.3D** showed an asymmetric curve with a sizeable right-leaning tail, meaning that the DWV 3′ UTR adopted an

extended shape as seen in other RNAs (34,35). The RNA was also shown to have a D_{max} of 189 Å, which is smaller than expected for an RNA of this size (35,58). However, this suggests that the DWV 3′ UTR was folded more tightly than other RNAs. We also determined the real space R_g to be 60.16 ± 0.19 Å, which was similar to the Guinier R_g (**Table 3.1**), further verifying the validity of our data.

The P(r) data was utilized to create the low-resolution envelope structure of the DWV 3′ UTR. Twenty envelope models were initially generated in DAMMIN with favourable X^2 values (**Table 3.1**), indicating agreement between experimental scattering data and the models. A single representative model was then obtained, showing a favourable NSD value below 1 (**Table 3.1**), illustrating that the average envelope model was similar to all generated models (60). The resulting envelope, shown in **Figure 3.4**, illustrated a typical elongated RNA structure, as seen in other studies (34,35,58). As it was rotated along the X-axis, it was evident that the RNA was asymmetrical and had a bulge near the middle of the envelope. While we successfully generated the SAXS *ab initio* model for the DWV 3′ UTR in solution, we were missing information on directionality and needed to employ further techniques.

To understand more about the structural features of the DWV 3′ UTR, we combined the low-resolution envelope structure with high-resolution tertiary structure information. However, the tertiary structure of DWV 3′ UTR has not been determined experimentally. Therefore, we employed computational tools to predict the structure. First, the RNA secondary structure was predicted using the RNAfold WebServer. This program predicts the minimum free energy secondary structure based on the sequence of an inputted RNA (44). As shown in **Figure 3.5**, the resulting structure was a long, structured region with multi-branched loop junctions. A short grey SL occurred at the 5′ end, while the 3′ end featured a single-stranded poly-A tail (red). Following

the grey SL, a single-stranded region leads to the beginning of the four-way junction (red). A bent yellow stem emerged from this junction, leading into the three-way junction. The presence of a four-way junction with longer SLs suggested that the RNA was flexible and may exhibit conformational fluctuations (61). Also, the three-way junction may add some flexibility, as a bulge was present (62). The secondary structure constraints were inputted into SimRNA to predict the tertiary atomistic structure. We can observe the fit between computational and experimental structures by overlaying the predicted tertiary structures with the SAXS envelope.

Overall, the tertiary models followed the shape of the SAXS envelope (**Figure 3.6**), although some sections did not fit ideally. The NSD values for all models were higher than ideal (>1.29), indicating greater discrepancy between the models and the experimental SAXS envelope (63). As discussed previously (Chapter 2), this also indicated conformational heterogeneity, which was seen throughout the models (63,64). Every model adopted a slightly different conformation; however, they all maintained a similar shape throughout. All models showed that the helical green SL of the three-way junction protruded out of the left side of the envelope. Also, the bent purple SL of the four-way junction bulged out of the envelope on all models, with a slightly different conformation in each. Model 683 (**Figure 3.6A**) and Model 686 (**Figure 3.6B**) lacked overlap with the small grey SL on the right side. Additionally, Model 686 and Model 701 (**Figure 3.6C**) disagreed with the poly-A tail, which is expected from a highly flexible structure like a single-stranded poly-A tail. It is plausible that more complex structural elements, such as pseudoknots, are being formed, which the software could not predict. Further experiments, such as SHAPE, could confirm the presence of pseudoknots or other structurally complex elements. Despite the discrepancies with the fittings, the main shape was maintained throughout the models, and they followed the SAXS envelope. These findings provide insights into the

conformational dynamics of the DWV 3′ UTR, which may influence its interactions with host proteins or contribute to its role in viral replication and translation, roles of which have been seen in other viral 3′ UTRs (20,65). In summary, by utilizing SAXS coupled with structural prediction software, we successfully determined the structural representation of the DWV 3′ UTR in solution.

3.6 Conclusion and Future Directions

We successfully biophysically characterized and resolved the solution structure of the DWV 3′ UTR using a combined approach of SEC-MALS, SAXS, and computational modelling. The UTR was determined to be monomeric, with a calculated M_W slightly smaller than expected. SAXS analysis revealed that the *ab initio* envelope of the UTR was asymmetrical and elongated. Furthermore, combining the SAXS envelope with computationally predicted tertiary structures portrayed a conformationally flexible and extended structure. Each model followed the general shape of the envelope; however, we showed regions of each model that did not overlay ideally.

To gain insight into both DWV UTRs, troubleshooting and optimization of the DWV 5′ UTR purification is required to successfully analyze the structure using SAXS. With the workflow established, the biophysical characterization of the longer 5′ UTR should be feasible. Additionally, SHAPE should be performed to obtain experimental insight into the secondary structure of the DWV UTRs, providing a foundation for more accurate tertiary structure predictions. Gaining full insight into the structural features of the DWV UTRs is crucial for our understanding of the Iflavirus mechanisms of infection and replication. These findings lay the groundwork for future studies to uncover therapeutic targets based on structural regions critical for the viral life cycle.

3.7 References

1. Martin, S.J. and Brettell, L.E. (2019) Deformed wing virus in honeybees and other insects. *Annu Rev Virol*, **6**, 49-69.
2. Beaurepaire, A., Piot, N., Doublet, V., Antunez, K., Campbell, E., Chantawannakul, P., Chejanovsky, N., Gajda, A., Heerman, M., Panziera, D. *et al.* (2020) Diversity and global distribution of viruses of the western honey bee, *Apis mellifera*. *Insects*, **11**.
3. Bailey, L. and Ball, B.V. (1991), *Honey Bee Pathology*, pp. 10-34.
4. Wilfert, L., Long, G., Leggett, H.C., Schmid-Hempel, P., Butlin, R., Martin, S.J.M. and Boots, M. (2016) Deformed wing virus is a recent global epidemic in honeybees driven by Varroa mites. *Science*, **351**, 594-597.
5. Anderson, D.L. and Trueman, J.W.H. (2000) *Varroa jacobsoni* (Acari: Varroidae) is more than one species. *Experimental and Applied Acarology*, **24**, 165-189.
6. Ryabov, E.V., Posada-Florez, F., Rogers, C., Lamas, Z.S., Evans, J.D., Chen, Y. and Cook, S.C. (2022) The vectoring competence of the mite *Varroa destructor* for deformed wing virus of honey bees is dynamic and affects survival of the mite. *Frontiers in Insect Science*, **2**.
7. de Miranda, J.R. and Genersch, E. (2010) Deformed wing virus. *J Invertebr Pathol*, **103 Suppl 1**, S48-61.
8. Dainat, B., Evans, J.D., Chen, Y.P., Gauthier, L. and Neumann, P. (2012) Dead or alive: deformed wing virus and *Varroa destructor* reduce the life span of winter honeybees. *Appl Environ Microbiol*, **78**, 981-987.
9. Highfield, A.C., El Nagar, A., Mackinder, L.C., Noel, L.M., Hall, M.J., Martin, S.J. and Schroeder, D.C. (2009) Deformed wing virus implicated in overwintering honeybee colony losses. *Appl Environ Microbiol*, **75**, 7212-7220.
10. Lanzi, G., de Miranda, J.R., Boniotti, M.B., Cameron, C.E., Lavazza, A., Capucci, L., Camazine, S.M. and Rossi, C. (2006) Molecular and biological characterization of deformed wing virus of honeybees (*Apis mellifera* L.). *J Virol*, **80**, 4998-5009.
11. Ongus, J.R., Peters, D., Bonmatin, J.M., Bengsch, E., Vlak, J.M. and van Oers, M.M. (2004) Complete sequence of a picorna-like virus of the genus *Iflavirus* replicating in the mite *Varroa destructor*. *J Gen Virol*, **85**, 3747-3755.
12. Mordecai, G.J., Wilfert, L., Martin, S.J., Jones, I.M. and Schroeder, D.C. (2016) Diversity in a honey bee pathogen: first report of a third master variant of the deformed wing virus quasispecies. *ISME J*, **10**, 1264-1273.
13. Kevill, J.L., de Souza, F.S., Sharples, C., Oliver, R., Schroeder, D.C. and Martin, S.J. (2019) DWV-A lethal to honey bees (*Apis mellifera*): a colony level survey of DWV variants (A, B, and C) in England, Wales, and 32 states across the US. *Viruses*, **11**, 426.
14. Francis, R.M., Nielsen, S.L. and Kryger, P. (2013) Varroa-virus interaction in collapsing honey bee colonies. *PLoS One*, **8**, e57540.
15. Cornman, R.S., Tarpy, D.R., Chen, Y., Jeffreys, L., Lopez, D., Pettis, J.S., vanEngelsdorp, D. and Evans, J.D. (2012) Pathogen webs in collapsing honey bee colonies. *PLoS One*, **7**, e43562.
16. Paxton, R.J., Schafer, M.O., Nazzi, F., Zanni, V., Annoscia, D., Marroni, F., Bigot, D., Laws-Quinn, E.R., Panziera, D., Jenkins, C. *et al.* (2022) Epidemiology of a major honey bee pathogen, deformed wing virus: potential worldwide replacement of genotype A by genotype B. *Int J Parasitol Parasites Wildl*, **18**, 157-171.

17. Valles, S.M., Chen, Y., Firth, A.E., Guerin, D.M.A., Hashimoto, Y., Herrero, S., de Miranda, J.R., Ryabov, E. and ICTV Report Consortium. (2017) ICTV virus taxonomy profile: *Iflaviridae*. *J Gen Virol*, **98**, 527-528.
18. Payne, S. (2017), *Viruses*, pp. 97-105.
19. Liu, Y., Zhang, Y., Wang, M., Cheng, A., Yang, Q., Wu, Y., Jia, R., Liu, M., Zhu, D., Chen, S. *et al.* (2020) Structures and functions of the 3′ untranslated regions of positive-sense single-stranded RNA viruses infecting humans and animals. *Front Cell Infect Microbiol*, **10**, 453.
20. Kloc, A., Rai, D.K. and Rieder, E. (2018) The roles of picornavirus untranslated regions in infection and innate immunity. *Front Microbiol*, **9**, 485.
21. Lin, J.Y., Chen, T.C., Weng, K.F., Chang, S.C., Chen, L.L. and Shih, S.R. (2009) Viral and host proteins involved in picornavirus life cycle. *J Biomed Sci*, **16**, 103.
22. Ng, W.C., Soto-Acosta, R., Bradrick, S.S., Garcia-Blanco, M.A. and Ooi, E.E. (2017) The 5′ and 3′ untranslated regions of the flaviviral genome. *Viruses*, **9**, 137.
23. Alvarez, D.E., De Lella Ezcurra, A.L., Fucito, S. and Gamarnik, A.V. (2005) Role of RNA structures present at the 3′UTR of dengue virus on translation, RNA synthesis, and viral replication. *Virology*, **339**, 200-212.
24. Upstone, L., Colley, R., Harris, M. and Goonawardane, N. (2023) Functional characterization of 5′ untranslated region (UTR) secondary RNA structures in the replication of tick-borne encephalitis virus in mammalian cells. *PLoS Negl Trop Dis*, **17**, e0011098.
25. Lu, J., Zhang, J., Wang, X., Jiang, H., Liu, C. and Hu, Y. (2006) *In vitro* and *in vivo* identification of structural and sequence elements in the 5′ untranslated region of Ectropis obliqua picorna-like virus required for internal initiation. *J Gen Virol*, **87**, 3667-3677.
26. Ongus, J.R., Roode, E.C., Pleij, C.W.A., Vlak, J.M. and van Oers, M.M. (2006) The 5′ non-translated region of *Varroa destructor* virus 1 (genus *Iflavirus*): structure prediction and IRES activity in *Lymantria dispar* cells. *J Gen Virol*, **87**, 3397-3407.
27. Wu, T.Y., Wu, C.Y., Chen, Y.J., Chen, C.Y. and Wang, C.H. (2007) The 5′ untranslated region of *Perina nuda* virus (PnV) possesses a strong internal translation activity in baculovirus-infected insect cells. *FEBS Lett*, **581**, 3120-3126.
28. Li, M., Man, N., Qiu, H., Cai, S., He, X., He, X. and Lu, X. (2012) Detection of an internal translation activity in the 5′ region of *Bombyx mori* infectious flacherie virus. *Appl Microbiol Biotechnol*, **95**, 697-705.
29. Deigan, K.E., Li, T.W., Mathews, D.H. and Weeks, K.M. (2009) Accurate SHAPE-directed RNA structure determination. *PNAS*, **106**, 97-102.
30. Jackson, R.W., Smathers, C.M. and Robart, A.R. (2023) General strategies for RNA X-ray crystallography. *Molecules*, **28**, 2111.
31. Chen, J.L., Bellaousov, S. and Turner, D.H. (2016), *RNA Structure Determination*, pp. 177-186.
32. Chen, Y. and Pollack, L. (2016) SAXS studies of RNA: structures, dynamics, and interactions with partners. *Wiley Interdiscip Rev RNA*, **7**, 512-526.
33. Miao, Z. and Westhof, E. (2017) RNA structure: advances and assessment of 3D structure prediction. *Annu Rev Biophys*, **46**, 483-503.
34. Mrozowich, T., Henrickson, A., Demeler, B. and Patel, T.R. (2020) Nanoscale structure determination of Murray Valley encephalitis and Powassan virus non-coding RNAs. *Viruses*, **12**, 190.

35. Mrozowich, T., Park, S.M., Waldl, M., Henrickson, A., Tersteeg, S., Nelson, C.R., De Klerk, A., Demeler, B., Hofacker, I.L., Wolfinger, M.T. *et al.* (2023) Investigating RNA-RNA interactions through computational and biophysical analysis. *Nucleic Acids Res*, **51**, 4588-4601.
36. Wyatt, P.J. (2014) Measurement of special nanoparticle structures by light scattering. *Anal Chem*, **86**, 7171-7183.
37. Manalastas-Cantos, K., Konarev, P.V., Hajizadeh, N.R., Kikhney, A.G., Petoukhov, M.V., Molodenskiy, D.S., Panjkovich, A., Mertens, H.D.T., Gruzinov, A., Borges, C. *et al.* (2021) ATSAS 3.0: expanded functionality and new tools for small-angle scattering data analysis. *J Appl Crystallogr*, **54**, 343-355.
38. Panjkovich, A. and Svergun, D.I. (2018) CHROMIXS: automatic and interactive analysis of chromatography-coupled small-angle X-ray scattering data. *Bioinformatics*, **34**, 1944-1946.
39. Putnam, C.D. (2016) Guinier peak analysis for visual and automated inspection of small-angle X-ray scattering data. *J Appl Crystallogr*, **49**, 1412-1419.
40. Burke, J.E. and Butcher, S.E. (2012) Nucleic acid structure characterization by small angle X-ray scattering (SAXS). *Curr Protoc Nucleic Acid Chem*, **Chapter 7**, Unit7 18.
41. Svergun, D.I. (1992) Determination of the regularization parameter in indirect-transform methods using perceptual criteria. *J. Appl. Cryst.*, **25**, 495-503.
42. Svergun, D.I. (1999) Restoring low resolution structure of bio macromolecules from solution scattering using simulated annealing. *Biophysical Journal*, **76**, 2879-2886.
43. Volkov, V.V. and Svergun, D.I. (2003) Uniqueness of *ab initio* shape determination in small-angle scattering. *Journal of Applied Crystallography*, **36**, 860-864.
44. Gruber, A.R., Lorenz, R., Bernhart, S.H., Neubock, R. and Hofacker, I.L. (2008) The Vienna RNA websuite. *Nucleic Acids Res*, **36**, W70-74.
45. Lorenz, R., Bernhart, S.H., Höner zu Siederdissen, C., Tafer, H., Flamm, C., Stadler, P.F. and Hofacker, I.L. (2011) ViennaRNA package 2.0. *Algorithms for Molecular Biology*, **6**.
46. Johnson, P.Z. and Simon, A.E. (2023) RNAcanvas: interactive drawing and exploration of nucleic acid structures. *Nucleic Acids Res*, **51**, W501-W508.
47. Boniecki, M.J., Lach, G., Dawson, W.K., Tomala, K., Lukasz, P., Soltysinski, T., Rother, K.M. and Bujnicki, J.M. (2016) SimRNA: a coarse-grained method for RNA folding simulations and 3D structure prediction. *Nucleic Acids Res*, **44**, e63.
48. Meng, E.C., Goddard, T.D., Pettersen, E.F., Couch, G.S., Pearson, Z.J., Morris, J.H. and Ferrin, T.E. (2023) UCSF ChimeraX: tools for structure building and analysis. *Protein Sci*, **32**, e4792.
49. Harding, S.E. (1994) In Jones, C., Mulloy, B. and Thomas, A. (eds.), *Methods in Molecular Biology*. Humana Press, Vol. 22, pp. 85-95.
50. Patel, T.R., Chojnowski, G., Astha, Koul, A., McKenna, S.A. and Bujnicki, J.M. (2017) Structural studies of RNA-protein complexes: A hybrid approach involving hydrodynamics, scattering, and computational methods. *Methods*, **118-119**, 146-162.
51. Wyatt, P.J. (1993) Light scattering and the absolute characterization of macromolecules. *Analytica Chimica Acta*, **272**, 1-40.
52. Rambo, R.P. and Tainer, J.A. (2011) Characterizing flexible and intrinsically unstructured biological macromolecules by SAS using the Porod-Debye law. *Biopolymers*, **95**, 559-571.

53. Durand, D., Vives, C., Cannella, D., Perez, J., Pebay-Peyroula, E., Vachette, P. and Fieschi, F. (2010) NADPH oxidase activator p67(phox) behaves in solution as a multidomain protein with semi-flexible linkers. *J Struct Biol*, **169**, 45-53.
54. Kikhney, A.G. and Svergun, D.I. (2015) A practical guide to small angle X-ray scattering (SAXS) of flexible and intrinsically disordered proteins. *FEBS Lett*, **589**, 2570-2577.
55. Peng, T., Yang, F., Yang, F., Cao, W., Zheng, H. and Zhu, Z. (2023) Structural diversity and biological role of the 5′ untranslated regions of picornavirus. *RNA Biol*, **20**, 548-562.
56. Nalewaj, M. and Szabat, M. (2022) Examples of structural motifs in viral genomes and approaches for RNA structure characterization. *Int J Mol Sci*, **23**, 15917.
57. Svergun, D.I. (2010) Small-angle X-ray and neutron scattering as a tool for structural systems biology. *Biol Chem*, **391**, 737-743.
58. D'Souza, M.H., Mrozowich, T., Badmalia, M.D., Geeraert, M., Frederickson, A., Henrickson, A., Demeler, B., Wolfinger, M.T. and Patel, T.R. (2022) Biophysical characterisation of human LincRNA-p21 sense and antisense Alu inverted repeats. *Nucleic Acids Res*, **50**, 5881-5898.
59. Cantero-Camacho, A., Fan, L., Wang, Y.X. and Gallego, J. (2017) Three-dimensional structure of the 3′X-tail of hepatitis C virus RNA in monomeric and dimeric states. *RNA*, **23**, 1465-1476.
60. Kozin, M.B. and Svergun, D.I. (2001) Automated matching of high- and low-resolution structural models. *J Appl Cryst*, **34**, 33-41.
61. Laing, C. and Schlick, T. (2009) Analysis of four-way junctions in RNA structures. *J Mol Biol*, **390**, 547-559.
62. Carr, C.E. and Marky, L.A. (2018) Increased flexibility between stems of intramolecular three-way junctions by the insertion of bulges. *Biophys J*, **114**, 2764-2774.
63. Konarev, P.V., Petoukhov, M.V. and Svergun, D.I. (2016) Rapid automated superposition of shapes and macromolecular models using spherical harmonics. *J Appl Crystallogr*, **49**, 953-960.
64. Zhang, Y., Zhang, Y., Liu, Z.Y., Cheng, M.L., Ma, J., Wang, Y., Qin, C.F. and Fang, X. (2019) Long non-coding subgenomic flavivirus RNAs have extended 3D structures and are flexible in solution. *EMBO Rep*, **20**, e47016.
65. Rohll, J.B., Moon, D.H., Evans, D.J. and Almond, J.W. (1995) The 3′ untranslated region of picornavirus RNA: features required for efficient genome replication. *J Virol*, **69**, 7835-7844.

Chapter 4: Towards Understanding the Interactions of Sacbrood Virus Untranslated Regions with *Apis mellifera* Proteins

4.1 Foreword

This chapter is based on unpublished work conducted with the help of SarahAnn Walker, Dr. Govi Veerareddygari, Danielle Gemmill, Dr. Shelley Hoover, Jack Moore, and Dr. Trushar Patel. I performed all wet laboratory experiments, with assistance from SarahAnn Walker. Dr. Veerareddygari assisted with DIG-NHS ester RNA labelling, and Danielle Gemmill provided the initial pull-down assay protocol and early pull-down assay support. Dr. Hoover provided the honey bees for the pull-down assays. Mass spectrometry was conducted by Jack Moore at the Alberta Proteomics and Mass Spectrometry Facility at the University of Alberta. I analyzed the mass spectrometry data, and SarahAnn assisted in the protein literature searches. I wrote the manuscript, with editing assistance from Dr. Patel.

4.2 Introduction

Sacbrood virus (SBV, *Morator aetatulas*) was the first virus known to infect honey bees (*Apis mellifera* L.) (1). Currently, it is one of the most common honey bee viruses found worldwide (2). In a 2017 survey, SBV was one of the most prevalent viruses detected in Canada (3). SBV can cause detrimental effects on a colony, with two-day-old larvae being most susceptible to infection (4). The larvae fail to pupate, and replicated particles of SBV accumulate in the ecdysial fluid underneath the skin, forming a sac-like appearance (5). Eventually, the larvae die and dry into a dark, leathery cuticle. Adult honey bees can also be infected with SBV; however, they are usually asymptomatic (2). Infected nurse bees can quickly spread the virus by feeding larvae and sharing food with other adult bees, including the queen, who can then lay infected eggs (6). The gradual mortality of a colony's developing bees leads to reduced productivity and overall colony population (7). Unfortunately, there are no direct treatments for combatting SBV or other honey bee viruses, which makes researching them pertinent.

The *Picornavirales* order is a "supergroup" of several picorna-like viral families, including the *Iflaviridae* family, to which SBV belongs (8). Viruses grouped in *Iflaviridae* are composed of a positive-sense single-stranded RNA ((+)ssRNA) genome (9). SBV has one open reading frame (ORF) encoding for a single polyprotein that is proteolytically processed into structural (N-terminal) and non-structural (C-terminal) proteins (9). The single ORF is flanked by a 5′ and 3′ untranslated region (UTR), sections of noncoding RNA crucial in regulating the viral life cycle (10).

The UTRs of ssRNA viruses are structured regions of RNA that play many roles in the viral life cycle, including translation regulation, viral replication, RNA stability, and genome

packaging (11-14). Many of these roles are facilitated by host RNA-binding proteins (RBPs) that viruses hijack to promote their propagation (15). For example, the family of picornaviruses have been shown to interact with cellular factors (16). Picornaviruses have an internal ribosome entry site (IRES) in their 5′ UTR capable of mediating cap-independent translation initiation (17). IRES-mediated initiation usually occurs through interaction with host proteins, including eukaryotic initiation factors (eIFs) and IRES trans-acting factors (ITAFs) (17,18). Studies have demonstrated that the La autoantigen (19-21), pyrimidine tract-binding protein (PTB) (22), and eIF4G (23) can bind to the picornavirus 5′ UTR and help facilitate translation initiation via the IRES element. Moreover, the 3′ UTR of picornaviruses have also been shown to bind to host factors (24,25), such as the nucleolar protein nucleolin (26).

While picornavirus-host interactions have been heavily researched, little is known about Iflaviruses engaging with their host. Studies have demonstrated that select Iflaviruses contain an IRES within the 5′ UTR (27-30). However, these studies do not explore the host factors required for IRES function. A common way to identify RBPs is through an RNA immunoprecipitation pull-down assay (31), which typically involves *in vitro* transcribed RNA bound to a linker molecule (i.e., digoxigenin, biotin, desthiobiotin) that can bind to appropriately crosslinked magnetic beads (32). Digoxigenin (DIG) is a popular small molecule used in labelling RNA, as it reduces false-positive identification of RBPs (33).

In this chapter, we aim to determine RBPs that interact with the SBV 5′ and 3′ UTRs and further understand the relevancy of this interaction. Based on the discovery that the SBV 5′ UTR has an IRES element (Chapter 2), we hypothesize that this region may recruit eIFs and ITAFs to aid IRES-mediated initiation. However, factor recruitment is not a requirement for all IRESs (34). We also hypothesize that the UTRs will bind proteins associated with insect immunity,

such as the honey bee antimicrobial peptide apidaecins, abaecins, hymenoptaecins, and defensins (35,36). DIG-labelled RNA immunoprecipitation pull-down assays were performed to determine lists of potential RBPs interacting with the SBV 5′ and 3′ UTRs. Functional and biological relationships among the identified proteins were mapped to uncover patterns and insights into their potential roles in the viral life cycle. Notably, two proteins associated with the SBV 5′ UTR and three with the 3′ UTR emerged as higher confidence candidates for true RBPs with binding potential. These interactions shed light on the potential molecular interactions between SBV and its host and provide the opportunity for future development of antiviral therapeutics to target these proteins and disrupt the viral life cycle.

4.3 Materials and Methods

4.3.1 Plasmid preparation

Constructs for the *in vitro* transcription (IVT) of the SBV 5′ and 3′ UTRs were derived from Genbank accession code MG545286. The SBV 5′ UTR comprises the genome's first 188 nucleotides; the 3′ UTR is the last 93 nucleotides. Scrambled RNA sequences were also created as a control for the pull-down assays. These constructs contained the same nt as the wildtype (WT) RNA but were rearranged using the Sequence Manipulation Suite to Shuffle DNA (37). Predicted secondary structures of each scrambled and WT RNA were generated and compared using the RNAfold WebServer (38,39). Constructs were designed with an upstream 5′ T7 RNA polymerase promoter with two additional G nucleotides, followed by a HindIII restriction enzyme cut site (A^AGCTT) downstream, as previously described (Chapter 2). The sequences were inserted into pUC-GW-Kan (Azenta Life Sciences, USA) and were as follows:

1. SBV 5′ UTR (191 nt)

5′GGGAAAUAAGAAUACGAAUCGUGAUUCGAUUCAUUGUUUCGCCUGAGUAAAUC
GAGAUUUACCUUGACGGGGUUUGCUUGACGUUGCGUCAGACCCGUUUUCCUUGU
GAUUUUUAGGUUGUGAAGAUUUAUUCGAGGAAGUUAAUUAAACAGAAAGUUUAU
UAUAUAGACAGAGACAUAAUAAGUUUAUUA 3′

2. Scrambled 5′ UTR (191 nt)

5′GGUAACAUUAUUUUUCUUGUGGCAGGAUCUCAUUUAGAGGCGCCCAUUAAUAU
AGUCUCAAUUUACGGAACAAUGUGAUUCUGUGUACUAAAUUUGGAUUAACAAAC
UAUUCUUUGAGUUUAAUAAGGGACGAAGAUUUUCGAGAUGUUGGCUUACUACGG
AGAGAUUGUUGUAUCGAGGAAAUUGUAAGA 3′

3. SBV 3′ UTR (96 nt)

5′GGUGUUUUUUAAGGUCUCAUAUAUGCUAUAAAGGUUAUGGGUACUAAUAUAGU
GGAUUAAUAUCAAUAUAUGGCAUUUUAAAAAAAAAAAAAAAAA 3′

4. Scrambled 3′ UTR (96 nt)

5′GGGACAUGAGAGGAAUAAAUUAUUAUAAAAAUUUAAUAAGUUAAGACAUAUAA
AUGAUUGAGUAUCUGUUACUUUCCAUAAUGAUAUUAUUAGAGA 3′

The plasmids were transformed into *Escherichia coli* DH5α competent cells. Transformants were grown overnight in 250 mL of LB media supplemented with kanamycin antibiotic, and plasmids were purified using GeneJET Plasmid Maxiprep Kits according to the manufacturer's instructions (Thermo Fisher Scientific, USA). Plasmids were ethanol precipitated overnight at -80°C and stored at -20°C for downstream reactions.

4.3.2 RNA purification

Purified plasmids were digested overnight with HindIII restriction endonuclease (New England Biolabs, Canada). IVT reactions were prepared using in-house purified T7 RNA polymerase and incubated at 37°C for 2-4 hours, as previously mentioned (40). Synthesized RNA was purified using size exclusion chromatography (SEC). A Superdex 200 Increase 10/300 GL (S200) column (GE Healthcare, USA) was used on the AKTA pure 25 FPLC (GE Healthcare, USA). RNA was eluted using RNA buffer (10 mM Bis-tris pH 6.0, 100 mM NaCl, 15 mM KCl, 5 mM $MgCl_2$, and 5% glycerol). Eluted RNA fractions were pooled, and ethanol precipitated overnight at -80°C.

4.3.3 Digoxigenin (DIG) labelling of RNA

Two protocols were used to label RNA with DIG. First, 30 µM of purified RNA sample was labelled with 5 nt 3′-DIG (IDT, USA) using T4 RNA Ligase (Thermo Fisher Scientific, USA). The prepared reaction was incubated overnight at 16°C. DIG-labelled RNA was purified using the Monarch RNA Cleanup Kit, according to the manufacturer's instructions (New England Biolabs, Canada). The labelling was verified using agarose gel electrophoretic mobility shift assays (EMSAs) with monoclonal mouse anti-digoxin antibodies (Jackson Immunoresearch,

USA). Labelling efficiency was analyzed using ImageJ software (41). This protocol was performed to prepare four replicates of the WT SBV 3′ UTR and Scrambled 3′ UTR.

The second protocol utilized is as follows. Purified RNA was mixed with 65.2 µmol of 1-ethyl-3-[3-dimethylaminopropyl]carbodiimide hydrochloride (EDC) and ethylenediamine/imidazole solution. An additional amount of 0.1 M imidazole (pH 6.0) was added, and the pH of the reaction was adjusted to around 6.0-7.0 as needed. The reaction was incubated at 37°C for 2 hours and purified using a S200 column. RNA fractions were collected and ethanol precipated overnight. The RNA pellet was dissolved in 100 mM sodium borate (pH 8.5) and incubated with Digoxigenin-3-O-methylcarbonyl-ε-aminocaproic acid-N-hydroxysuccinimide (DIG-NHS) ester (MilliporeSigma Canada Ltd., Canada) overnight at 4°C. DIG-labelled RNA was purified using the S200 column. Labelling was confirmed, as mentioned above. This protocol was performed to prepare three replicates of the WT SBV 5′ UTR and two of the Scrambled 5′ UTR.

4.3.4 Crosslinking the A/G magnetic beads

To facilitate the pull-down assays, the magnetic beads must be crosslinked with anti-digoxin antibodies so that they may bind the DIG-labelled RNA. Employing the combination of labelled RNA and crosslinked beads allows for stringent washes to ensure only strongly interacting RBPs are left after the pull-down. Pierce Protein A/G Magnetic Beads (Thermo Fisher Scientific, USA) were washed with phosphate-buffered saline (PBS) with the help of a DynaMag Magnet (Thermo Fisher Scientific, USA). Monoclonal mouse anti-digoxin antibody (Jackson Immunoresearch, USA) was incubated with the magnetic beads at 4°C for 1 hour. After being rinsed with PBS again, the beads were washed with 0.2 M triethanolamine (pH 8.2) and

incubated in 25 mM dimethyl pimelimidate and 0.2 M triethanolamine (pH 8.2) at room temperature for 45 minutes. Fresh dimethyl pimelimidate was added at 15-minute intervals. Beads were washed with 0.1 M ethanolamine (pH 8.2) and incubated with ethanolamine at room temperature for 30 minutes. Beads were washed again with PBS and then resuspended in 0.1 M glycine (pH 2.5). A final bead wash was done using PBS with 0.1% TWEEN and 0.02% sodium azide, and beads were then stored in this solution. The crosslinked beads were stored at 4°C and used within 1 week.

4.3.5 Pull-down assays and mass spectrometry analysis

The crosslinked A/G magnetic beads were equilibrated in Lysis Buffer (50 mM Tris [pH 7.0], 150 mM NaCl, 1% NP-40, 1x HALT protease and phosphate inhibitor, Ribolock). DIG-labelled RNA was added to the bead/Lysis Buffer mixture at 4°C for 1 hour. A negative control was also performed, where no RNA was added to the bead/Lysis Buffer mixture to account for proteins that may interact with the crosslinked beads.

The adult honey bees (*A. mellifera*) used for the pull-downs were sampled in July 2021 from colonies housed at the University of Lethbridge in Lethbridge, AB, Canada. Honey bees were collected from a random sweep of a 50 mL Falcon tube over a wax comb containing brood, immediately submerged into dry ice, and stored at -80°C until further use. Around 30-40 honey bees were washed with PBS in the 4°C cold room. The bees were macerated with a pre-chilled stainless-steel mortar and pestle with Lysis Buffer until sufficiently lysed and homogenous. Once transferred into microfuge tubes, the macerate was centrifuged at 16,100xg at 4°C for 10 minutes. The supernatant was filtered through a 0.45 µm syringe filter and centrifuged again. Buffer was aspirated off the beads, and the filtered honey bee lysate was incubated with the

crosslinked beads at 4°C for 2 hours. The beads were washed 3x with Lysis Buffer to remove loosely bound proteins. Beads and bound proteins were resuspended in 6x loading dye (10% SDS, 500 mM DTT, 50% glycerol, 500 mM Tris-HCl, 0.05% bromophenol blue). Samples were heated at 95°C for 5 minutes, loaded into sodium dodecyl sulphate polyacrylamide gel electrophoresis (SDS-PAGE) gels (6% stacking, 12% resolving), and ran at 120-200V for 10-15 minutes or 1 cm into the gel. Gels were fixed in 50% ethanol and 2% phosphoric acid and stained overnight with mass spectrometry staining solution (10% phosphoric acid, 10% ammonium sulphate, 0.12% Coomassie Blue G-250, 20% methanol). Protein bands were excised from stained gels and submitted to the Alberta Proteomics and Mass Spectrometry Facility (Jack Moore, University of Alberta, Canada) for RNA-binding protein (RBP) identification by liquid chromatography-tandem mass spectrometry.

4.3.6 Bioinformatic analysis of mass spectrometry data

Mass spectrometry (MS) results were analyzed and filtered to determine potential RBPs. Proteins were filtered to exclude overlapping proteins in the Scrambled RNA and control samples. The resulting total protein hits (TPHs) were inputted into the Search Tool for the Retrieval of Interacting Genes/Proteins (STRING) V12.0 (42). STRING creates a network of known and predicted protein-protein interactions with a minimum required interaction score of 0.700 (high confidence). TPHs were submitted into BlastKOALA (Basic Local Alignment Search Tool (Blast) for the Kyoto Encyclopedia of Genes and Genomes (KEGG) Orthology and Links Annotation), which takes amino acid sequences and assigns them functional categories, known as KEGG orthology numbers (43). High-hit proteins (HHPs) of interest were determined by their high MS score, presence in multiple replicates, and molecular function.

4.4 Results

4.4.1 Purification of *in vitro* transcribed SBV 5′ and 3′ UTRs

SEC was used to purify *in vitro* transcribed SBV 5′ UTR, 3′ UTR, and the Scrambled UTRs, which were used as a negative control. **Figures 4.1A** and **B** display the elution profiles of the SBV 5′, SBV 3′, and Scrambled UTRs using the S200 column. The SBV 5′ UTR profile showed a standalone peak from ~11.5-13 mL, whereas the 5′ Scrambled UTR eluted at a lower volume of ~9-11.5 mL, resulting in a wider peak (**Figure 4.1A**). The SBV 3′ UTR also showed a standalone peak from ~13.5-15 mL, whereas the 3′ Scrambled UTR eluted at a lower volume of ~11.5-13 mL (**Figure 4.1B**). The 3′ Scrambled UTR elution profile showed some degradation at higher volumes (~14-15.5 mL); however, these elution fractions were avoided for downstream use.

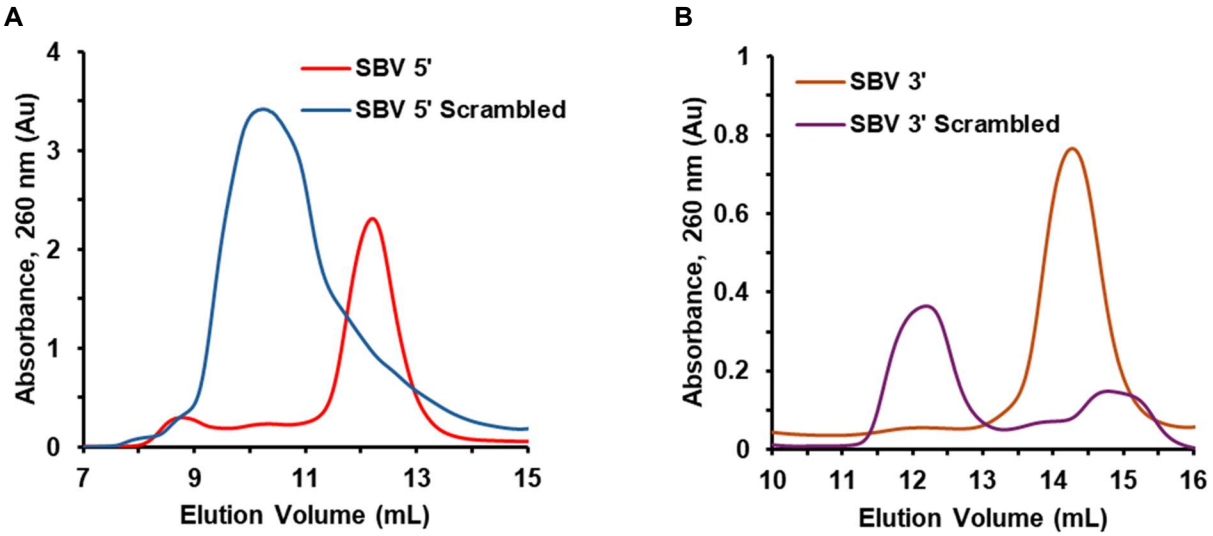

Figure 4.1. Size exclusion chromatography (SEC) purification of the SBV wildtype and Scrambled UTRs. (**A**) The SBV 5′ UTR (red) and 5′ Scrambled UTR (blue) elution profiles. The 5′ UTR elution fractions were collected from ~11.5-13 mL, whereas the 5′ Scrambled UTR were collected from ~9-11.5 mL. (**B**) The SBV 3′ UTR (orange) and 3′ Scrambled UTR (purple) elution profiles. The 3′ UTR elution fractions were collected from ~13.5-15 mL, whereas the 3′ Scrambled UTR were collected from ~11.5-13 mL. Purification was performed on the Superdex 200 10/300 GL column.

4.4.2 DIG-labelling efficiency

Purified RNA was used in DIG-labelling reactions. The T4 RNA ligase and EDC modification protocols were used with varying efficiency. EMSAs were performed to confirm successful labelling and measure labelling efficiency. **Figure 4.2A/B** shows that successful DIG labelling resulted in an RNA band shift when the anti-digoxin antibody (Ab) was added with labelled RNA. This addition results in the DIG label and Ab interacting, causing a larger complex to form and visually causing an upward band shift in the gel. ImageJ software (41) was used to determine labelling efficiency, and efficiency varied significantly. The average efficiency was 30%. The best labelling was of the SBV 3′ UTR at ~53% labelled (**Figure 4.2B**). The most inefficient labelling was seen from the SBV 5′ Scrambled UTR, at ~18% labelled (**Figure 4.2.A**). The WT SBV 5′ UTR and the Scrambled 3′ UTR were similar at around ~24% labelled.

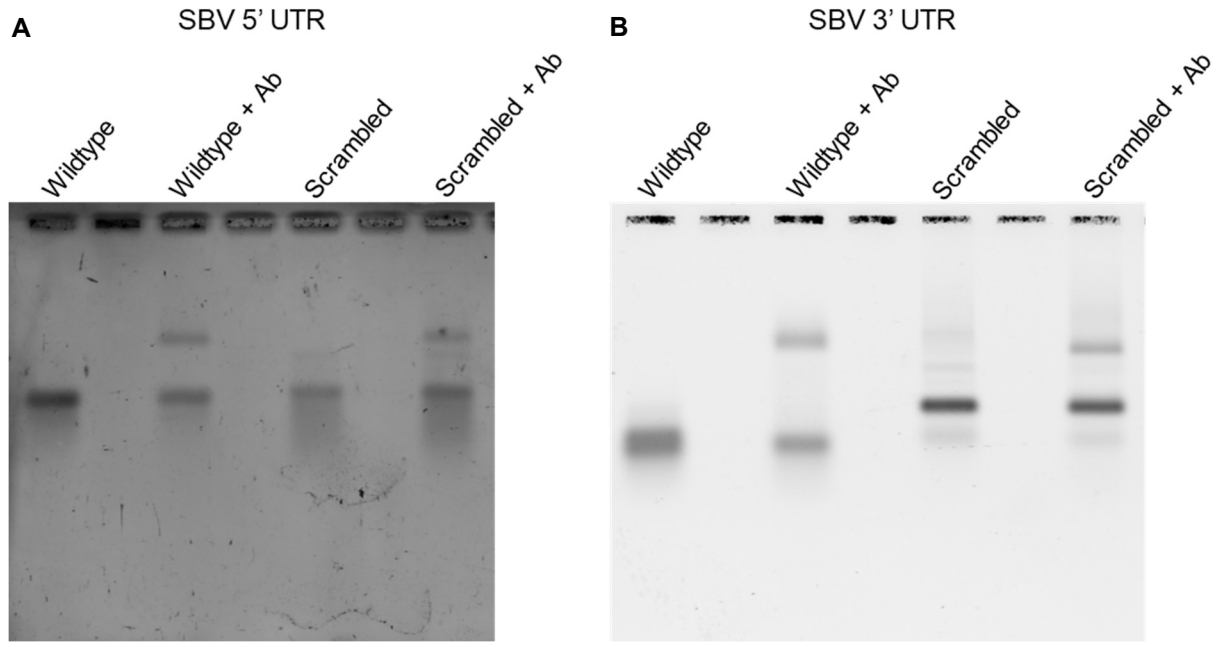

Figure 4.2. Electrophoretic mobility shift assay (EMSA) verifying successful DIG-labelling of the SBV UTRs. (**A**) SBV 5′ wildtype and Scrambled UTRs. (**B**) SBV 3′ wildtype and Scrambled UTRs. 500 nM of RNA was used with a 5 μM concentration of monoclonal mouse anti-digoxin antibody (Ab) (Jackson Immunoresearch, USA). Agarose gels (2%) were run at 100 V for 30 minutes in 1x TBE.

4.4.3 Potential RNA-binding proteins revealed through the SBV 5′ and 3′ UTR pull-down assays

Total proteins obtained from MS were filtered to exclude overlapping proteins found with the Scrambled UTRs and the negative control samples. Exceptions include select proteins that experienced a single hit in the Scrambled UTR pull-downs but a majority hit in WT UTR pull-downs. The final list of high-hit proteins (HHPs) (**Table 4.1**) was chosen based on hits with high MS scores, presence in multiple replicates, and biological relevancy.

Table 4.1. Mass spectrometry (MS) high-hit proteins (HHPs). Proteins are *Apis mellifera* specific using the *A. mellifera* (Honey bee) Uniprot data bank (UP000005203).

RNA	Protein Name	Average MS Score	Accession Number	Gene
SBV 5′ UTR	Vitellogenin*	54.90	A0A3S9VN34 A0A023W4D5 A0A023W5R1 G5D445 G5D319	Vg
	Myosin heavy chain, muscle isoform X32	41.39	A0A7M7IIK8	LOC409843
SBV 3′ UTR	Vitellogenin*	9.24	Q868N5 A0A023W515	Vg
	Paramyosin, long form	12.16	A0A7M7L7D3	LOC409787
	2-oxoglutarate dehydrogenase, mitochondrial	9.78	A0A7M7MPY0	LOC408286

*Multiple protein fragment hits were found, and the related accession numbers are noted.

The total protein hits (TPHs) were analyzed with the STRING database to map out protein-protein interactions and functional relationships (42). STRING integrates data from multiple biological databases, and from inputted proteins, it creates a network of functional associations (42). These associations are based on direct physical interactions and indirect functional connections. Each interaction is assigned a confidence score between zero and one based on the strength of the supporting evidence. The STRING network for the TPHs from the SBV 5′ UTR pull-down is shown in **Figure 4.3**. They are organized into three clusters (C) based on similar biological processes and molecular functions. CI (purple) is a large group of proteins involved in different metabolic processes, including oxidative phosphorylation, the tricarboxylic acid (TCA) cycle, and starch and sucrose metabolism. CII (green) is connected to CI and groups proteins involved in genetic information processing and includes molecular chaperones from the heat shock protein 70 family. Lastly, CIII (light blue) groups membrane trafficking proteins involved in muscle contraction. This cluster includes another HHP, myosin heavy chain (MHC), muscle

isoform X32 (A0A088AJE3). Other TPHs had no known network interactions, and another HHP is categorized here: vitellogenin (Vg).

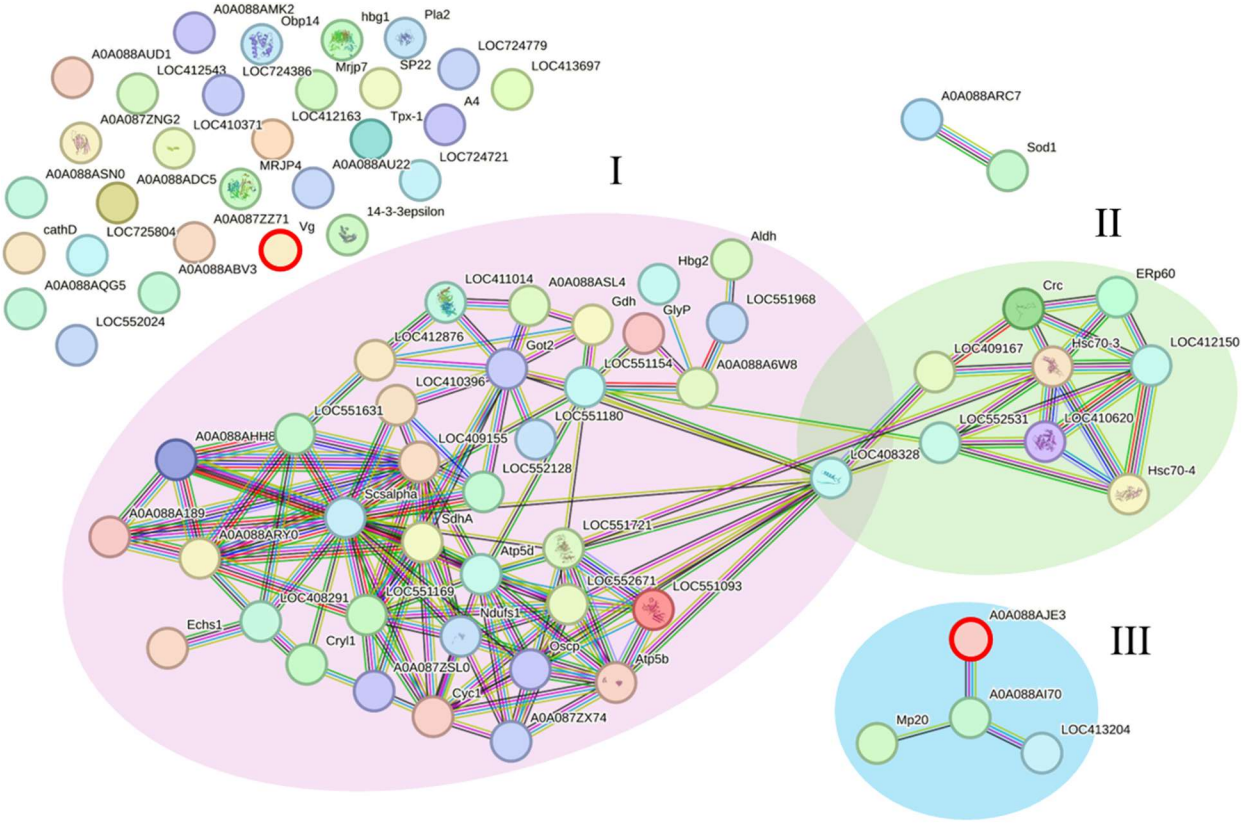

Figure 4.3. STRING network of potential protein-protein interactions of immunoprecipitated proteins associated with the SBV 5′ UTR. Each protein is represented by a coloured node which contains a known or predicted three-dimensional structure. Known interactions are depicted by the following lines: (--) from curated databases and (--) experimentally determined. Predicted interactions are depicted by lines: (--) from gene neighbourhood, (--) gene fusions, and (--) gene co-occurrence. Other interactions are depicted by lines: (--) textmining, (--) co-expression, and (--) protein homology. Clusters (C) are as follows: CI (purple) groups proteins involved in various metabolism processes; CII (green) groups proteins involved in genetic information processing; and CIII (light blue) groups proteins involved in membrane trafficking. Nodes circled in red are high-hit proteins of interest.

Figure 4.4 visualizes two distinct and unconnected clusters of potential RBPs pulled down with the SBV 3′ UTR. CI (green) includes four proteins involved in genetic information processing, including ribosomal proteins (Rp) and histone H3. CII (light blue) is a pair of

myosin-containing proteins, and this cluster has one HHP: paramyosin (PRM), long-form (A0A087ZW19). Like previously, there are also TPHs with no known interactions in the network, containing two HHPs: 2-oxoglutarate dehydrogenase (OGDH) (A0A088AHH8) and Vg, like the SBV 5′ UTR.

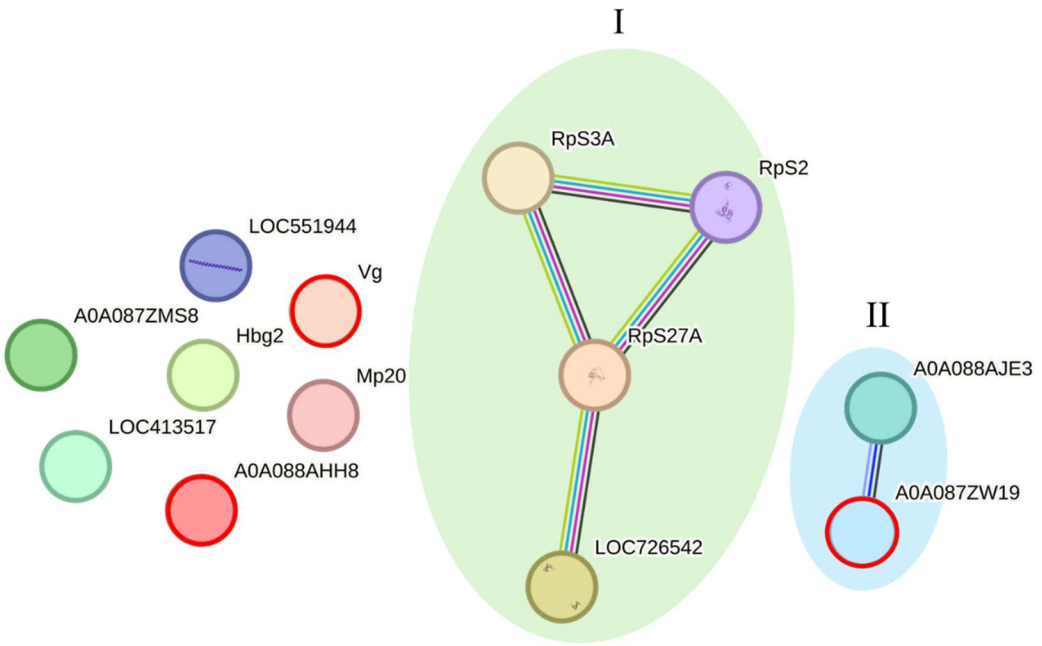

Figure 4.4. STRING network of potential protein-protein interactions of immunoprecipitated proteins associated with the SBV 3′ UTR. Each protein is represented by a coloured node which contains a known or predicted three-dimensional structure. Known interactions are depicted by the following lines: (--) from curated databases and (--) experimentally determined. Predicted interactions are depicted by lines: (--) from gene neighbourhood, (--) gene fusions, and (--) gene co-occurrence. Other interactions are depicted by lines: (--) textmining, (--) co-expression, and (--) protein homology. Clusters are as follows: CI (green) groups proteins involved in genetic information processing, and CII (light blue) groups myosin-containing proteins. Nodes circled in red are high-hit proteins of interest.

4.4.4 BlastKOALA analysis of total protein hits from the SBV 5′ and 3′ UTR pull-down assays

BlastKOALA (43) assigned KEGG orthology terms to the TPHs from the SBV 5′ and 3′ UTR pull-down assays. This tool takes input query amino acid sequences and functionally

annotates them using the KEGG database (43). It allows for the characterization of gene function and pathway analysis. Also, the incorporated Blast tool helps study any proteins that do not have direct annotations available, as it finds homologous sequences to help annotate the functions. The SBV 5′ UTR had 83 inputted entries into BlastKOALA, resulting in 62 entries being annotated (74.7%) (**Figure 4.5A**). Of these annotated entries, 64.5% are involved in carbohydrate metabolism, energy metabolism, lipid metabolism, and other metabolic pathways. An additional 24.2% are involved in genetic and environmental information processing, including transcription and signal transduction. Also, 8.1% are involved in cellular processes, including transport, catabolism, cell motility, and cell growth and death. The remaining 3.2% are involved in human diseases (including viral infectious diseases) and organismal systems (including the immune system). The SBV 3′ UTR had a total of 19 entries; however, only 10 were annotated (52.6%) (**Figure 4.5B**). When examining the annotated TPHs from SBV 3′ UTR, 50% of annotated entries involve genetic and environmental information processing, including translation and signal transduction. Additionally, 30% are involved in carbohydrate metabolism, and the final 20% are involved in signalling and cellular processes, such as transport, catabolism, and cell motility.

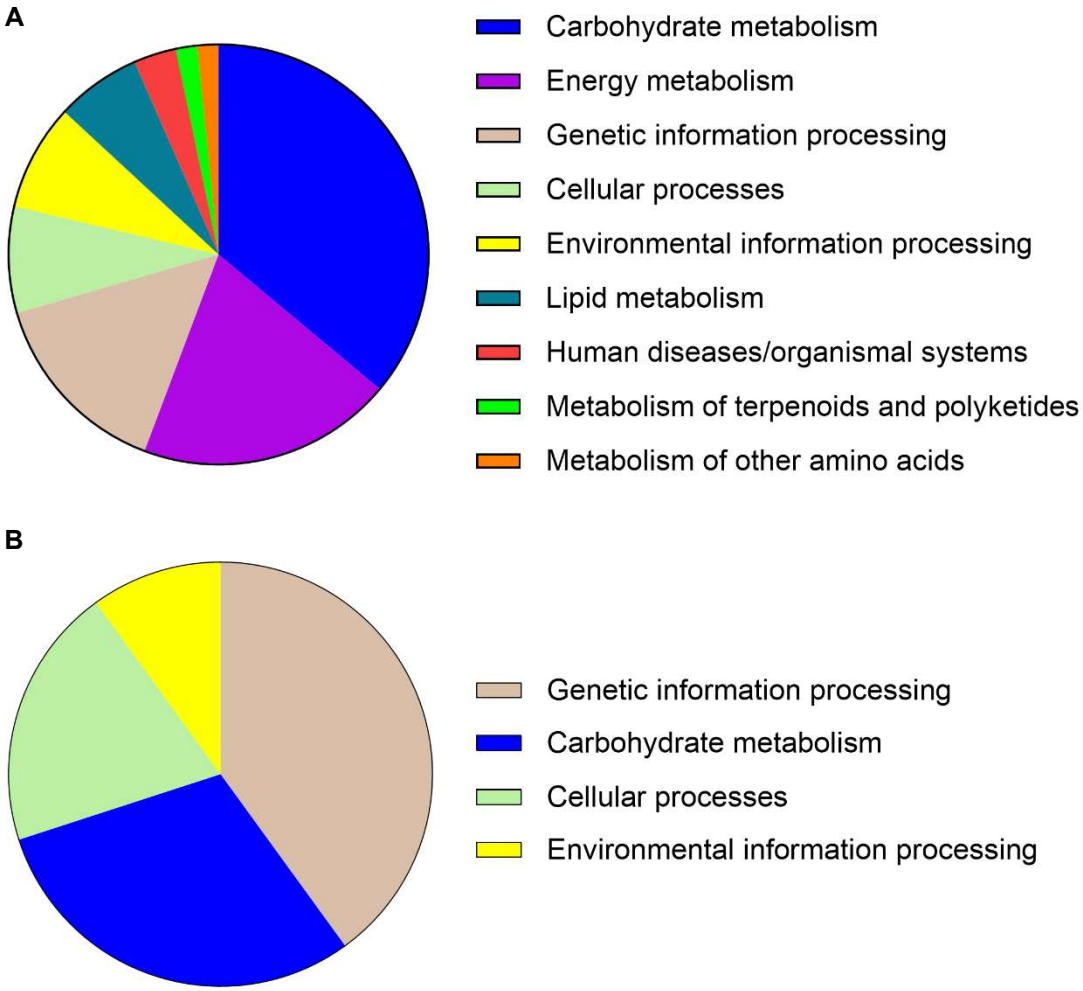

Figure 4.5. BlastKOALA analysis of total protein hits (TPHs) from the SBV UTR pull-down assays. (**A**) SBV 5′ UTR entries, where 74.7% were annotated from 83 entries. Most TPHs are involved in metabolic pathways, including carbohydrate (blue), energy (purple), lipid (cyan), terpenoids and polyketides (green), and other amino acid metabolism (orange). (**B**) SBV 3′ UTR entries, where 52.6% were annotated from 19 entries. Most TPHs are involved in carbohydrate metabolism (blue) or genetic information processing (tan).

4.5 Discussion

UTRs have many essential functions in the viral life cycle. Most of these roles are mediated by host cellular factors and viral non-structural proteins that a virus interacts with (15). The family of picornaviruses have been found to interact with an array of host cellular factors that aid in translation initiation and other processes (16). While extensive research has been completed for picornaviruses, no experimental studies have been performed to determine RBPs important to the Iflavirus life cycle. Since studies have demonstrated that some Iflaviruses utilize an IRES element in their 5′ UTR (27-30), we hypothesized that this region may interact with eIFs and ITAFs. Additionally, we believed that the UTRs would interact with proteins involved in insect immunity, such as the honey bee antimicrobial peptide apidaecins, abaecins, hymenoptaecins, and defensins (35). Uncovering virus-host interaction is vital for understanding the viral life cycle and creating a basis for future therapeutics.

The SBV 5′ and 3′ UTRs and their Scrambled counterparts were first *in vitro* transcribed and purified using SEC to generate homogenous, unaggregated RNA for use in DIG-labelling reactions, as seen in **Figure 4.1**. The SBV 5′ UTR and Scrambled 5′ UTR purification results showed single, prominent peaks for both RNA (**Figure 4.1.A**). The Scrambled 5′ UTR was eluted earlier, and even though both WT and Scrambled UTRs are the same size, this illustrated that different RNA conformations were being formed, which was expected based on the different secondary structures being formed between each RNA (not shown). Furthermore, the SBV 3′ UTR and Scrambled 3′ UTR purification illustrated smaller peaks with relatively pure RNA (**Figure 4.1.B**). The Scrambled 3′ UTR had degradation present that eluted later; therefore, these were avoided for downstream labelling reactions. One IVT reaction was enough to generate an appropriate concentration of RNA for each DIG-labelling reaction.

Each UTR was labelled with the DIG linker to prepare for the pull-down assays. RNA labelling was performed using two protocols, each with a different efficiency. The WT and Scrambled SBV 5′ UTRs were labelled by conjugating the DIG-NHS ester to the 5′ phosphate group of the RNA using the crosslinker EDC and imidazole (44). The WT and Scrambled SBV 3′ UTRs were DIG-labelled using a more commonly used protocol, T4 RNA ligation (45). The T4 RNA ligation was the most efficient labelling technique, with the SBV 3′ UTR and Scrambled 3′ UTR labelled at around 53% and 24%, respectively (**Figure 4.2B**). Unfortunately, the 5′-modified RNA labelled with the DIG-NHS ester was not as efficient, with the SBV 5′ UTR and Scrambled 5′ UTR labelled at around 24% and 18%, respectively (**Figure 4.2A**). While the labelling efficiency was low, we were confident that the amount of DIG-labelled UTR would be sufficient for the pull-down assays. Future pull-down assays should explore alternative, more efficient protocols for RNA labelling or consider using aptamer modifications (32).

Protein hits from each pull-down assay were filtered to obtain a list of TPHs, and STRING and BlastKOALA were used to characterize the functional relationships of the proteins. STRING analysis helped cluster proteins to visualize the functional roles of potential RBPs. Some TPHs for each UTR were intriguing; however, they were disregarded, as they only occurred in one replicate and could not be analyzed confidently as an RBP. The SBV 5′ UTR interacted with an extensive list of proteins (**Figure 4.3**). As seen in CI, most protein hits were involved in a range of metabolic activities, further outlined in the BlastKOALA results (**Figure 4.5A**). Also, many protein hits had no known interactions. This large group contained one of the HHPs chosen based on a high MS score and presence in more than one replicate, Vg (**Table 4.1**). This protein was a repeated hit from the SBV 5′ and SBV 3′ UTR pull-down assays and was found as full-length Vg and Vg fragments.

Vg is a large glycolipophosphoprotein found across all oviparous vertebrates and invertebrates (46). Its most well-known function is to aid reproduction as a precursor of egg yolk (47). However, many additional roles have been studied, including oxidative stress resistance, social organization, regulation of hormone dynamics, and immunity (48-52). Studies have shown that Vg can facilitate the transport of plant-infecting viruses across the insect midgut and hemolymph (53,54). Hemocyte-produced Vg from the small brown planthopper (*Laodelphax striatellus* F.) was found to bind to the Rice stripe virus *in vivo* (54). The virus was then capable of completing vertical transmission through the transportation of Vg into developing oocytes. Additionally, whitefly (*Bemisia tabaci* G.) Vg can form a complex with tomato yellow leaf curl virus, which gets internalized into midgut epithelial cells for intracellular transport (53). Furthermore, a study by Garcia et al. (55) has speculated that the infectious pancreatic necrosis virus in Atlantic salmon (*Salmo salar* L.) has developed a strategy for vertical transmission, where the virus becomes coated with Vg and can be transported intracellularly via Vg-receptors on developing oocytes. While these studies are interesting, they do not portray Vg directly binding viral RNA. However, finding Vg in multiple hits of our pull-down assays with a high MS score indicates a possible novel role for the protein.

Given the evidence of Vg being involved in immunity and vertical transmission of other viruses, it is plausible that Vg can interact with SBV. In honey bees, Vg has also been implicated in immune priming (56). Nurse bees have high levels of Vg in their fat bodies, which decreases as honey bees age and transition into foragers (50,57). Harwood et al. (56) suggest bacterial fragments may be transported with Vg, incorporated into royal jelly, and fed directly to larvae or the queen. These findings, taken together with Vgs association with viruses (53-55), suggest that

Vg may have implications in promoting SBV transmission from nurse bees to larvae or the queen. More investigation is required to determine Vg's possible RNA-binding capacity.

The other HHP result for the SBV 5′ UTR was MHC muscle isoform X32 found in the smaller CIII of proteins involved in membrane trafficking (**Figure 4.3**). Myosins are a family of motor proteins that aid in muscle contraction and other movements of non-muscle cells, such as cytokinesis, vesicle transport, and phagocytosis (58). Beyond these functions, studies have demonstrated that myosin can interact with viruses in many different capacities (59). Depending on the context, myosin can either aid or hinder various stages of the viral life cycle. Alongside this, myosin proteins have been found to have RNA-binding activity, which is considered a noncanonical role for motor proteins (60). One example of this dual function is the myosin motor Myosin Va, which has been found to interact with the picornavirus Rhinovirus B in the early stages of viral infection and RNA replication (61). Myosin Va was colocalized with Rhinovirus B RNA and proteins in structures resembling phagocytic cups and may contribute to the localization of the viral RNA genome to replication sites (61). Given that MHC was pulled down with the SBV 5′ UTR and had a high MS score, it is possible that myosin plays a similar role in SBV infection. As with Vg, further investigation will be required to fully determine the RNA-binding capabilities of MHC to the SBV 5′ UTR.

The SBV 3′ UTR bound to a smaller list of proteins, as seen in **Figure 4.4**. Most protein hits did not have any known interactions with one another. A few of the proteins with no known interactions are involved in metabolism (**Figure 4.5B**), as further outlined by one of the HHPs with a moderate MS score: 2-oxoglutarate dehydrogenase (OGDH) (**Table 4.1**). OGDH is part of the multi-enzyme complex known as the oxoglutarate dehydrogenase complex, which is responsible for the oxidative decarboxylation of 2-oxoglutarate to succinyl-coenzyme A during

the TCA cycle (62). Recent reports have shown that many metabolic enzymes can 'moonlight' as RBPs, a traditionally unconventional function for these enzymes (63,64). Viruses can hijack metabolic enzymes to generate the metabolites required for viral infection (65). For example, fatty acid synthase has been characterized as a viral replication regulator and can bind both viral and cellular RNA (66). Similarly, other TCA cycle proteins, such as glutamate dehydrogenase and NAD^+-dependent isocitrate dehydrogenase, have been found to possess RNA-binding properties (67). Although OGDH has not yet been shown to bind RNA, its role in viral infection has been investigated. A study by Liu et al. (68) revealed that OGDH is proviral and that an OGDH knockdown significantly inhibited viral replication. These studies highlight the possibility that OGDH may act as a noncanonical RBP, potentially interacting with viral RNAs, such as the SBV 3′ UTR, to modulate viral replication. Given the increasing number of metabolic enzymes being recognized as RBPs, there is potential that OGDH could be recruited by SBV to facilitate replication. Future studies will need to be completed to confirm RNA-binding activity and determine whether OGDH is capable of moonlighting as an RBP.

The final HHP found through the SBV 3′ UTR pull-down assay was paramyosin (PRM), another cytoskeletal protein (**Table 4.1**). PRM is a protein that provides structural support to the thick filaments of invertebrate muscles (69). In *Drosophila melanogaster*, PRM has a structure similar to the MHC rod tail and forms rod-like dimers (70). It forms the core of the thick filament onto which myosin packs around the core (71). However, unlike myosin, there is limited information regarding PRM's capacity to bind RNA or its involvement in viral infections. A study by DeBlasio et al. (72) predicted that PRM was a high-probability candidate for interacting with the Potato leafroll virus through affinity purifications from viruliferous aphids (*Myzus persicae* S.), a known vector of the Potato leafroll virus. This suggests that PRM

may have a potential but unexplored role in the viral life cycle. Since PRM is associated with myosin, it is plausible that PRM was found in the pull-down as an association with MHC rather than a direct RBP. Given the lack of direct evidence linking PRM to RNA-binding, further studies are required to confirm this function.

4.6 Conclusions and Future Directions

This study reveals potential RBPs capable of interacting with the SBV 5′ and 3′ UTRs. The proteins hypothesized to interact with the SBV UTRs, including eIFs, ITAFs, and immunity-associated proteins, were not found in our HHPs. Since the proteins found are noncanonical RBPs, further investigation is required to verify the RNA-protein interactions. This will include repeating the pull-down assays to confirm the likelihood of these RBPs interacting with the UTRs and ensure other potential RBPs, like the proteins hypothesized, were not missed. Ideally, honey bee proteins for the pull-down assays would be obtained via cell culturing; however, maintaining an *A. mellifera* cell line has proven difficult (73). We anticipate future developments of the cell line to allow for *in vivo* pull-down assays, thereby making the use of an RNA Mango aptamer possible. The RNA Mango aptamer is an RNA tag that can be added directly onto an RNA of interest, eliminating RNA-labelling steps (74). It binds a series of thiazole orange (fluorophore) derivatives with nanomolar affinity and can increase fluorescence significantly. RNAs tagged with RNA Mango can be transfected and transcribed *in vivo*, allowing for the immunoprecipitation of RBPs in the cell (75). Using this technique for future pull-down assays and comparing results to the RBPs pulled down in this study would create strong evidence for the proteins found. The pull-down assays will also be repeated with larvae rather than adult honey bees to allow for an in-depth comparison between developmental states and SBV-host interactions.

Once RBPs are confirmed with high confidence through subsequent experiments, the UTRs and their associated HHP will be subjected to EMSAs, microscale thermophoresis, and isothermal titration calorimetry. This combination of techniques will allow for the qualitative and quantitative study of the RNA-protein binding interactions (76-78). Also, this provides the

opportunity to investigate uncharacterized honey bee proteins. The structural features of these proteins and their RNA-protein complexes will be determined using small-angle X-ray scattering (SAXS) and cryo-electron microscopy (79). Overall, this study provides insight into the potential viral RNA-protein interactions in honey bees and creates a basis for multiple future studies.

4.7 References

1. White, G.F. (1913) *Sacbrood, a disease of bees*. US Department of Agriculture, Bureau of Entomology, Washington, DC, USA.
2. Wei, R., Cao, L., Feng, Y., Chen, Y., Chen, G. and Zheng, H. (2022) Sacbrood virus: a growing threat to honeybees and wild pollinators. *Viruses*, **14**, 1871.
3. National Bee Diagnostic Centre. (2017) Canadian National Honey Bee Health Survey, 2017 Report. 1-33.
4. Ball, B.V. and Bailey, L. (1997) In Morse, R. A. and Flottum, K. (eds.), *Honey Bee Pests, Predators, & Disease*. The A. I. Root Company, Medina, OH, USA, pp. 11-31.
5. Bailey, L. (1975) Recent research on honeybee viruses. *Bee World*, **56**, 55-64.
6. Chen, Y.P. and Siede, R. (2007) Honey bee viruses. *Adv Virus Res*, **70**, 33-80.
7. Borba, R.S., Hoover, S.E., Currie, R.W., Giovenazzo, P., Guarna, M.M., Foster, L.J., Zayed, A. and Pernal, S.F. (2022) Phenomic analysis of the honey bee pathogen-web and its dynamics on colony productivity, health and social immunity behaviors. *PLoS One*, **17**, e0263273.
8. Le Gall, O., Christian, P., Fauquet, C.M., King, A.M., Knowles, N.J., Nakashima, N., Stanway, G. and Gorbalenya, A.E. (2008) *Picornavirales*, a proposed order of positive-sense single-stranded RNA viruses with a pseudo-T = 3 virion architecture. *Arch Virol*, **153**, 715-727.
9. Valles, S.M., Chen, Y., Firth, A.E., Guerin, D.M.A., Hashimoto, Y., Herrero, S., de Miranda, J.R., Ryabov, E. and ICTV Report Consortium. (2017) ICTV virus taxonomy profile: *Iflaviridae*. *J Gen Virol*, **98**, 527-528.
10. Li, J., Wang, T., Evans, J.D., Rose, R., Zhao, Y., Li, Z., Li, J., Huang, S., Heerman, M., Rodriguez-Garcia, C. *et al.* (2019) The phylogeny and pathogenesis of Sacbrood virus (SBV) infection in European honey bees, *Apis mellifera*. *Viruses*, **11**.
11. Chiu, W.-W., Kinney, R.M. and Dreher, T.W. (2005) Control of translation by the 5′- and 3′-terminal regions of the dengue virus genome. *Journal of Virology*, **79**, 8303-8315.
12. Alvarez, D.E., De Lella Ezcurra, A.L., Fucito, S. and Gamarnik, A.V. (2005) Role of RNA structures present at the 3′UTR of dengue virus on translation, RNA synthesis, and viral replication. *Virology*, **339**, 200-212.
13. Sokoloski, K.J., Dickson, A.M., Chaskey, E.L., Garneau, N.L., Wilusz, C.J. and Wilusz, J. (2010) Sindbis virus usurps the cellular HuR protein to stabilize its transcripts and promote productive infections in mammalian and mosquito cells. *Cell Host Microbe*, **8**, 196-207.
14. Xie, X., Zou, J., Zhang, X., Zhou, Y., Routh, A.L., Kang, C., Popov, V.L., Chen, X., Wang, Q.-Y., Dong, H. *et al.* (2019) Dengue NS2A protein orchestrates virus assembly. *Cell Host & Microbe*, **26**, 606-622.e608.
15. Vidalain, P.O. and Tangy, F. (2010) Virus-host protein interactions in RNA viruses. *Microbes Infect*, **12**, 1134-1143.
16. Lin, J.Y., Chen, T.C., Weng, K.F., Chang, S.C., Chen, L.L. and Shih, S.R. (2009) Viral and host proteins involved in picornavirus life cycle. *J Biomed Sci*, **16**, 103.
17. Abdullah, S.W., Wu, J., Wang, X., Guo, H. and Sun, S. (2023) Advances and breakthroughs in IRES-directed translation and replication of picornaviruses. *mBio*, **14**.
18. Sweeney, T.R., Abaeva, I.S., Pestova, T.V. and Hellen, C.U.T. (2014) The mechanism of translation initiation on Type 1 picornavirus IRESs. *The EMBO Journal*, **33**, 76-92.

19. Cheung, P., Lim, T., Yuan, J., Zhang, M., Chau, D., McManus, B. and Yang, D. (2007) Specific interaction of HeLa cell proteins with coxsackievirus B3 3′UTR: La autoantigen binds the 3′ and 5′UTR independently of the poly(A) tail. *Cell Microbiol*, **9**, 1705-1715.
20. Ray, P.S. and Das, S. (2002) La autoantigen is required for the internal ribosome entry site-mediated translation of Coxsackievirus B3 RNA. *Nucleic Acids Res*, **30**, 4500-4508.
21. Bhattacharyya, S. and Das, S. (2005) Mapping of secondary structure of the spacer region within the 5′-untranslated region of the coxsackievirus B3 RNA: possible role of an apical GAGA loop in binding La protein and influencing internal initiation of translation. *Virus Research*, **108**, 89-100.
22. Kolupaeva, V.G., Hellen, C.U.T. and Shatsky, I.N. (1996) Structural analysis of the interaction of the pyrimidine tract-binding protein with the internal ribosomal entry site of encephalomyocarditis virus and foot-and-mouth disease virus RNAs. *RNA*, **2**, 1199-1212.
23. Kolupaeva, V.G., Pestova, T.V., Hellen, C.U.T. and Shatsky, I.N. (1998) Translation eukaryotic initiation factor 4G recognizes a specific structural element within the internal ribosome entry site of encephalomyocarditis virus RNA. *Journal of Biological Chemistry*, **273**, 18599-18604.
24. Todd, S., Nguyen, J.H.C. and Semler, B.L. (1995) RNA-protein interactions directed by the 3′ end of human rhinovirus genomic RNA. *Journal of Virology*, **69**, 3605-3614.
25. Mellits, K.H., Meredith, J.M., Rohll, J.B., Evans, D.J. and Almond, J.W. (1998) Binding of a cellular factor to the 3′ untranslated region of the RNA genomes of entero- and rhinoviruses plays a role in virus replication. *Journal of General Virology*, **79**, 1715-1723.
26. Waggoner, S. and Sarnow, P. (1998) Viral ribonucleoprotein complex formation and nucleolar-cytoplasmic relocalization of nucleolin in poliovirus-infected cells. *Journal of Virology*, **72**, 6699-6709.
27. Ongus, J.R., Roode, E.C., Pleij, C.W.A., Vlak, J.M. and van Oers, M.M. (2006) The 5′ non-translated region of *Varroa destructor* virus 1 (genus *Iflavirus*): structure prediction and IRES activity in *Lymantria dispar* cells. *J Gen Virol*, **87**, 3397-3407.
28. Lu, J., Hu, Y., Hu, L., Zong, S., Cai, D., Wang, J., Yu, H. and Zhang, J. (2007) *Ectropis obliqua* picorna-like virus IRES-driven internal initiation of translation in cell systems derived from different origins. *J Gen Virol*, **88**, 2834-2838.
29. Wu, T.Y., Wu, C.Y., Chen, Y.J., Chen, C.Y. and Wang, C.H. (2007) The 5′ untranslated region of *Perina nuda* virus (PnV) possesses a strong internal translation activity in baculovirus-infected insect cells. *FEBS Lett*, **581**, 3120-3126.
30. Li, M., Man, N., Qiu, H., Cai, S., He, X., He, X. and Lu, X. (2012) Detection of an internal translation activity in the 5′ region of *Bombyx mori* infectious flacherie virus. *Appl Microbiol Biotechnol*, **95**, 697-705.
31. Ramanathan, M., Porter, D.F. and Khavari, P.A. (2019) Methods to study RNA-protein interactions. *Nat Methods*, **16**, 225-234.
32. Gemmill, D., D'Souza, S., Meier-Stephenson, V. and Patel, T.R. (2020) Current approaches for RNA-labelling to identify RNA-binding proteins. *Biochem Cell Biol*, **98**, 31-41.
33. McCreery, T. (1997) Digoxigenin labeling. *Molecular Biotechnology*, **7**, 121-124.
34. Filbin, M.E. and Kieft, J.S. (2009) Toward a structural understanding of IRES RNA function. *Curr Opin Struct Biol*, **19**, 267-276.

35. Feng, M., Fei, S., Xia, J., Labropoulou, V., Swevers, L. and Sun, J. (2020) Antimicrobial peptides as potential antiviral factors in insect antiviral immune response. *Front Immunol*, **11**, 2030.
36. Brutscher, L.M., Daughenbaugh, K.F. and Flenniken, M.L. (2015) Antiviral defense mechanisms in honey bees. *Curr Opin Insect Sci*, **10**, 71-82.
37. Stothard, P. (2000) The Sequence Manipulation Suite: JavaScript programs for analyzing and formatting protein and DNA sequences. *Biotechniques*, **28**, 1102-1104.
38. Gruber, A.R., Lorenz, R., Bernhart, S.H., Neubock, R. and Hofacker, I.L. (2008) The Vienna RNA websuite. *Nucleic Acids Res*, **36**, W70-74.
39. Lorenz, R., Bernhart, S.H., Höner zu Siederdissen, C., Tafer, H., Flamm, C., Stadler, P.F. and Hofacker, I.L. (2011) ViennaRNA package 2.0. *Algorithms for Molecular Biology*, **6**.
40. Mrozowich, T., Park, S.M., Waldl, M., Henrickson, A., Tersteeg, S., Nelson, C.R., De Klerk, A., Demeler, B., Hofacker, I.L., Wolfinger, M.T. *et al.* (2023) Investigating RNA-RNA interactions through computational and biophysical analysis. *Nucleic Acids Res*, **51**, 4588-4601.
41. Schneider, C., Rasband, W. and Eliceiri, K. (2012) NIH Image to ImageJ: 25 years of image analysis. *Nat Methods*, **9**, 671-675.
42. Szklarczyk, D., Kirsch, R., Koutrouli, M., Nastou, K., Mehryary, F., Hachilif, R., Gable, A.L., Fang, T., Doncheva, Nadezhda T., Pyysalo, S. *et al.* (2023) The STRING database in 2023: protein–protein association networks and functional enrichment analyses for any sequenced genome of interest. *Nucleic Acids Research*, **51**, D638-D646.
43. Kanehisa, M., Sato, Y. and Morishima, K. (2016) BlastKOALA and GhostKOALA: KEGG tools for functional characterization of genome and metagenome sequences. *Journal of Molecular Biology*, **428**, 726-731.
44. Hermanson, G.T. (2008) *Bioconjugate Techniques*. 2 ed. Academic Press, San Diego, USA.
45. England, T.E., Bruce, A.G. and Uhlenbeck, O.C. (1980) Specific labeling of 3′ termini of RNA with T4 RNA ligase. *Methods Enzymol*, **65**, 65-74.
46. Biscotti, M.A., Barucca, M., Carducci, F., Canapa, A. and Costantini, M. (2018) New perspectives on the evolutionary history of vitellogenin gene family in vertebrates. *Genome Biology and Evolution*, **10**, 2709-2715.
47. Raikhel, A.S. and Dhadialla, T.S. (1992) Accumulation of yolk proteins in insect oocytes. *Annu Rev Entomol*, **37**, 217-251.
48. Havukainen, H., Münch, D., Baumann, A., Zhong, S., Halskau, Ø., Krogsgaard, M. and Amdam, G.V. (2013) Vitellogenin recognizes cell damage through membrane binding and shields living cells from reactive oxygen species. *Journal of Biological Chemistry*, **288**, 28369-28381.
49. Amdam, G.V., Norberg, K., Hagen, A. and Omholt, S.W. (2003) Social exploitation of vitellogenin. *PNAS*, **100**, 1799-1802.
50. Nelson, C.M., Ihle, K.E., Fondrk, M.K., Page, R.E. and Amdam, G.V. (2007) The gene vitellogenin has multiple coordinating effects on social organization. *PLoS Biol*, **5**, e62.
51. Guidugli, K.R., Nascimento, A.M., Amdam, G.V., Barchuk, A.R., Omholt, S., Simões, Z.L.P. and Hartfelder, K. (2005) Vitellogenin regulates hormonal dynamics in the worker caste of a eusocial insect. *FEBS Letters*, **579**, 4961-4965.
52. Salmela, H. and Sundström, L. (2017) Vitellogenin in inflammation and immunity in social insects. *Inflammation and Cell Signaling*, **4**.

53. He, Y., Wang, Y., Yin, T., Cuellar, W.J., Liu, S.S. and Wang, X. (2021) Gut-expressed vitellogenin facilitates the movement of a plant virus across the midgut wall in its insect vector. *mSystems*, **6**.
54. Huo, Y., Yu, Y., Liu, Q., Liu, D., Zhang, M., Liang, J., Chen, X., Zhang, L. and Fang, R. (2019) Rice stripe virus hitchhikes the vector insect vitellogenin ligand-receptor pathway for ovary entry. *Philos Trans R Soc Lond B Biol Sci*, **374**, 20180312.
55. Garcia, J., Munro, E.S., Monte, M.M., Fourrier, M.C.S., Whitelaw, J., Smail, D.A. and Ellis, A.E. (2010) Atlantic salmon (*Salmo salar* L.) serum vitellogenin neutralises infectivity of infectious pancreatic necrosis virus (IPNV). *Fish & Shellfish Immunology*, **29**, 293-297.
56. Harwood, G., Amdam, G. and Freitak, D. (2019) The role of Vitellogenin in the transfer of immune elicitors from gut to hypopharyngeal glands in honey bees (*Apis mellifera*). *J Insect Physiol*, **112**, 90-100.
57. Amdam, G.V. and Omholt, S.W. (2003) The hive bee to forager transition in honeybee colonies: the double repressor hypothesis. *J Theor Biol*, **223**, 451-464.
58. Cooper, G.M. (2000) In Sunderland, M. A. (ed.), *The Cell: A Molecular Approach*. 2 ed. Sinauer Associates.
59. Matozo, T., Kogachi, L. and de Alencar, B.C. (2022) Myosin motors on the pathway of viral infections. *Cytoskeleton (Hoboken)*, **79**, 41-63.
60. Iselin, L., Palmalux, N., Kamel, W., Simmonds, P., Mohammed, S. and Castello, A. (2022) Uncovering viral RNA-host cell interactions on a proteome-wide scale. *Trends Biochem Sci*, **47**, 23-38.
61. Real-Hohn, A., Provance, D.W., Jr., Goncalves, R.B., Denani, C.B., de Oliveira, A.C., Salerno, V.P. and Oliveira Gomes, A.M. (2017) Impairing the function of MLCK, myosin Va or myosin Vb disrupts Rhinovirus B14 replication. *Sci Rep*, **7**, 17153.
62. Rex Sheu, K.-F. and Blass, J.P. (1999) The α-ketoglutarate dehydrogenase complex. *Annals of the New York Academy of Sciences*, **893**, 61-78.
63. Castello, A., Hentze, M.W. and Preiss, T. (2015) Metabolic enzymes enjoying new partnerships as RNA-binding proteins. *Trends Endocrinol Metab*, **26**, 746-757.
64. Balcerak, A., Trebinska-Stryjewska, A., Konopinski, R., Wakula, M. and Grzybowska, E.A. (2019) RNA-protein interactions: disorder, moonlighting and junk contribute to eukaryotic complexity. *Open Biol*, **9**, 190096.
65. Lisy, S., Rothamel, K. and Ascano, M. (2021) RNA binding proteins as pioneer determinants of infection: protective, proviral, or both? *Viruses*, **13**.
66. Kim, B., Arcos, S., Rothamel, K., Jian, J., Rose, K.L., McDonald, W.H., Bian, Y., Reasoner, S., Barrows, N.J., Bradrick, S. *et al.* (2020) Discovery of widespread host protein interactions with the pre-replicated genome of CHIKV using VIR-CLASP. *Molecular Cell*, **78**, 624-640.e627.
67. Cieśla, J. (2006) Metabolic enzymes that bind RNA: yet another level of cellular regulatory network? *Acta Biochimica Polonica*, **53**, 11-32.
68. Liu, Y., You, Y., Lu, Z., Yang, J., Li, P., Liu, L., Xu, H., Niu, Y. and Cao, X. (2019) N^6-methyladenosine RNA modification-mediated cellular metabolism rewiring inhibits viral replication. *Science*, **365**, 1171-1176.
69. Szent-Györgyi, A.G., Cohen, C. and Kendrick-Jones, J. (1971) Paramyosin and the filaments of molluscan "catch" muscles: II. Native filaments: Isolation and characterization. *Journal of Molecular Biology*, **56**, 239-248.

70. Cervera, M., Arredondo, J.J. and Ferreres, R.M. (2006), *Nature's Versatile Engine: Insect Flight Muscle Inside and Out*. Molecular Biology Intelligence Unit, Springer, Boston, MA.
71. Miller, M.S., Tanner, B.C.W., Nyland, L.R. and Vigoreaux, J.O. (2010) Comparative biomechanics of thick filaments and thin filaments with functional consequences for muscle contraction. *BioMed Research International*, **2010**, 473423.
72. DeBlasio, S.L., Wilson, J.R., Tamborindeguy, C., Johnson, R.S., Pinheiro, P.V., MacCoss, M.J., Gray, S.M. and Heck, M. (2021) Affinity purification-mass spectrometry identifies a novel interaction between a polerovirus and a conserved innate immunity aphid protein that regulates transmission efficiency. *J Proteome Res*, **20**, 3365-3387.
73. Guo, Y., Goodman, C.L., Stanley, D.W. and Bonning, B.C. (2020) Cell lines for honey bee virus research. *Viruses*, **12**, 236.
74. Dolgosheina, E.V., Jeng, S.C.Y., Panchapakesan, S.S.S., Cojocaru, R., Chen, P.S.K., Wilson, P.D., Hawkins, N., Wiggins, P.A. and Unrau, P.J. (2014) RNA Mango aptamer-fluorophore: a bright, high-affinity complex for RNA labeling and tracking. *ACS Chemical Biology*, **9**, 2412-2420.
75. Panchapakesan, S.S.S., Ferguson, M.L., Hayden, E.J., Chen, X., Hoskins, A.A. and Unrau, P.J. (2017) Ribonucleoprotein purification and characterization using RNA Mango. *RNA*, **23**, 1592-1599.
76. Hellman, L.M. and Fried, M.G. (2007) Electrophoretic mobility shift assay (EMSA) for detecting protein-nucleic acid interactions. *Nat Protoc*, **2**, 1849-1861.
77. Moon, M.H., Hilimire, T.A., Sanders, A.M. and Schneekloth, J.S., Jr. (2018) Measuring RNA-ligand interactions with microscale thermophoresis. *Biochemistry*, **57**, 4638-4643.
78. Feig, A.L. (2009) Studying RNA-RNA and RNA-protein interactions by isothermal titration calorimetry. *Methods Enzymol*, **468**, 409-422.
79. Patel, T.R., Chojnowski, G., Astha, Koul, A., McKenna, S.A. and Bujnicki, J.M. (2017) Structural studies of RNA-protein complexes: A hybrid approach involving hydrodynamics, scattering, and computational methods. *Methods*, **118-119**, 146-162.

CHAPTER 5: Conclusions

5.1 Overview

My work has explored the structural and functional characteristics of Iflavirus untranslated regions (UTRs), towards addressing a critical gap in research on these critical regions. By focusing on *Iflaviridae*, a family of viruses that has garnered much interest due to their impact on honey bees (1), this work adds to our growing understanding of the family. UTRs play essential roles in the viral life cycle through host interactions based on complex secondary and tertiary structures (2,3), but many features of the Iflavirus UTRs remain undescribed. We characterized the UTRs of the sacbrood virus (SBV) and deformed wing virus (DWV) and determined their structures and links to possible functions involving host interactions and translational control. Through the integration of multiple biophysical techniques and assays, this thesis provides foundational insights that will guide future studies.

Using a combination of small-angle X-ray scattering (SAXS) and computation modelling, we revealed high-resolution structures of the SBV UTRs (Chapter 2). The SBV 5′ UTR exhibited a unique, multi-branched loop tertiary structure, while the SBV 3′ UTR had a typical elongated structure. Given the evidence that other Iflaviruses have an internal ribosome entry site (IRES) in the 5′ UTR (4-7), we investigated whether this function was present in SBV. Using a bicistronic reporter assay system, we confirmed IRES activity in the UTR both *in vitro* and *in vivo*. Subsequently, deletion mutants on either side of the UTR helped map the minimal region required for IRES activity. These results provide the first evidence that SBV contains an IRES element, offering new insights into its structure-to-function relationship.

I extended the combination of biophysical techniques to elucidate the structure of the DWV 3′ UTR (Chapter 3). SAXS analysis allowed the determination of the low-resolution envelope structure of the UTR, revealing an asymmetrical, elongated shape. By combining the envelope with high-resolution tertiary structures, it was observed that the models followed the general shape of the envelope; however, some regions of each protruded out. This work gives insight into the 3′ UTR of DWV, providing a basis for future studies to discover the correlation of structure to function.

Lastly, I investigated the interaction between the SBV UTRs and host proteins (Chapter 4). Using RNA immunoprecipitation pull-down assays, I found a list of potential RNA-binding proteins (RBPs) interacting with the SBV 5′ and 3′ UTRs. Though many of the proteins found were noncanonical RBPs with limited evidence of RNA-binding capacity, literature reviews suggest further investigation is warranted. Vitellogenin and a myosin heavy chain protein were identified in the SBV 5′ UTR pull-down assays. Vitellogenin has a role in immunity and has been implicated in the vertical transmission of viruses (8-10). Myosin proteins have noncanonical RNA-binding activity and have been shown to interact with viruses to either aid or hinder the viral life cycle (11,12). The SBV 3′ UTR pull-down assays also revealed vitellogenin and two other unconventional proteins, including 2-oxoglutarate dehydrogenase and paramyosin. Metabolic enzymes like 2-oxoglutarate dehydrogenase have been shown to 'moonlight' as RBPs and play important roles in viral infection (13,14), and paramyosin, a cytoskeletal protein, has limited evidence of being an RBP (15). These identified proteins may play similar roles in the SBV viral life cycle; however, more investigation is required. Together, these findings lay the groundwork for understanding Iflavirus-host interactions, which has implications for developing antiviral therapeutics.

5.2 Future Directions

Discovering that the SBV 5′ UTR has an IRES element allows multiple future studies to characterize the IRES further. Additional mutational analyses will be performed to disrupt stem loops and motifs, such as the pyrimidine tract region, and determine whether these regions are critical for SBV IRES activity (16). Also, determining if host factors, including initiation factors or IRES trans-acting factors, are required for IRES activity is a crucial next step to uncovering the IRES' mechanism for translation initiation (17). This will also help classify the IRES and determine if a new classification is warranted. Additional studies include analyzing IRES activity in other cell types, including hymenopteran and *A. mellifera* cell lines, once robust protocols are available (18). Performing additional *in vivo* studies will enhance our understanding of how the mechanism of IRES-mediated translation is conserved in SBV. These future directions are just a handful of foundational studies that will lead to the characterization of this newly discovered IRES.

Orthogonal strategies can improve and build upon the biophysical characterization of the SBV and DWV UTRs. Selective 2' Hydroxyl Acylation analyzed by Primer Extension (SHAPE) will help experimentally determine the RNA secondary structure and the presence of potential pseudoknot domains, a critical component for further understanding the SBV IRES (19). Acquiring an experimental secondary structure will significantly increase the impact of the SBV and DWV SAXS structures. Additionally, comparing the experimental secondary structure with the computational predictions will help assess the accuracy of these tools. Having this workflow established will make completing the biophysical characterization of the DWV 5′ UTR much more streamlined.

As discussed previously, the potential RBPs found through the pull-down assays will be confirmed through further investigation. Repeat pull-down assays will help confirm the RBPs found in the previous assays with high confidence and ensure other potential RBPs are not overseen. We hope future *A. mellifera* cell line developments will allow *in vivo* pull-down assays using the RNA Mango aptamer (20). Using alternative methods for the pull-down assays will create a robust list of RBPs that can be investigated further. This will involve the overexpression and purification of the RBPs from insect cell lines (such as Sf9) and characterizing their RNA binding capacity. Techniques including electrophoretic mobility shift assays, microscale thermophoresis, and isothermal titration calorimetry (21-23) will determine binding affinities between RBP and UTR. Just as SAXS was utilized to characterize the structure of the UTRs, it will be employed for the RNA-protein complexes. Additional techniques, including cryo-electron microscopy, can be used to compare the results of the complex structures (24).

5.3 References

1. Beaurepaire, A., Piot, N., Doublet, V., Antunez, K., Campbell, E., Chantawannakul, P., Chejanovsky, N., Gajda, A., Heerman, M., Panziera, D. *et al.* (2020) Diversity and global distribution of viruses of the western honey bee, *Apis mellifera*. *Insects*, **11**.
2. Liu, Y., Zhang, Y., Wang, M., Cheng, A., Yang, Q., Wu, Y., Jia, R., Liu, M., Zhu, D., Chen, S. *et al.* (2020) Structures and functions of the 3′ untranslated regions of positive-sense single-stranded RNA viruses infecting humans and animals. *Front Cell Infect Microbiol*, **10**, 453.
3. Vidalain, P.O. and Tangy, F. (2010) Virus-host protein interactions in RNA viruses. *Microbes Infect*, **12**, 1134-1143.
4. Ongus, J.R., Roode, E.C., Pleij, C.W.A., Vlak, J.M. and van Oers, M.M. (2006) The 5′ non-translated region of *Varroa destructor* virus 1 (genus *Iflavirus*): structure prediction and IRES activity in *Lymantria dispar* cells. *J Gen Virol*, **87**, 3397-3407.
5. Lu, J., Hu, Y., Hu, L., Zong, S., Cai, D., Wang, J., Yu, H. and Zhang, J. (2007) *Ectropis obliqua* picorna-like virus IRES-driven internal initiation of translation in cell systems derived from different origins. *J Gen Virol*, **88**, 2834-2838.
6. Wu, T.Y., Wu, C.Y., Chen, Y.J., Chen, C.Y. and Wang, C.H. (2007) The 5′ untranslated region of *Perina nuda* virus (PnV) possesses a strong internal translation activity in baculovirus-infected insect cells. *FEBS Lett*, **581**, 3120-3126.
7. Li, M., Man, N., Qiu, H., Cai, S., He, X., He, X. and Lu, X. (2012) Detection of an internal translation activity in the 5′ region of *Bombyx mori* infectious flacherie virus. *Appl Microbiol Biotechnol*, **95**, 697-705.
8. He, Y., Wang, Y., Yin, T., Cuellar, W.J., Liu, S.S. and Wang, X. (2021) Gut-expressed vitellogenin facilitates the movement of a plant virus across the midgut wall in its insect vector. *mSystems*, **6**.
9. Huo, Y., Yu, Y., Liu, Q., Liu, D., Zhang, M., Liang, J., Chen, X., Zhang, L. and Fang, R. (2019) Rice stripe virus hitchhikes the vector insect vitellogenin ligand-receptor pathway for ovary entry. *Philos Trans R Soc Lond B Biol Sci*, **374**, 20180312.
10. Garcia, J., Munro, E.S., Monte, M.M., Fourrier, M.C.S., Whitelaw, J., Smail, D.A. and Ellis, A.E. (2010) Atlantic salmon (*Salmo salar* L.) serum vitellogenin neutralises infectivity of infectious pancreatic necrosis virus (IPNV). *Fish & Shellfish Immunology*, **29**, 293-297.
11. Matozo, T., Kogachi, L. and de Alencar, B.C. (2022) Myosin motors on the pathway of viral infections. *Cytoskeleton (Hoboken)*, **79**, 41-63.
12. Iselin, L., Palmalux, N., Kamel, W., Simmonds, P., Mohammed, S. and Castello, A. (2022) Uncovering viral RNA-host cell interactions on a proteome-wide scale. *Trends Biochem Sci*, **47**, 23-38.
13. Castello, A., Hentze, M.W. and Preiss, T. (2015) Metabolic enzymes enjoying new partnerships as RNA-binding proteins. *Trends Endocrinol Metab*, **26**, 746-757.
14. Balcerak, A., Trebinska-Stryjewska, A., Konopinski, R., Wakula, M. and Grzybowska, E.A. (2019) RNA-protein interactions: disorder, moonlighting and junk contribute to eukaryotic complexity. *Open Biol*, **9**, 190096.
15. DeBlasio, S.L., Wilson, J.R., Tamborindeguy, C., Johnson, R.S., Pinheiro, P.V., MacCoss, M.J., Gray, S.M. and Heck, M. (2021) Affinity purification-mass spectrometry

identifies a novel interaction between a polerovirus and a conserved innate immunity aphid protein that regulates transmission efficiency. *J Proteome Res*, **20**, 3365-3387.
16. Martinez-Salas, E., Francisco-Velilla, R., Fernandez-Chamorro, J. and Embarek, A.M. (2017) Insights into structural and mechanistic features of viral IRES elements. *Front Microbiol*, **8**, 2629.
17. Abdullah, S.W., Wu, J., Wang, X., Guo, H. and Sun, S. (2023) Advances and breakthroughs in IRES-directed translation and replication of picornaviruses. *mBio*, **14**.
18. Guo, Y., Goodman, C.L., Stanley, D.W. and Bonning, B.C. (2020) Cell lines for honey bee virus research. *Viruses*, **12**.
19. Deigan, K.E., Li, T.W., Mathews, D.H. and Weeks, K.M. (2009) Accurate SHAPE-directed RNA structure determination. *PNAS*, **106**, 97-102.
20. Dolgosheina, E.V., Jeng, S.C.Y., Panchapakesan, S.S.S., Cojocaru, R., Chen, P.S.K., Wilson, P.D., Hawkins, N., Wiggins, P.A. and Unrau, P.J. (2014) RNA Mango aptamer-fluorophore: a bright, high-affinity complex for RNA labeling and tracking. *ACS Chemical Biology*, **9**, 2412-2420.
21. Hellman, L.M. and Fried, M.G. (2007) Electrophoretic mobility shift assay (EMSA) for detecting protein-nucleic acid interactions. *Nat Protoc*, **2**, 1849-1861.
22. Moon, M.H., Hilimire, T.A., Sanders, A.M. and Schneekloth, J.S., Jr. (2018) Measuring RNA-ligand interactions with microscale thermophoresis. *Biochemistry*, **57**, 4638-4643.
23. Feig, A.L. (2009) Studying RNA-RNA and RNA-protein interactions by isothermal titration calorimetry. *Methods Enzymol*, **468**, 409-422.
24. Patel, T.R., Chojnowski, G., Astha, Koul, A., McKenna, S.A. and Bujnicki, J.M. (2017) Structural studies of RNA-protein complexes: A hybrid approach involving hydrodynamics, scattering, and computational methods. *Methods*, **118-119**, 146-162.